UNIVERSITY OF CALIFORNIA
RIVERSIDE

Electrospun Polyaniline/Poly (ethylene oxide) Composite Nanofibers Based Gas Sensor

A Thesis submitted in partial satisfaction
of the requirements for the degree of

Master of Science

in

Materials Science and Engineering

by

Changling Li

August 2013

Thesis Committee:
Dr. Nosang Myung, Chairperson
Dr. Jin Nam
Dr. David Kisailus

The Thesis of Changling Li is approved:

Committee Chairperson

University of California, Riverside

ACKNOWLEDGEMENTS

The work presented in this thesis would and could not have been initiated or completed without the generous support of professors, co-workers, friends and family.

I would like to thank my advisor, Prof. Nosang V. Myung for his continuous support and encouragement throughout my Master's Degree. Thank you for believing in me once I started this project. I am so fortunate to have had your mentoring me when I was struggling with my experiment. You gave me many opportunities to be creative, hard-working and responsible. I would like to express my sincere gratitude to you. Thank you.

My heartfelt appreciation goes to lab members, Miluo Zhang, Charles Su, Jiwon Kim, Michael Nlbandian, Lauren Brooks and Tingjun Wu, and especially Nicha Chartuprayoon, for her valuable comments and suggestions on this project. I am also very thankful to Prof. Jin Nam for giving me his guidance and useful suggestions and to Wayne Bosze, for his generous help with me design and review of my work. Thank you.

A special thanks goes to my parents who have always provided the love and support necessary for me to progress to this stage in my life. Thank you for your generosity and help by supporting and encouraging me to work hard and succeed. No words can express how grateful I am for all of your love. Thank you.

ABSTRACT OF THE THESIS

Electrospun Polyaniline/Poly (ethylene oxide) Composite Nanofibers Based Gas Sensor

by

Changling Li

Master of Science, Graduate Program in Materials Science and Engineering
University of California, Riverside, August 2013
Dr. Nosang Myung, Chairperson

Electrospinning as a cost-effective process to synthesize nanofiber with controlled morphology and structure has regained attention in the last decade as result of rapid advancements in nanoscale science and engineering and their applications. Although there are a few works demonstrated the ability to fabricate nano gas sensor using electrospun nanofibers as sensing materials, there are limited works to show the optimization of the sensing performance by understanding the electron transport properties and their sensing mechanism. The overall objective of this work is to electrospun conducting polymer/insulating polymer composite nanofibers (*i.e.,* (+)-camphor-10-sulfonic acid (HCSA) doped polyanline PANI (conductive) blended with PEO (non-conductive)) with different compositions (*i.e.,* 12 to 68 wt.%) and apply them as chemiresistive sensing material to detect ammonia at room temperature. The diameter, defects, and morphology of nanofibers were adjusted by controlling solution composition,

processing parameters and their effect toward the sensing performance were also investigated.

Viscosity of electrospinning solutions was found to have a pronounced impact on fiber diameter and morphology of PANI/PEO nanofibers. Diameters around 350nm of different compositions of PANI/PEO nanofibers were achieved, where decreasing solution viscosity by increasing the PANI content resulted in a morphology changing from individual fibers to junctions. Although all the compositions of PANI/PEO nanofibers show semiconducting behavior and fit a three dimensional variable hopping range model, the activation energy and hopping distance increased as the PANI content decreased.

The PANI/PEO nanofibers exhibited excellent sensitivity towards NH_3 with fast response and recovery times where a low detection limit of 0.5 ppm with the sensitivity of 5.6 %/ppm of NH_3 was achieved from 26 wt.% PANI/PEO nanofibers. Additionally, the PANI/PEO nanofibers response toward water vapor changed from positive to negative indicating the humidity independent ammonia gas sensor can be fabricated by controlling the composition of PANI/PEO nanofibers.

TABLE OF CONTENTS

1 Chapter 1 1

1.1 Introduction 1

1.1.1 Gas sensors 1

1.1.2 Intrinsically Conducting Polymers 3

1.1.3 Polyaniline 4

1.1.4 Electric properties of polyaniline 6

1.1.5 PANI based gas sensors fabricated by various methods 9

1.1.6 Electrospinning 14

1.1.7 Electrospinning polyaniline based gas sensor 17

2 Chapter 2 37

2.1 Abstract 37

2.2 Introduction 38

2.3 Experimental 39

2.3.1 UV-Vis of unfiltered and filtered PANI/PEO solutions 39

2.3.2 Electrospinning PANI/PEO nanofibers 40

2.4 Results and Discussion 41

2.4.1 Characterization of UV-Vis of HCSA doped PANI solutions before and after filtering

2.4.2 Estimation of filtered PANI content 42

2.4.3 Viscosities of different composition of PANI/PEO solutions 43

2.4.4 The effect of colleting distance on the diameter and morphology of PANI/PEO nanofibers 44

2.4.5 Dilution (Viscosity) Effect on diameter and morphology of PANI/PEO nanofibers 45

2.5 Conclusions 46

3 Chapter 3 64

3.1 Abstract 64

3.2 Introduction 66

3.3 Experimental Details 67
3.3.1 Electrospun PANI/PEO nanofibers with different composition 67
3.3.2 Gas sensing measurements 68
3.4 Results and Discussion 68
3.4.1 Material synthesis and characterization 68
3.4.2 Composition effect on electrical characterization 71
3.4.3 Composition effect on sensing performance 72
3.4.4 Temperature dependent of resistance 74
3.4.5 Thickness effect on sensing performance 77
3.5 Conclusions 78
4 Chapter 4(Appendix) 108
4.1 Abstract 108
4.2 Introduction 109
4.3 Experimental Details 110
4.4 Results and Discussion 110
4.4.1 Material characterization 110
4.4.2 NH_3 Sensing 111

LIST OF FIGURES

Figure 1.1 Components of a gas sensor 20

Figure 1.2 Structures of several intrinsically conducting polymers... **Error! Bookmark not defined.**

Figure 1.3 Polyaniline oxidation states (a)leucoemeraldine (b)emeraldine (c)pernigraniline 22

Figure 1.4 Polymerization of polyaniline 24

Figure 1.5 Process of polyaniline is doped with acids 24

Figure 1.6 Conductivity of polyaniline 25

Figure 1.7 Time dependence of R/R_0 of PANI–PSSM thin film (5-layer) on repeated exposure and removal of ammonia; concentration of ammonia in the air–ammonia mixture: (a) 5 ppm and (b) 250 ppm..... 27

Figure 1.8 Dynamic response of the SAW sensor towards different concentrations of (a)H_2 (b)CO, and (c)NO_2 27

Figure 1.9 Electrospinning set-up 28

Figure 1.10 Description of a stable electrospinning jet 28

Figure 2.1 UV-visible spectra of (a)unfiltered HCSA doped PANI with different dilution concentrations (b) PTFE syringe filter filtered HCSA doped PANI solution with same dilution degrees as unfiltered HCSA doped PANI solutions 47

Figure 2.2 Calibration curve comparison of UV-visible absorbance at (a) 365nm and (b)770nm wavelength of HCSA doped PANI before and after filtering..... 48

Figure 2.3 Viscosities of different composition of PANI/PEO solutions 49

Figure 2.4 Fiber diameter distribution (a, b) and SEM images of (c-f) of the electrospun 12 wt.% PANI PANI/PEO nanofibers with varying the distance between collector and spinneret: 15 cm (a-c) and 30 cm (d-f). The applied voltage and flow rate were fixed at 4.5kV and 0.3 ml/hr, respectively. 50

Figure 2.5 Fiber diameter distribution (a, b) and SEM images of (c-f) of the electrospun 26 wt.% PANI PANI/PEO nanofibers with varying the distance between collector and spinneret: 15 cm (a-c) and 30 cm (d-f). The applied voltage and flow rate were fixed at 5 kV and 0.3 ml/hr, respectively. 51

Figure 2.6 Fiber diameter distribution (a, b) and SEM images of (c-f) of the electrospun 45 wt.% PANI PANI/PEO nanofibers with varying the distance between collector and spinneret: 15 cm (a-c) and 30 cm (d-f). The applied voltage and flow rate were fixed at 5 kV and 0.3 ml/hr, respectively. 52

Figure 2.7 Fiber diameter distribution (a, b) and SEM images of (c-f) of the electrospun 52 wt.% PANI PANI/PEO nanofibers with varying the distance between collector and spinneret: 15 cm (a-c) and 30 cm (d-f). The applied voltage and flow rate were fixed at 5 kV and 0.3 ml/hr, respectively. 53

Figure 2.8 Fiber diameter distribution (a, b) and SEM images of (c-f) of the electrospun 68 wt.% PANI PANI/PEO nanofibers with varying the distance between collector and

spinneret: 15 cm (a-c) and 30 cm (d-f). The applied voltage and flow rate were fixed at 5.5 kV and 0.3 ml/hr, respectively. 54

Figure 2.9 The effect of applied voltage on the diameters of different compositions of PANI/PEO nanofibers 55

Figure 2.10 The effect of composition and distance between collector and needle on the diameter of electrospun nanofibers..... 55

Figure 2.11 Fiber diameter distributions and SEM images of 12 wt% PANI/PEO nanofiber at 4.5 kV as function of different dilution degrees: (a, e) no dilution, (b, f) 10 v%, (c, g) 30 v%, (d, h) 50 v%..... 56

Figure 2.12 Fiber diameter distributions and SEM images of 26 wt% PANI/PEO nanofiber at 5 kV as function of different dilution degrees: (a, e) no dilution, (b, f) 10 v%, (c, g) 30 v%, (d, h) 50 v%. 57

Figure 2.13 Fiber diameter distributions and SEM images of 45 wt% PANI/PEO nanofiber at 5 kV as function of different dilution degrees: (a, e) no dilution, (b, f) 10 v%, (c, g) 20 v%, (d, h) 30 v%. 58

Figure 2.14 Fiber diameter distributions and SEM images of 68 wt% PANI/PEO nanofiber at 5.5 kV as function of different dilution degrees: (a, c) no dilution, (b, d) 10 v%. 59

Figure 2.15 Relationship between solution viscosities and dilution degrees of different composition of PANI/PEO solutions 60

Figure 2.16 The effect of applied voltage on the diameters of electrospun nanofibers 60

Figure 2.17 Average electrospun nanofibers diameter as function of solution viscosity 61

Figure 3.1 Diameter distributions of different composition of PANI/PEO nanofibers with PANI content (wt.%) (a)12 (b)26 (c)45 (d)52 80

Figure 3.2 Scanning electron microscopy images of the electrospun PANI/PEO nanofibers with PANI content(wt.%): (a)(b)12, (c)(d)26, (e)(f)45, (g)(h)52. 80

Figure 3.3 FT-IR of different compositions of PANI/PEO nanofibers (a)(e)12wt.% PANI (b)(f)26wt.% PANI (c)(g)45wt.% (d)(h)52wt.% with various wave number (cm^{-1}) range . 81

Figure 3.4 Direct energy band gap of PANI/PEO fiber mats 82

Figure 3.5 Band gap for HCSA doped PANI 82

Figure 3.6 Dectak images of electrospun 12wt.% PANI/PEO nanofibers with different electrospining time: (a)2.5min (b)5min (c)7.5min (d)10min 83

Figure 3.7 Dectak images of electrospun 26wt.% PANI/PEO nanofibers with different electrospining time: (a)10min (b)15min (c)20min (d)25min (e)30min 83

Figure 3.8 Dectak images of electrospun 45wt.% PANI/PEO nanofibers with different electrospining time: (a)15min (b)20min (c)25min (d)30min 84

Figure 3.9 Dectak images of electrospun 52wt.% PANI/PEO nanofibers with different electrospining time: (a)15min (b)20min (c)25min (d)30min 84

Figure 3.10 Electrospinning time effect on the thickness of different composition of PANI/PEO fiber mats. PANI content (wt.%): (a)12 (b)26 (c)45 (d)52 85

Figure 3.11 Linear rate of different composition of PANI/PEO fiber mats 85

Figure 3.12 Fabrication of PANI/PEO fiber mats contact 86

Figure 3.13 I-V curves of PANI/PEO fiber mats with 800nm thickness. PANI content (wt.%): (a)12 (b)26 (c)45 (d)52 87

Figure 3.14 Electrical conductivity of the HCSA doped PANI and PEO blend electrospun nanofibers 87

Figure 3.15 Real-time response of different composition of PANI/PEO nanofibers to different concentrations of NH_3. PANI content (wt.%): (a)12 (b)26 (c)45 (d)52 89

Figure 3.16 Real-time response of different composition of PANI/PEO nanofibers to different concentrations of NH_3 90

Figure 3.17 Sensing Mechanism of HCSA doped Polyaniline to NH_3..... 90

Figure 3.18 Calibration Curve of sensitivity of different composition of PANI/PEO nanofibers exposed to NH_3 91

Figure 3.19 PANI Content effect on NH3 sensing sensitivity..... 91

Figure 3.20 Calibration curve of response time to different concentrations of NH_3 92

Figure 3.21 Calibration curve of recovery time to different concentrations of NH_3..... 92

Figure 3.22 Real-time response of different composition of PANI/PEO nanofibers to different concentrations of NH_3. PANI content (wt.%): (a)12 (b)26 (c)45 (d)52 94

Figure 3.23 Real-time response of different composition of PANI/PEO nanofibers to different concentrations of NH_3 95

Figure 3.24 Sensing mechanism of HCSA doped polyaniline to water..... 95

Figure 3.25 Calibration Curve of sensitivity of different humidity degree..... 96

Figure 3.26 I-V characteristics of PANI/PEO nanofiber with various temperatures. PANI content (wt.%): (a)12 (b)26 (c)45 (d)52 97

Figure 3.27 Resistivity at various temperature 98

Figure 3.28 Temperature coefficient of resistance for different compositions of PANI/PEO nanofibers 98

Figure 3.29 Arrhenius plot for different compositions of PANI/PEO nanofibers 99

Figure 3.30 Activation energy for different compositions of PANI/PEO nanofibers..... 99

Figure 3.31 Reduced activation energy for different compositions of PANI/PEO nanofibers 100

Figure 3.32 Plot of ln(ρ) as function of $T^{1/2}$, $T^{1/3}$, $T^{1/4}$ 100

Figure 3.33 Average hopping distance for different compositions of PANI/PEO nanofibers 101

Figure 3.34 Average hopping energy for different compositions of PANI/PEO nanofibers 101

Figure 3.35 Dectak images of 52wt.% PANI/PEO nanofibers with different thickness (a)0.82µm (b)1.15µm (c)3.57µm (d)5.24µm 102

Figure 3.36 I-V curve of 52wt.% PANI/PEO nanofibers with different thickness(a)0.82µm (b)1.15µm (c)3.57µm (d)5.24µm 102

Figure 3.37 Resistance of 52wt.% PANI/PEO fiber mats with different thickness 103

Figure 3.38 Electric conductivity of 52wt.% PANI/PEO fiber mats with different thickness 103

Figure 3.39 Real-time response of different thickness of 52wt.% PANI/PEO nanofibers to different concentrations of NH_3 104

Figure 3.40 Calibration curve of different NH_3 concentrations of 52wt.% PANI/PEO nanofibers with different thickness 104

Figure 3.41 Calibration curve of response time of different composition of PANI/PEO nanofibers exposed to NH_3 105

Figure 3.42 Calibration curve of recovery time of different composition of PANI/PEO nanofibers exposed to NH_3 105

Figure 4.1 Distribution areas of inkjet printing different drops of 1.3wt.% and 0.13wt.% PEDOT-PSS 113

Figure 4.2 Optical images of Ink-jet printing different drops of 1.3wt.% PEODT-PSS (a)20 drops (b)10 drops (c)5 drops (d)1 drop 114

Figure 4.3 Optical images of Ink-jet printing different drops of 1.3wt.% PEODT-PSS (a)20 drops (b)10 drops (c)5 drops (d)1 drop 114

Figure 4.4 Dectak images of ink-jet printing different drops of 1.3wt.% PEDOT-PSS (a)20 drops (b)10 drops (c)5 drops (d)1 drop 115

Figure 4.5 Dectak images of ink-jet printing different drops of 0.13wt.% PEDOT-PSS (a)20 drops (b)10 drops (c)5 drops (d)1 drop 115

Figure 4.6 Films thickness of ink-jet printing different drops of 1.3wt.% and 0.13wt.% PEDOT-PSS 116

Figure 4.7 Resistivity of ink-jet printing different drops of 1.3wt.% and 0.13wt.% PEDOT-PSS 116

Figure 4.8 Real-time response of ink-jet printing different drops of 1.3wt.% PEDOT-PSS exposed to NH_3 (a)20 drops (b)10 drops (c)5 drops (d)1 drop 118

Figure 4.9 Real-time response of ink-jet printing different drops of 0.13wt.% PEDOT-PSS exposed to NH_3 (a)20 drops (b)10 drops (c)5 drops (d)1 drop 120

Figure 4.10 Calibration curves of ink-jet printing different drops of (a) 1.3wt.% and (b) 0.13wt.% PEODT-PSS exposed to NH_3 sensing 121

Figure 4.11 Calibration curve of different thickness of PEODT-PSS to NH_3 sensing 122

LIST OF TABLES

Table 1.1 Sensor types 21

Table 1.2 Solubility and conductivity of emeraldine salt with(SO_3^-) counter ion, R contains functional group 23

Table 1.3 Summary of selected sensing performance of PANI based gas sensors 26

Table 1.4 Gas sensors based on electrospun polyaniline nanofibers 29

Table 2.1 Calculation of filtered PANI content in PANI/PEO blends 49

Table 2.2 Shear rates of different composition of PANI/PEO solutions in the needle.... 49

Chapter 1
INTRODUCTION

1.1 Introduction

1.1.1 Gas sensors

Gaseous analytes such as NH_3, NO_2, CO, SO_2 and CO_2 are harmful to human health and to the environment. Automotive emissions contribute 50-70% of gaseous analytes that are harmful to human health. Other harmful sources include the burning of fuels by industry, medical manufacturing, metals processing, mining, agriculture and residential pollution. Increasing levels of these analytes can have far reaching impacts on our environment ranging from altering the earth's protective ozone layer to global warming. Over exposure to such harmful gases can weaken human health progressing from benign eye, skin, nose irritations, to impairing the respiratory system, to attacking our central nervous system - or even death[2, 3]. For example, the detection and measurement of ammonia has gained attention in industrial and medical fields due to its high toxicity and explosive nature. Exposures to ammonia at 25 ppm over 8 hours or 35 ppm over 15 minutes are harmful to human health[4-6]. In order to detect all the above species, federal and state agencies (including the Environmental Protection Agency, Department of Energy, and their sponsors) have been working toward improving access to accurate information sufficient to effectively protect human health and the environment. Thus, the

development of cost effective, rapid and highly sensitive, selective, and reliable gas sensors will play a key role in educating the public to increase environmental awareness, and implementing and enforcing local, state, and federal environmental laws.

Gas sensors are devices that can detect the presence of different gases in an area where the gas alters one or more of its element's properties in a direct or indirect way [10]. As shown in figure 1.1, a typical sensor consists of two important parts: the sensing material (element) and a transducer. As the sensing material interacts with targeted gases its property change (*e.g.,* resistance, mass, color or capacitance) while the transducer, an integral part of the sensing system, transfers the response to a readable signal. Characteristically, the performance of a chemical gas sensor performance is able to have high sensitivity, high selectivity, low detection limit, fast response and recovery times, and a wide dynamic range meaning that it can detect the analyte in a large concentration with high sensitivity[4, 13, 14]. Manufactures of commercial sensor systems have become plentiful in recent times and produce a wide range of products utilizing different sensor types depending mainly on the specific applications. Many of these systems are reviewed in table 1.1.

Various materials including polymers[16], semiconductors[17, 18], carbon[19, 20], and organic/inorganic composites[22] have been synthesized as the sensing materials to detect different analytes. The sensitivity of a gas sensor strongly depends on the specific surface area to volume ratio. Conducting polymers, such as polypyrrole (PPy), polyaniline

(PANI), polythiophene (PTh) and their derivatives have been developed as gas sensors. Compared to metal oxide commercial sensors which require to operate at high temperature, conducting polymer based sensors are easy to fabricate and exhibit high sensitivity and fast response time at room temperature. Thus, researchers have given more attention in developing conducting polymer based gas sensors[24, 25].

1.1.2 **Intrinsically Conducting Polymers**

A large number of organic compounds, which effectively induce electron movement, are basically classified with charge complex/ion radical salts, organometallic species and conjugated organic polymers. A new class of polymer known as intrinsically conducting polymers (ICPs) were discovered in 1960[28]. Their interesting physical, chemical and biological properties and numerous potential applications had attracted the beginning of research investigations. In recent years, ICPs have been investigated for their possible applications such as electronics, electrochemical, electromagnetic, thermoelectric, electro-rheological, chemical, membrane and sensors [31-33].

ICPs are intrinsically conducting in nature due to the presence of a conjugated π electron system in their structure. ICPs posse electronic properties, low ionization potentials, low energy optical transitions and a high electro affinity. This extended π-conjugated system of conducting polymer is linked with single and double bonds The conductivity level can be tuned near to that of a metal depending on the oxidation states

and doping level with a suitable dopant[37, 38]. Shirakawa Louis et al. first polymerized polyacetylene, and he found that it could be transformed from insulator to metal behavior by chemical doping where the conductivity increased by several orders of magnitude. Other polymers such as polypyrrole(PPy), polythiophene(PTh), poly(p-phenylenevinylene) and poly(p-phenylene), as well as their derivatives, have been synthesized as ICPs[41]. The structures of some ICPs are shown in figure 1.2.

1.1.3 **Polyaniline**

Polyaniline(PANI) is recognized as one of the most useful ICPs due to its ease of synthesis, good stability at room temperature, attractive properties and low-cost materials in its fabrication process[42-46]. However, the main obstacles need to overcome ICPs including polyaniline is insulating compared to metal, and they have very low solubility in most organic solvents. However, the conductivity and solubility of polyaniline can be enhanced by doping or modifying the starting monomer[44, 49, 50]. Polyaniline has also been successfully utilized as a blend member with other commercially available polymers which possess good mechanical and processing abilities. Although the preparation of polyaniline blended with insulating polymers can be problematic, a vulcanized and stable PANI matrix can be achieved through a judicious mixture of ingredients including curatives, colorants and anti-degradants. Thermoplastic elastomers (TPE) have also been successfully used as a carrier host when acids are required which

protonate PANI reducing the vulcanization effect. Thus, with its improved electrically conductivity, mechanical and processing properties, ICP's of blended polyaniline composites show great potential to open wider application areas [51-53].

Polyaniline is superior to other ICPs. Its processability and conductivity of PANI are good, and its stability is better than most conductive polymers. Moreover, it is expected to have advantages in its manufacturing because the monomer is inexpensive relative to other ICP monomers, its synthesis is simple, and its properties are easily tuned[55-57].

Polyaniline exists in three oxidation states when it's polymerized from an aniline monomer. They can be classified as leucoemeraldine, emeraldine and pernigraniline based on the ratio of amine to imine as shown in figure 1.3. Leucoemeraldine is the fully reduced state, where the polyaniline chain is linked with imine. Pernigraniline is the fully oxidized state which is composed of amine. The emeraldine polyaniline is neutral and regarded as the most useful form of polyaniline because of its high stability at room temperature, and the resulting emeraldine salt doped with the imine nitrogen protonated by an acid is electrically conductive. Leucoemeraldine and pernigraniline are poor conductors, even when doped with acids. These three oxidation states could be transformed by oxidation and reduction. Many suitable dopants can improve the conductivity of polyaniline[60, 61]. In contrast, the treatment of neutral of alkaline media is able to decreased the conductivity of conducting emeraldine salt by ten orders of magnitude[33]. The oxidation states of polyaniline correspond to different colors; this

property can be utilized to fabricate sensors and electronic devices. However, the excellent and tunable conductivity of polyaniline which relies on the doping levels and oxidation states is more attractive for sensor applications.

Various methods have been successfully used to synthesize polyaniline which can be classified as chemical, electrochemical, enzymatic, template, photo, plasma, etc. Chemical synthesis is subsequently divided into seeding, solution, interfacial, heterophase, self-assembling and sonochemical polymerizations[41, 50]. In general, polyaniline is polymerized by dissolving aniline and ammonium persulfate in hydrochloric acid, where the precipitates are collected and used as emeraldine base polyaniline. The reaction is shown in figure 1.4[64].

1.1.4 **Electric properties of polyaniline**

Polyaniline with various dopants were polymerized and their conductivity and solubility were compared as shown in table 1.1, where R represents the functional group with sulfonic acid. It shows that the conductivity of polyaniline was further enhanced when polyaniline was doped with camphor sulfonic acid (HCSA), and its solubility in several solvents was also improved. The acid's doping process is shown in figure 1.5. The counter- ions group protonates imine nitrogen on the polymer chain, which induces the charge carrier. The doped polyaniline exists in two forms as shown in figures 1.5(b) and

(c): the bipolaron structure and stable polaron structure, they are interchangeable[32, 60, 66].

Polyaniline is a p-type semiconductor and charge carriers acting as holes are the lead to the movement of electrons[69]. The polaron structure is responsible for electric conduction by a hopping mechanism on the polymer chain[71]. After protonating the imine nitrogen, valence holes are created and act as charge carriers. The electron from the adjacent nitrogen on the amine group jumps to that hole and that hole becomes neutral and the second hole on the imine group is created. Thus, the hole starts to move. The conductivity can be tuned by more than 14 orders of magnitude from an insulating region to a metallic doped PANI region as shown in figure 1.6. The resulting conductivity is influenced by four factors; namely molecular weight, percentage of crystallinity, oxidation degree and doping level[72, 73].

Electric conductivity is related to the density of charge carriers, charge of each carrier and the mobility of each carrier, which can be described by the following equation:

$$\sigma = en\mu$$

where σ is the conductivity (S/m), n is the charge carrier density (m^{-3}), μ is the mobility of each carrier (m^2/Vs) and e is the single electronic charge ($1.6 \times 10^{-19}C$). The π electron system exists in polyaniline and the difference between the π orbitals and π* orbitals is the band gap of the valance band and conduction band. Lower band gap makes electron

hopping easier, leading to a high conductivity[76]. The electrical conduction mechanism in PANI has been investigated by researchers.

Variable range hopping (VRH) models of PANI electrical conduction mechanism have been studied by temperature dependent of resistance. Lee et al. studied the charge transport of the fully sulfonated polyaniline. The temperature dependent dc conductivity fit the quasi-1D variable range hopping model: $\sigma_{dc}(T)=\sigma_o \exp[-(T_o/T)^{\gamma}]$ because γ equaled 0.5[79]. Quasi-1D VRH reveals that the conductivity is highly anisotropic along the polymer chains. The resistivity was sensitive at higher temperature and insensitive at lower temperature. With increasing of resistivity, its temperature dependence tends toward a saturation effect at higher temperature and is fit by a T^2 Power law at lower temperature[80]. Mott's law can be used for charactering the hopping mechanism of a disordered semiconductor with localized states, the variable-range hopping is expressed in terms of conductivity as

$$\sigma(T) = \sigma_o \exp\left[-\left(\frac{T_o}{T}\right)^{\gamma}\right] \qquad \text{Eq. (1.1)}$$

$$\sigma_o = e^2 \nu R^2 N(E) \qquad \text{Eq. (1.2)}$$

$$T_o = \frac{\lambda \alpha^3}{kN(E)} \qquad \text{Eq. (1.3)}$$

where e is the electronic charge, ν is a hopping frequency, λ ≈ 18.1 is a dimensionless constant, α is the inverse rate of fall of wave function, k is Boltzmann's constant, N(E) is

the density of states at the Fermi level. For a 3D hopping model, the hopping distance R equals:

$$R=[9/8\pi\alpha kTN(E)]^{1/4} \qquad \text{Eq. (1.4)}$$

where the exponent can take on the values γ = 1/2, 1/3, 1/4 are representing the 1D, 2D, 3D electron hopping conduction models. The average hopping energy W can be calculated by the hopping distance R and the Fermi level N(E) by the following equation:

$$W = 3/4\ \pi R^3 N(E) \qquad \text{Eq. (1.5)}$$

By plotting $\ln(\sigma T1/2)$ as a function of $T^{-1/4}$, the linear rate and intercept of fitting straight line can be used to calculate the values of T_o and σ_o[81].

1.1.5 **PANI based gas sensors fabricated by various methods**

The performance of PANI based gas sensors to environmental pollutants, including NH_3, NO_2, CO and other gaseous analytes, is not only dependent on the electrical nature of polyaniline, but it is also strongly dependent on the processing methods employed. Researchers have used various nano-manufacturing methods to physically and chemically adjust the molecular structure of PANI and evaluated these various PANI structures as a gas sensor element including sensitivity, selectivity, electrical conductivity stability and durability. Several polyaniline-based environmental gas sensors are listed in table 1.2[82].

In 2004, G.K. Prasad and co-workers synthesized PANI using the salt of 1: poly (4-styrenesulfonate-co-maleic acid as the protonation reagent and ammonium peroxodisulfate $(NH_4)2S_2O_8$ as the oxidation agent. The water soluble, polyeletrolyte (PSSM) template PANI mixed with polyvinyl alcohol (PVA) solution was spin cast on a glass substrate and the electric contact for thin film and sensing air-circulating fan were connected through a stopper and passage to make the sensor model. The ammonia sensing response of the thin films was investigated. The 5-layered film was the optimal sensing system. It was found that the resistance was reversible and reproducible at NH_3 concentrations ranging from 5-250 ppm and the response and recovery time were within 50-1000 s as shown in figure 1.7 [1].

Similarly, Dan Xie et al. fabricated the pure polyaniline film, polyaniline and acetic acid(AA) mixed film, and polyaniline doped with polystyrenesulfonic acid(PSSA) composite film with various layers through Langmuir-Blodgett(LB) and self-assembly(SA) methods[8]. Quartz and silicon were used as the substrates and the inter-digitated electrode gold pattern were coating on the silicon to connect with thin films. The sensors were tested to NO_2 ranged from 1 to 200 ppm. The thinner the films, the higher the sensitivity achieved and the faster response time performed.

Do et al. fabricated the amperometric NO_2 gas sensor using the PANI/Au/Nafion as the working electrode prepared by the methods of cyclic voltammetry (CV), constant current (CC) and constant potential (CP) methods, respectively[12]. When the current

density used to prepare PANI/Au/Nafion increased from 1 to 10mAcm^{-2} (CC method) and worked as the sensing electrode, the sensitivity of the gas sensor to NO_2 decreased from 2.35 to 1.41μA ppm^{-1} at 300 ml min^{-1}. The optimal sensitivity was found to be 3.04 μA ppm^{-1} when PANI/Au/Nafion electrode was fabricated by CV method in 1.0M $HClO_4$. Moreover, the maximum sensitivity of PANI/Au/Nafion based gas sensor prepared with the constant potential (CP) method was 2.54 μA ppm^{-1} when exposed to NO_2. The NO_2 concentration was ranged from 0 to 100 ppm, the response time of the gas sensors were 14 minutes at a constant potential, 18 minutes (CV method) and 19 minutes (CC method).

Yan et al. demonstrate detection of NO_2 with a polyaniline nanofibers networks synthesized by an interfacial polymerization method[26]. The uniform and diluted dispersion of PANI nanofibers in water were drop-cast onto the patterned gold electrodes by a microliter pipette and dried in vacuum at room temperature. Upon exposure to NO_2 gas with different concentrations ranging from 10 to 200 ppm, the resistance of polyaniline emeraldine salt increased dramatically, even three orders of magnitude in 100 ppm. The sensor had a rapid response time for NO_2 gas at room temperature.

Wanna et al. studied the effect of a carbon nanotube dispersion effect on CO gas sensing performance versus a conventional polyaniline gas sensor by the means of solution casting[29]. The carbon nanotubes were synthesized with acetylene and argon gases at 600 ^{O}C by chemical vapor deposition (CVD). The polyaniline was polymerized using maleic acid as the dopant. The dispersed CNTs were then mixed with polyaniline

solution with ultrasonication and deposited on an interdigitated Al electrode by solvent casting. The gas sensor was tested with CO concentrations ranging from 100-1000 ppm at room temperature. The sensitivity was improved with the existence of CNTs to CO gas and the response and recovery time was reduced by more than 2 orders of magnitude compared to polyaniline without CNT- based gas sensor. Shiigi et al. also fabricated a polyaniline/poly(vinylalcohol) (PVA) based gas sensor detecting the presence of CO_2 at room temperature by solution casting[30].

Manoj et al. fabricated an ultrathin conducting polymer/metal oxide (SnO_2 and/or TiO_2) films based gas sensor for CO detection via in situ layer-by-layer (LBL) self-assembly method[34]. The indium-tin oxide (ITO) coated glass and interdigitated electrodes were washed with methanol/chloroform and treated with aqueous ammonia to make the surface hydrophilic. Such substrates were used for the deposition of in situ self-assembled LBL films. The sensor can detect CO at a concentration as low as 1 ppm at room temperature.

Sutar et al. also developed a polyaniline film based chemiresistor. The fibrous polyaniline films with a highly crystalline structure was polymerized on an amino SAM-modified silicon substrate[35]. The chemiresistor sensors were exposed to different concentrations of NH_3 and the lower detection limit was 0.5 ppm. The sensor detected with fast response time and recovery time were both around 15 minutes.

Sadek et al. demonstrated the polyaniline/In_2O_3 nanofiber composite based layered surface acoustic wave (SAW) sensor by drop casting a nanocomposite onto a layered ZnO/64^o YX $LiNbO_3$ SAW transducer[39]. The composite was synthesized by chemical oxidation polymerization by adding finely In_2O_3 to aniline solution. The detection limit of the sensor for H_2, CO and NO_2 were 0.06%, 60 ppm and 510 ppb, respectively. The response times were 30, 24 and 30 s for H_2, CO and NO_2. The recovery times were 40, 36 and 65 s. The real-time response the composite to different gases are shown in figure 1.8.

Dixit et al. reported the fabrication of polyanline semiconducting thin films based gas sensor for the detection of CO prepared by vacuum deposition[47]. Polyaniline was synthesized through copolymerization of aniline and formaldehyde, and metal halides were used as the dopants because of being sensitive to CO gas. The polymeric thin films were prepared on glass substrate by vacuum deposition and ITO coated glass plates under a vacuum of 10^{-6} mmHg. The gas sensor could detect a CO concentration as low as 10 ppm with very short response time (5 s).

Bishop et al. developed a cost-effective electrospinning technique for generating conductive polymer PANI blended with carrier hosting polyvinyl pyrrolidone (PVP) hybrid structures for NO_2 detection at room temperature[15]. The nanofiber composite was collected on an alumina substrate with gold interdigitated contacts using a DC voltage power supply. The sensor was tested at room temperature and 40% RH. The lowest detection limit of the sensor is 1 ppm.

Conducting polymers (CPs) are novel intrinsically conducting organic materials which require lower power and are stable when operated at room temperature. Conducting polymers are cost-effective materials for fabricating and manufacturing gas sensors. Many researchers have demonstrated that the polyaniline based gas sensor developed by adjusting the structures of PANI with various processing methods show excellent sensing performance to specific analytes. Thus, the current research focuses on the improvement of the quality of gas sensors made by polyaniline as the platform.

1.1.6 **Electrospinning**

Electrospinning technology has regained more interests in the last 10 years probably due in large part to an increased subject in nanoscale properties and technology. The electrospinning process is able to produce ultrafine fibers or fibrous structures of various polymers with diameters ranging from several nanometers to microns[83]. When the diameters of polymer fibers decrease down to sub-micron or nanometer, several interesting properties appear including the very large surface area to volume ratio, which could be 10^3 times more than that of a microfiber, controlled surface flexibility, superior mechanical properties (e.g. surface tension, and stiffness) compared to materials synthesized by other methods. These attractive performance make the electrospun polymer nanofibers to the outstanding candidates for many important applications [84-86]. Many techniques have been developed to produce polymer nanofibers including

template synthesis[87], drawing[88], self-assembly[89], and electrospinning[90]. In terms of the flexibility of the process, electrospinning is able to fabricate ultralong and continuous nanofibers from a number of materials. Typically, nanofibers of polymer, composites, semiconductor and ceramics are electospinnable[91].

Promising features of electrospinning are its simple and low cost setup and processing. The typical electrospinning setup consists of a syringe pump, a high voltage source and a collector as shown in figure 1.9. During the electrospinning process, a polymer precursor is fed through a syringe and held with a needle tip by surface tension. An electric field using the high-voltage source is applied to cause charges within the precursor. This electrostatic repulsive force counters the surface tension force. When the charge repulsion reaches a critical value, it overcomes the surface tension and a jet erupts from the tip of the needle and is drawn to a collector of opposite potential. During the jet transient, the solvent evaporates and polymer fibers deposit on the collector. This method has been used successfully to electrospun numerous polymer solutions into ultralong fibers[91-93]s.

Reneker and Chun reported the prototypical path of an electrospinning jet in detail as shown in figure 1.10[94]. When the electrostatic force is larger than the surface tension at the tip of the needle, a jet emerges to from a cone, known as the Tylor cone. The straight jet is transformed into a three-dimensional coil gradually changing to a smaller coil. With the further stretching and accelerating of the polymer jet, the jet

diameter decreases as the length becomes longer. More than one jet can form from a Taylor cone. Also branched fibers can be made by ejecting smaller jets from the surface of the primary jet(s). Continuous, while the solvents evaporate the charge repulsive force can split the fiber jet(s) into many smaller fibers. This multi-jet, stretching and splitting process determines the fiber diameter(s) collected on the substrates.

The electrospinning process is impacted by various parameters. Reneker and Doshi reported that the factors that control the electrospinning process can be classified with solution properties, spinning variables, and ambient factors [95]. Solution properties are related to viscosity, surface tension, conductivity, polymer molecular weight, dipole moment and dielectric constant. These effects are influenced by each other if one factor varies. The working spinning variables have applied voltage, flow rate, collecting distance, needle diameter, and collector design. Ambient factors include temperature, humidity, and velocity. The above parameters determine the fiber diameter and morphology of electrospun fibers [84].

Viscosity is recognized as the most important effect on fiber diameter and morphology during the electrospinning process. At low polymer concentrations, the beads and droplets exist on the fiber, or the junctions and bundles have been observed because of incomplete solvent evaporation. To get uniform fibers, increasing the concentrations of a polymer precursor makes the droplet dry out quickly at the tip before the jet emerges [95-97]. Surface tension has relationship with the existence of beads[98].

With lower viscosity, the solvent molecules tend to come together under the action of surface tension resulting in bead formations. Solutions with high conductivity leads to fibers with fewer beads because high charge density makes fibers stretch further[99]. It has been found that the number of beads and droplets decreased when the molecular weight increased[100]. The dipole moment and dielectric constant of the polymer solution have not been investigated widely so far. For the electrospinning parameters, in general, fiber diameter is reduced if the feed rate decreases or the applied voltage increases. Researchers found that a minimum distance is necessary to allow solvent evaporation and fiber jet stretches, or beads or drops would appear. The needle size has an effect on shear rate, which influences the fiber diameter. Regarding ambient factors, high temperature resulted in smaller fibers and increasing of humidity lead to the pores coalescing[96, 101].

1.1.7 **Electrospinning polyaniline based gas sensor**

Polyaniline (PANI) is an intrinsically conducting polymer that have been used to fabricate gas sensors as the sensing materials. Polyaniline is easy to synthesize and the polymerized existing states (pernigraniline, emeraldine and leucoemeraldine) can be transformed with redox. It is stable to environmental changes. For example, emeraldine base polyaniline can stand high temperature up to 300^{o}C related to the dopants. Moreover, the resulting polyaniline salts are soluble in various organic solvent such as

chloroform, dimethylsulfoxide, dimethylformamide, tetrahydrofuran, 1-methyl 2-pyrrolidinone. Furthermore, dopants protonating iminic nitrogen on polyaniline chain changes the conductivity from undoped insulating base form (σ≤10-10 S/cm) to completely doped salt from (σ≥1 S/cm)[67]. Nanofibers synthesized from electrospinning technique leads to a large surface which is one to two orders of magnitude larger than flat films fabricated by other methods. The large surface to volume ratio makes nanofibers excellent candidates for the potential application in sensors[4].

Chen et al. fabricated single polyaniline nanofiber field effect transistor (FET) gas sensor by electropinning polyaniline blended with polyethylene oxide (PEO) as the carrier hosting[9]. The contact between the polymer and gold electrodes was ohmic, in contrast, a Schottky barrier forms at the polymer and n-type silicon contact interface. A higher gate voltage enhanced the sensitivity to NH_3, and the nanofiber transistor showed a 7% reversible resistance change to 1 ppm NH_3 when the gate voltage was at 10 V.

Macagnano et al. electrospun polyaniline blended with various insulating host polymers non-woven framework and enable gas sensors based on these hybrid structures to function over a wide dynamic range of gas or vapour concentrations[21]. The transducer that used to transform the chemical change of interactions between nanofibers and analytes was manufactured by a standard photolithographic process: a chromium-gold layer was evaporated onto a silicon waver to generate the electrodes after lift-off procedure. The PANI/PS, PANI/PEO and PANI/PVP matrix based gas sensor

response to different concentrations of NH_3, NO_2 and NO showed an increase in current. The detection limits were 175 ppb, 1 ppm and 1 ppm for detecting NH_3, NO_2 and NO gases, respectively.

Pinto et al. fabricated isolated camphor sulfonic acid doped polyaniline blended with poly(ethylene oxide) (PEO) nanofibers based gas sensors and they were tested exposed to various aliphatic alcohol vapors[24]. The response of the electrospun nanofibers to small alcohol molecules is opposite to that tested base on cast nanofiber mats. The sensor exhibited good sensing performance for different alcohol vapors. The response times were 32, 20, 110 s for methanol, ethanol and 2-propanol vapors, respectively. And the recovery time were 20, 20, 50 s.

Other researchers also have fabricated polyaniline composites based gas sensors by electrospinning technique shown in table 1.3. Sensors based on the use of π-conjugated conducting polymers have been developed as the next cost-effective and disposable generation of electronic devices[36]. However, the lifetimes of sensors based on organic materials are generally only several months, which inhibit the development of its potential application-especially since the sensors are easily poisoned by high concentrations of the targeted analytes. Furthermore, poor selectivity for specific analytes also limit future developments in organic material based gas sensors.

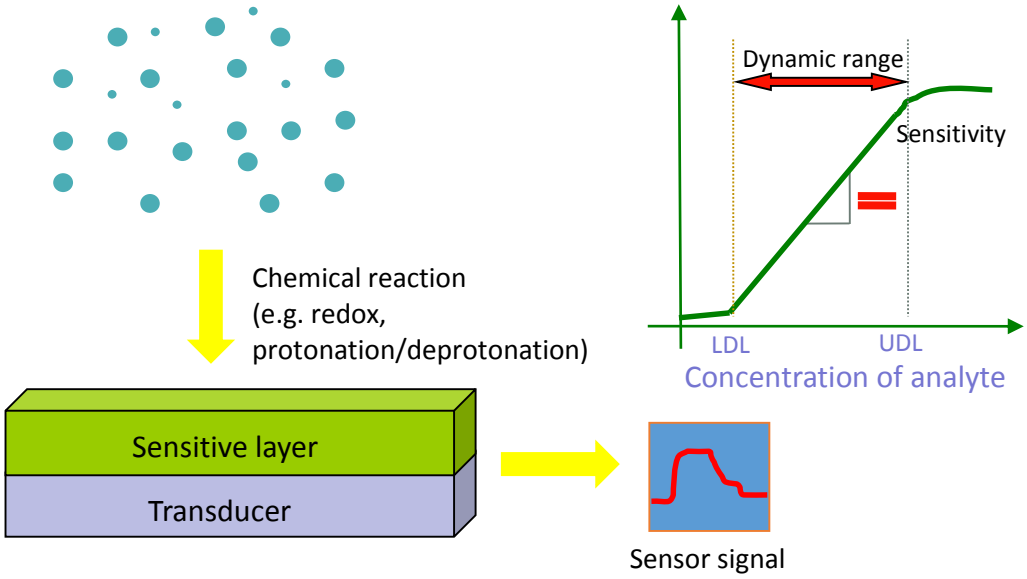

Figure 1.1 Components of a gas sensor

Table 1.1 Sensor types

Sensor type	Signal	Fabrication	Advantages	Disadvantages
Chemiresistor	Conductivity	Screenprinting, spincoating, dipcoating, spray coating, microfabrication, electrochemical; chemical polymerization, electrospinning, etc	Operate at diverse environment, cheap, fast response and recovery time, IC integratable	Sensitive to temperature and humidity, suffer from baseline drift, poisoning, limited rang of coatings
ChemFET	Threshold/ voltage change	Chemical, electrochemical, FR sputtering, thermal evaporating, electrospinning, microfabration, inkjetprinting, microfabrication, etc	Small, good stability, low cost sensors, CMOS integratible and reproducible	Base line drift, need controlled environment
SAW	Piezoelectricity	Photolithography, airbrushing, screenprinting, dipcoating, spincoating,etc	Diverse range of coatings, high sensitivity, good response times, IC integratable	Complex interface circuitry, difficult to reproduce
QCM	Piezoelectricity	Micromachining, spincoating, airbrushing, inkjetprinting, dipcoating, etc.	Diverse range of coatings, good batch to batch reproducibility	Poor signal-to-noise ratio, complex circuitry
Optodes/ Photoelectric	Intensity/ Spectrum	Photolithography, airbrushing, screenprinting, spincoating, electrochemical,etc	Immune to electromagnetic interference, fast response time, cheap, light weight	Suffer from photobleaching, complex interface circuitry, restricted light sources
Amperometric	Thermal conductivity	Electrochemical, chemical, etc.	High signal-noise ratio, good stability, high sensitivity	Slow response, sensitivity to temperature and PH, signal drift
Thermistor	Thermal conductivity	Electrochemical, chemical, etc.	High sensitivity, accuracy and low cost	Aging, interchangeability, unreliability
Pellistor	Thermal conductivity	Microfabrication, electrochemical, chemical, etc.	Fast response, cost-effective, reproducibility	Unstable intensity detection, non-linear response

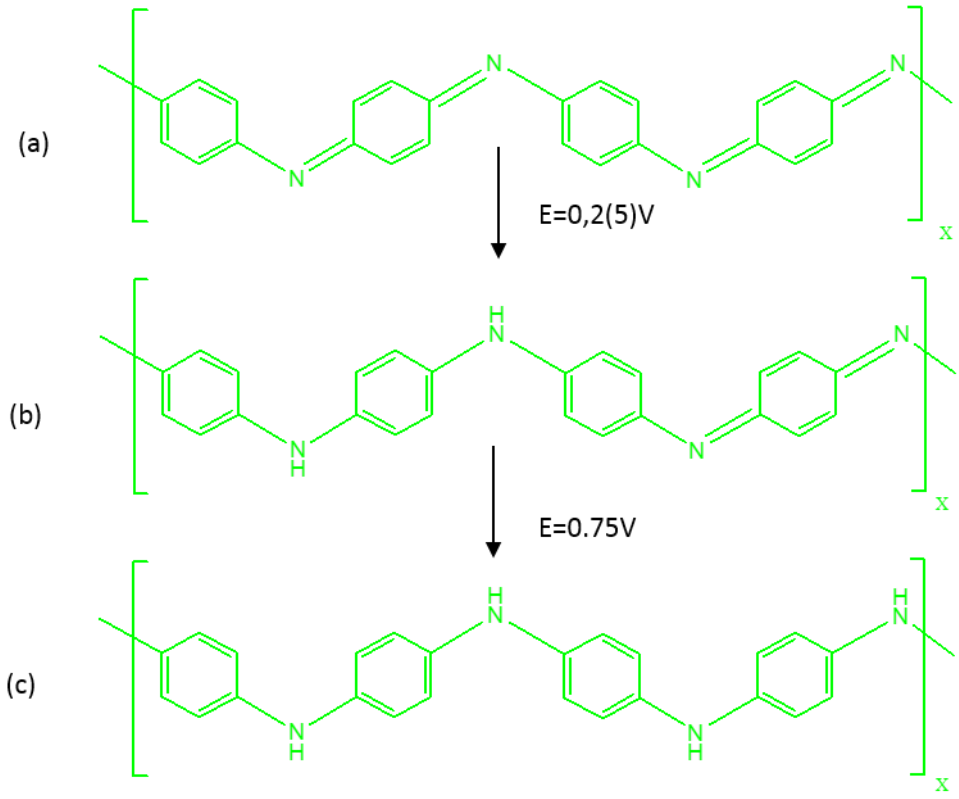

Figure 1.2 Polyaniline oxidation states (a)leucoemeraldine (b)emeraldine (c)pernigraniline

Table 1.2 Solubility and conductivity of emeraldine salt with (SO_3^-) counter ion, R contains functional group

(SO_3)-R	**σ(S/cm)**		**Solubility[b]**				
	Pellet	Film	Xylene	$CHCl_3$	m-Cresol	Formic acid	DMSO
C_6H_{13}	10		O				
C_8H_{17}	19		O				
$C_8F_{17}COOH$	2.7		__[e]				
C_8F_{17}	3.7		__[e]				
(1,D)-Camphor	1.8	100-400		⊙	⊙	⊙	O
4-Dodecylbenzene	26.4	100-250	⊙	⊙	⊙	O	
O-Anisidine-5-	$7.7x10^{-3}$					O	O
O-Anisidine-5-	7.3					O	O
4-Nitrotoluene-2-	$5.7x10^{-2}$					O	O
Dinonylnaphthalene	$1.8x10^{-5}$		O	⊙			
Cresol red	$2.2x10^{-4}$ [d]						
Pyrrogallol red	$1.2x10^{-1}$ [d]						
Pyrrocatechol violet	$1.9x10^{-1}$ [d]						

[a]Films were cast from concentrated solution; O=soluble at room temperature; Δ=low conductivity⊙=very soluble at room temperature; [b]Soluble in perfluoralkanes, e.g..nPerfluorodecaline. [d]Pressed at 165°C.Source: Ref. 36.

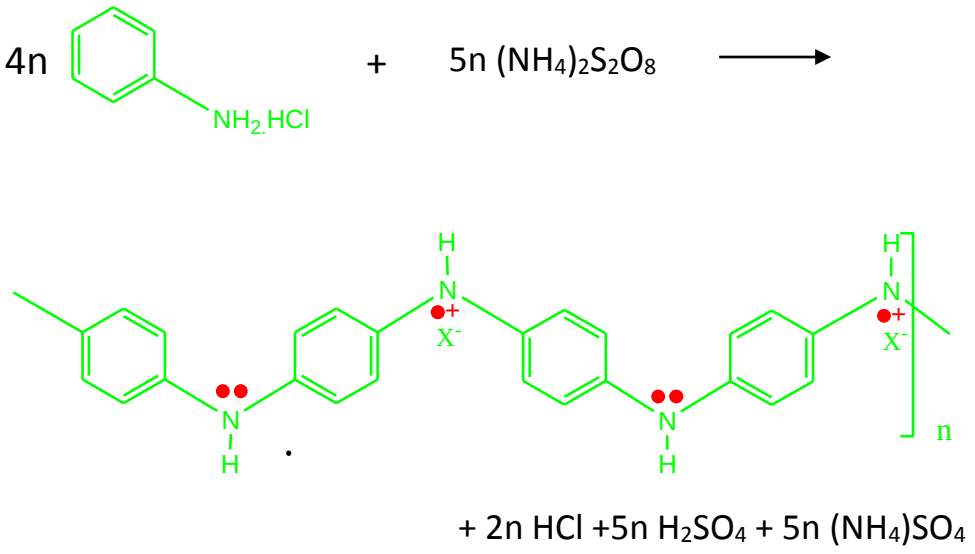

Figure 1.3 Polymerization of polyaniline

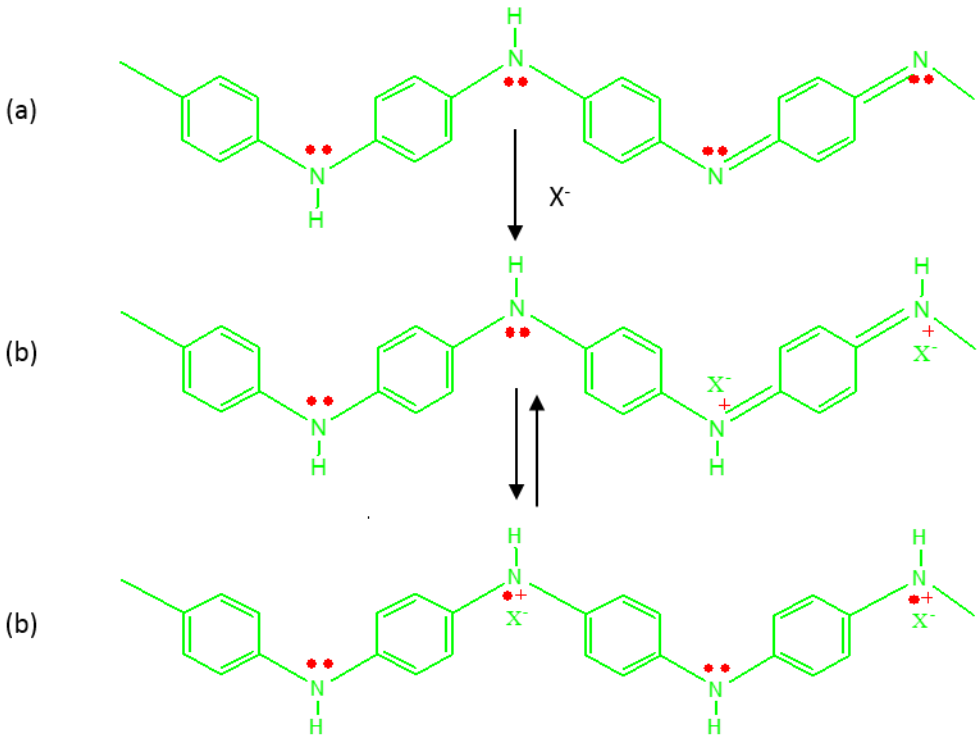

Figure 1.4 Process of polyaniline is doped with acids (X^- represents counter-ion group)

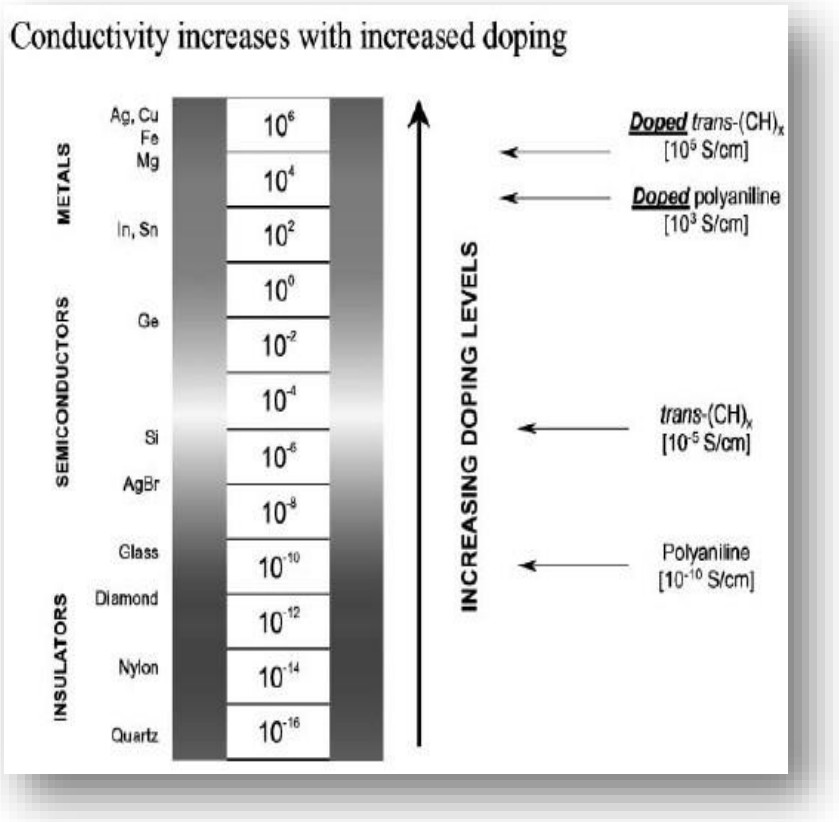

Figure 1.5 Conductivity of polyaniline

Table 1.3 Summary of selected sensing performance of PANI based gas sensors

Processing methods	Sensor configuration	Dopant/ composite	Targeted analytes	Detection limit	Response time	Reversibility	REF
Spin Coating	Chemiresistor	Poly(4-styrenesulfonate-co-maleic acid)	NH_3	5 ppm	60 s	Reversible (50-1000s)	[1]
Langmuir Blodgett	Chemiresistor	EB/Acetic Acid	NO_2	20 ppm	10 s	2-4min	[8]
Cyclic Voltammetry	Chemiresistor	$HClO_4$, H_2SO_4, HCl/PANI/Au/Nafion	NO_2	20 ppm	18 min	Reversible	[12]
Constant Current	Chemiresistor	$HClO_4$, H_2SO_4, HCl/PANI/Au/Nafion	NO_2	20 ppm	19 min	Reversible	[12]
Constant Potential	Chemiresistor	$HClO_4$, H_2SO_4, HCl/PANI/Au/Nafion	NO_2	20 ppm	14 min	Reversible	[12]
Interfacial Polymerization	Chemiresistor	HCl	NO_2	10 ppm	104 s	Reversible	[26]
Solution Casting	Chemiresistor	EB/Poly vinyl alcohol composite: Maleic Acid/Cacon Nanotubes	CO_2/CO	100 ppm/167 ppm	5 min/0.6 min	Reversible	[29, 30]
Self Assembly	Chemiresistor	HCl/SnO2, TiO2; aminosilane for templating	CO/NH_3	1 ppm/0.5 ppm	80 s/60 s	15min	[34, 35]
Drop Casting	Chemiresistor	Camphorsulfonic acid(CSA)/In2O3	CO,NO_2	60ppm/0.51ppm	24 s/ 30 s	Reversible	[39]
Vacuum Deposition	SAW	Fe-Al	CO	10 ppm	5 s	100 s	[47]
Electrospinning	Chemiresistor	H_2O	NO_2	1 ppm	4 min	Irreversible	[15]
Pressed Pellets	Chemiresistor	Maleic Acid/Zeolite	CO	7.8 ppm	169 min	N/S	[58]

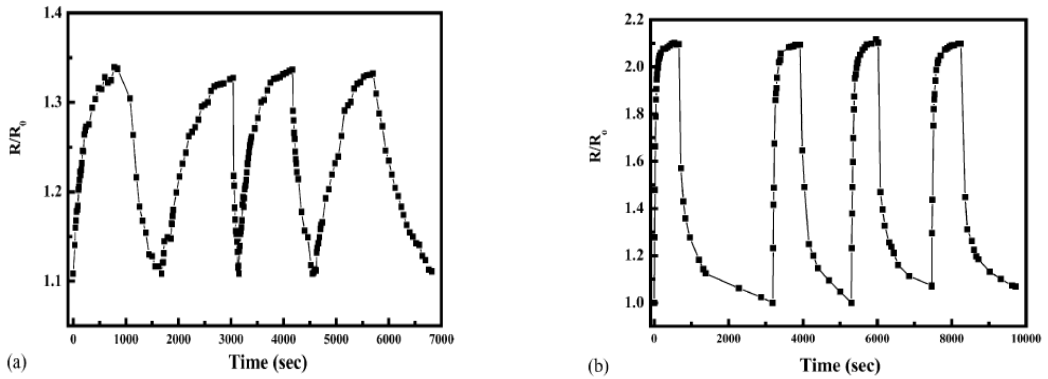

Figure 1.6 Time dependence of R/R_0 of PANI–PSSM thin film (5-layer) on repeated exposure and removal of ammonia; concentration of ammonia in the air–ammonia mixture: (a) 5 ppm and (b) 250 ppm.

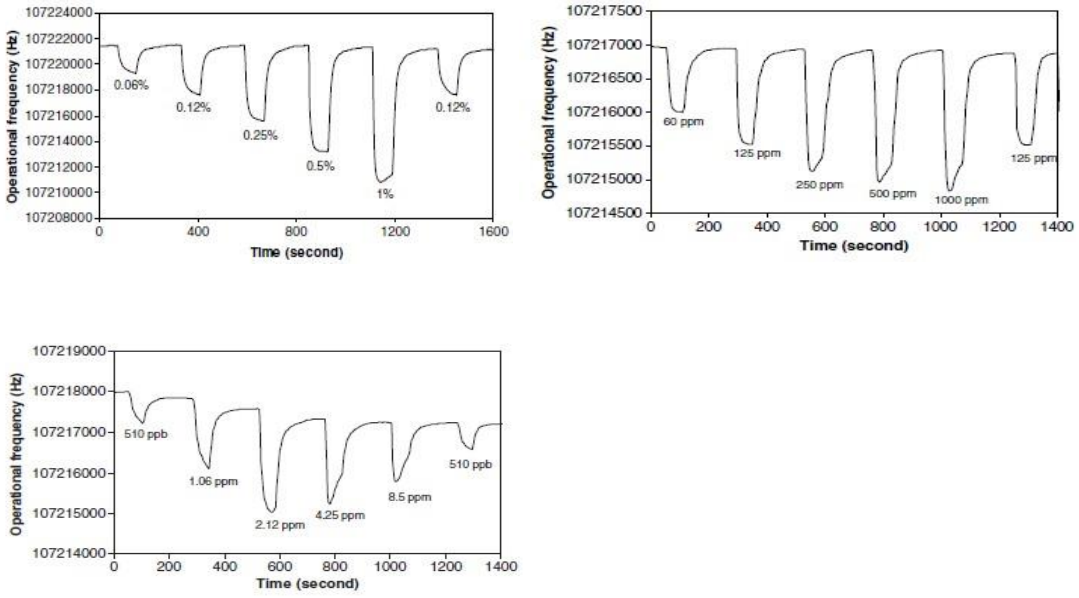

Figure 1.7 Dynamic response of the SAW sensor towards different concentrations of (a)H_2 (b)CO, and (c)NO_2

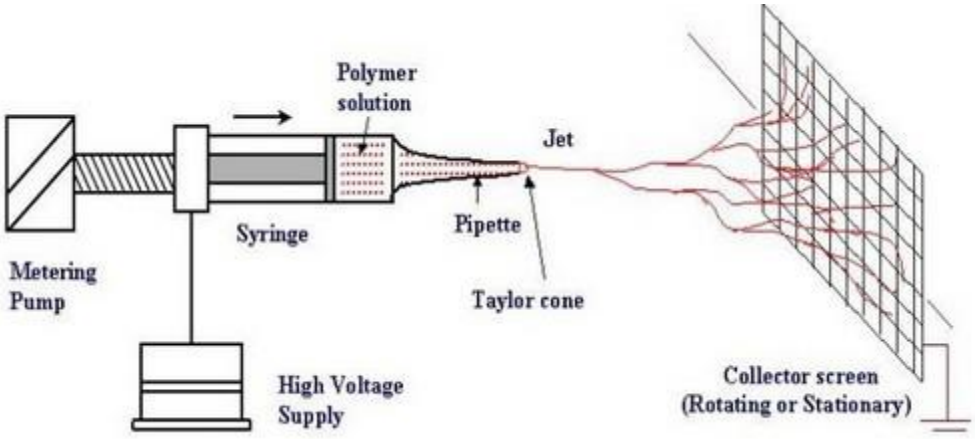

Figure 1.8 Electrospinning set-up

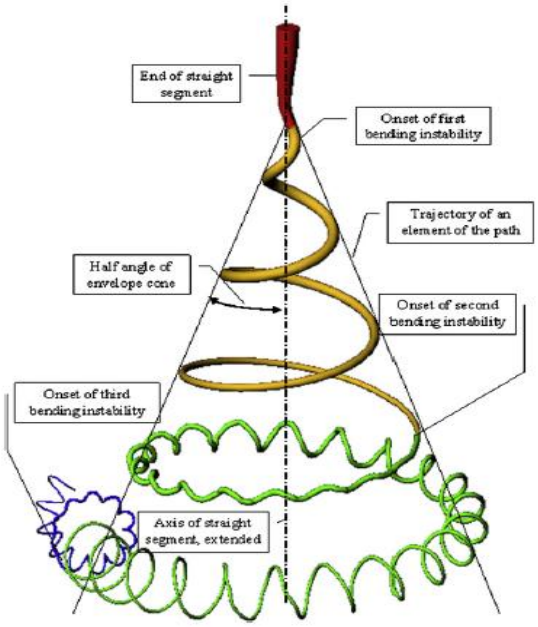

Figure 1.9 Description of a stable electrospinning jet

Table 1.4 Gas sensors based on electrospun polyaniline nanofibers

CPs	Mw	Doping	Nanofiber Carrier	Solvent Composite	Voltage (kV)	Dis. (cm)	Fiber Diameter (nm)	Electrode	Collecting distance (μm)	Carrier Gas	Relative Humidity	Analyte	Detection Limit (ppm)	Ref.
PANI		$HCSA/PdCl_2$	PEO	$CHCl_3$	1.3	0.2	550	Au	10	Air	Dry	H_2	$3x10^3$	[7]
		HCSA	PEO	$CHCl_3$	0.8	0.2	400	Au	10	N_2	Dry	NH_3	1	[9]
		HCSA	PVP	Ethanol	15	5.5	$1x10^3$-$1x10^4$	Au		air	40%	NO_2	1-7	[11]
		HCSA	PEO	$CHCl_3$			20-150	Au		N_2	Dry	Water/Methanol/ $CHCl_3$		[15]
	10k	HCSA	PS	$CHCl_3$/THF	10	5	300	Au	20	N_2	Dry	NH_3	0.175	[21]
	10k		PEO	$CHCl_3$/EtOH	10	5	50-600	Au	20	N_2	Dry	NO_2	0.25-1.5	
	10k		PVP	$CHCl_3$/EtOH	10	5	50-600	Au	20	N_2	Dry	NO_2,NH_3		
			PVP	EtOH	15	5-6		Al		Air	20%	NO_2	1-7	[23]
			PVP/urease	EtOH	20	5-6		Al		Air	40%	NO_2	1-7	
		HCSA	PEO	$CHCl_3$	8	20	120-300	Au						[27]
		HCSA	PEO	$CHCl_3$				Au						[36]
	65k	HCSA	PEO	$CHCl_3$	25-40	30								[40]
			PMMA	CHCl/DMF	34	30								
		HCSA	PEO	$CHCl_3$			30							[48]
		HCSA	PEO/MSWNT	$CHCl_3$	10	13		Au						[54]
	20k	HCSA	PEO	$CHCl_3$										[59]
	10k	HCSA	PVP	$CHCl_3$										[62]
		HCSA	PEO	$CHCl_3$	8	20								[27]
		HCSA	PMMA	$CHCl_3$	15-25									[63]
	50k	DBSA	PHB	$CHCl_3$		10	15							[65]
	65k	HCSA	PMMA	$CHCl_3$										[67]
	65k	HCSA	PMMA	$CHCl_3$	15-25									[68]
	10k	HCSA	PS	$CHCl_3$/THF	10	5				N_2	10%-30%	NO_2	1	[70]
			PVP	$CHCl_3$/EtOH	10	5				N_2	10%-30%	NH_3	0.5	
			PEO	$CHCl_3$/EtOH	10	5				N_2	10%-30%	NO_2	0.25	
		HCSA	PEO	$CHCl_3$			100	Au		N_2	Dry	NH_3		[74]
		HCSA	PEO	$CHCl_3$			100	Au		N_2	Dry			[75]
	65k	HCSA	PEO/SWNT	$CHCl_3$			100	Au		N_2	Dry			[77]
			CA	Acetone	8	0.5		Al		air	20%	NO_2	1	[78]
	10k	HCSA	PS	$CHCl_3$/THF	10	5		Au						[25]
	10k		PEO	$CHCl_3$/EtOH	10	5		Au						
	10k		PVP	$CHCl_3$/EtOH	10	5		Au						
		HCSA	PEO	$CHCl_3$			20-150	Au		N_2	Dry	Ethanol, Methanol, 2-propanol		[25]

References:

1. Prasad, G.K., et al., Ammonia sensing characteristics of thin film based on polyelectrolyte templated polyaniline. Sensors and Actuators B: Chemical, 2005. **106**(2): p. 626-631.
2. U.S. Environmental Protection Agency, National Ambient Air Quality Standards. 1990.
3. U.S. Environmental Protection Agency, Six Common Pollutants. 1990.
4. Ding, B., et al., Gas Sensors Based on Electrospun Nanofibers. Sensors, 2009. **9**(3): p. 1609-1624.
5. Kong, J., et al., Nanotube Molecular Wires as Chemical Sensors. Science, 2000. **287**(5453): p. 622-625.
6. Göpel, W. and K.D. Schierbaum, SnO2 sensors: current status and future prospects. Sensors and Actuators B: Chemical, 1995. **26**(1–3): p. 1-12.
7. Dajing, C., et al. Polyaniline nanofiber gas sensors by direct-write electrospinning. in Micro Electro Mechanical Systems (MEMS), 2011 IEEE 24th International Conference on. 2011.
8. Xie, D., et al., Fabrication and characterization of polyaniline-based gas sensor by ultra-thin film technology. Sensors and Actuators B: Chemical, 2002. **81**(2–3): p. 158-164.
9. Chen, D., S. Lei, and Y. Chen, A Single Polyaniline Nanofiber Field Effect Transistor and Its Gas Sensing Mechanisms. Sensors, 2011. **11**(7): p. 6509-6516.
10. Jin, Z., et al., Application of nano-crystalline porous tin oxide thin film for CO sensing. Sensors and Actuators B: Chemical, 1998. **52**(1–2): p. 188-194.
11. a, A.B.-H.a.b.P.G., Electrospun Polyaniline Composites for NO2 Detection. Materials and Manufacturing Processes, 2007. **22**(6).
12. Do, J.-S. and W.-B. Chang, Amperometric nitrogen dioxide gas sensor based on PAn/Au/Nafion® prepared by constant current and cyclic voltammetry methods. Sensors and Actuators B: Chemical, 2004. **101**(1–2): p. 97-106.
13. Lee, D.-S., et al., Nitrogen oxides-sensing characteristics of WO3-based nanocrystalline thick film gas sensor. Sensors and Actuators B: Chemical, 1999. **60**(1): p. 57-63.
14. Göpel, W., Supramolecular and polymeric structures for gas sensors. Sensors and Actuators B: Chemical, 1995. **24**(1–3): p. 17-32.
15. Bishop-Haynes, A. and P. Gouma, Electrospun Polyaniline Composites for NO2 Detection. Materials and Manufacturing Processes, 2007. **22**(6): p. 764-767.
16. Slater, J.M., et al., Gas and vapour detection with poly(pyrrole) gas sensors. Analyst, 1992. **117**(8): p. 1265-1270.
17. Schierbaum, K.D., U. Weimar, and W. Göpel, Comparison of ceramic, thick-film and thin-film chemical sensors based upon SnO2. Sensors and Actuators B: Chemical, 1992. **7**(1–3): p. 709-716.

18. Savage, N., et al., Composite n–p semiconducting titanium oxides as gas sensors. Sensors and Actuators B: Chemical, 2001. **79**(1): p. 17-27.
19. Varghese, O.K., et al., Gas sensing characteristics of multi-wall carbon nanotubes. Sensors and Actuators B: Chemical, 2001. **81**(1): p. 32-41.
20. ukaszewicz, J.P., Carbon Materials for Chemical Sensors: A Review. Sensor Letters, 2006. **4**(2): p. 53-98.
21. Macagnano, A., et al., Nanofibrous PANI-based conductive polymers for trace gas analysis. Thin Solid Films, 2011. **520**(3): p. 978-985.
22. Unde, S., J. Ganu, and S. Radhakrishnan, Conducting polymer-based chemical sensor: Characteristics and evaluation of polyaniline composite films. Advanced Materials for Optics and Electronics, 1996. **6**(3): p. 151-157.
23. Gouma, A.B.a.P., Leuco-emeraldine based polyaniline-polyvinylpyrrolidone electrospun composites and biocomposites: A preliminary study of sensing behavior. Rev.Adv.Mater.Sci., 2005. **10**: p. 209-214.
24. Pinto, N.J., et al., Electric response of isolated electrospun polyaniline nanofibers to vapors of aliphatic alcohols. Sensors and Actuators B: Chemical, 2008. **129**(2): p. 621-627.
25. Zampetti, E., et al., Effects of temperature and humidity on electrospun conductive nanofibers based on polyaniline blends. Journal of Nanoparticle Research, 2011. **13**(11): p. 6193-6200.
26. Yan, X.B., et al., NO2 gas sensing with polyaniline nanofibers synthesized by a facile aqueous/organic interfacial polymerization. Sensors and Actuators B: Chemical, 2007. **123**(1): p. 107-113.
27. Pinto, N.J., et al., Electrospun polyaniline/polyethylene oxide nanofiber field-effect transistor. Applied Physics Letters, 2003. **83**(20): p. 4244-4246.
28. Gerard, M., A. Chaubey, and B.D. Malhotra, Application of conducting polymers to biosensors. Biosensors and Bioelectronics, 2002. **17**(5): p. 345-359.
29. Y. Wanna, N.S., A. Tuantranont, A. Wisitsoraat, N. Thavarungkul, and a.P. Singjai, The effect of carbon nanotube dispersion on CO gas sensing characteristics of polyaniline gas sensor. Journal of Nanoscience and Nanotechnology, 2006. **6**: p. 3893–3896.
30. H. Shiigi, T.O., T. Tonosaki, and K. Ogura, CO2-sensitive Characteristics of Base-type Polyaniline/Poly(vinyl alcohol) Composites at Room Temperature and Effects of Coexisting Gases. Electrochemistry, 2001. **69**(12): p. 997-1001.
31. Schoch, K.F., Update on electrically conductive polymers and their applications. Electrical Insulation Magazine, IEEE, 1994. **10**(3): p. 29-32.
32. Angelopoulos, M., Conducting polymers in microelectronics. IBM Journal of Research and Development, 2001. **45**(1): p. 57-75.
33. Gospodinova, N. and L. Terlemezyan, Conducting polymers prepared by oxidative polymerization: polyaniline. Progress in Polymer Science, 1998. **23**(8): p. 1443-1484.

34. Ram, M.K., et al., CO gas sensing from ultrathin nano-composite conducting polymer film. Sensors and Actuators B: Chemical, 2005. **106**(2): p. 750-757.
35. Sutar, D.S., et al., Preparation of nanofibrous polyaniline films and their application as ammonia gas sensor. Sensors and Actuators B: Chemical, 2007. **128**(1): p. 286-292.
36. Pinto, N.J., et al., Electrospun hybrid organic/inorganic semiconductor Schottky nanodiode. Applied Physics Letters, 2006. **89**(3): p. 033505-033505-3.
37. Bhadra, S., et al., Improvement of conductivity of electrochemically synthesized polyaniline. Journal of Applied Polymer Science, 2008. **108**(1): p. 57-64.
38. Bhadra, S., N.K. Singha, and D. Khastgir, Polyaniline by new miniemulsion polymerization and the effect of reducing agent on conductivity. Synthetic Metals, 2006. **156**(16–17): p. 1148-1154.
39. Sadek, A.Z., et al., A layered surface acoustic wave gas sensor based on a polyaniline/In 2 O 3 nanofibre composite. Nanotechnology, 2006. **17**(17): p. 4488.
40. Rutledge, Y.Z.a.G.C., Electrical Conductivity of Electrospun Polyaniline and Polyaniline-Blend Fibers and Mats. Macromolecules, 2012. **45**(10): p. 4238-4246.
41. Shirakawa, H., et al., Synthesis of electrically conducting organic polymers: halogen derivatives of polyacetylene, (CH). Journal of the Chemical Society, Chemical Communications, 1977. **0**(16): p. 578-580.
42. Bhadra, S., N.K. Singha, and D. Khastgir, Electrochemical synthesis of polyaniline and its comparison with chemically synthesized polyaniline. Journal of Applied Polymer Science, 2007. **104**(3): p. 1900-1904.
43. Bhadra, S. and D. Khastgir, Degradation and stability of polyaniline on exposure to electron beam irradiation (structure–property relationship). Polymer Degradation and Stability, 2007. **92**(10): p. 1824-1832.
44. Bhadra, S., N.K. Singha, and D. Khastgir, Effect of aromatic substitution in aniline on the properties of polyaniline. European Polymer Journal, 2008. **44**(6): p. 1763-1770.
45. Bhadra, S. and D. Khastgir, Extrinsic and intrinsic structural change during heat treatment of polyaniline. Polymer Degradation and Stability, 2008. **93**(6): p. 1094-1099.
46. Bhadra, S. and D. Khastgir, Glass–rubber transition temperature of polyaniline: Experimental and molecular dynamic simulation. Synthetic Metals, 2009. **159**(12): p. 1141-1146.
47. Dixit, V., S.C.K. Misra, and B.S. Sharma, Carbon monoxide sensitivity of vacuum deposited polyaniline semiconducting thin films. Sensors and Actuators B: Chemical, 2005. **104**(1): p. 90-93.
48. Zhou, Y., et al., Fabrication and electrical characterization of polyaniline-based nanofibers with diameter below 30 nm. Applied Physics Letters, 2003. **83**(18): p. 3800-3802.

49. Bhadra, S. and D. Khastgir, Rheological properties, shear-dependent electrical resistance, and settling phenomena of polyaniline in ECO solution. Journal of Applied Polymer Science, 2009. **114**(1): p. 238-245.
50. Cho, M.S., et al., Synthesis and electrical properties of polymer composites with polyaniline nanoparticles. Materials Science and Engineering: C, 2004. **24**(1–2): p. 15-18.
51. Bhadra, S. and D. Khastgir, In situ preparation of polyaniline coated fumed and precipitated silica fillers and their composites with nitrile rubber (Investigation on structure-property relationship). European Polymer Journal, 2007. **43**(10): p. 4332-4343.
52. Bhadra, S., N.K. Singha, and D. Khastgir, Mechanical, dynamic mechanical, morphological, thermal behavior and processability of polyaniline and ethylene 1-octene based semi-conducting composites. Journal of Applied Polymer Science, 2008. **107**(4): p. 2486-2493.
53. Bhadra, S., N.K. Singha, and D. Khastgir, Dielectric properties and EMI shielding efficiency of polyaniline and ethylene 1-octene based semi-conducting composites. Current Applied Physics, 2009. **9**(2): p. 396-403.
54. Shin, M.K., et al., Enhanced conductivity of aligned PANi/PEO/MWNT nanofibers by electrospinning. Sensors and Actuators B: Chemical, 2008. **134**(1): p. 122-126.
55. Bhadra, S., N.K. Singha, and D. Khastgir, Semiconductive composites from ethylene 1-octene copolymer and polyaniline coated nylon 6: Studies on mechanical, thermal, processability, electrical, and EMI shielding properties. Polymer Engineering & Science, 2008. **48**(5): p. 995-1006.
56. Sinha, S., S. Bhadra, and D. Khastgir, Effect of dopant type on the properties of polyaniline. Journal of Applied Polymer Science, 2009. **112**(5): p. 3135-3140.
57. Rao, P.S., S. Subrahmanya, and D.N. Sathyanarayana, Synthesis by inverse emulsion pathway and characterization of conductive polyaniline–poly(ethylene-co-vinyl acetate) blends. Synthetic Metals, 2003. **139**(2): p. 397-404.
58. N. Densakulprasert, L.W., D. Chotpattananont, P. Hiamtup, A. Sirivat, and J. Schwank, Electrical conductivity of polyaniline/zeolite composites and synergetic interaction with CO. Materials Science and Engineering B, 2005. **117**: p. 276-282.
59. Jun Kameoka1, R.O., Yanou Yang1, David Czaplewski1, Robert Mathers2, Geoffrey W Coates2 and H G Craighead1, A scanning tip electrospinning source for deposition of oriented nanofibres This. nanotechnology, 2003. **14**(10): p. 1124.
60. Fukushima, M., et al., Effects of dopants and polymer structures on electrical conductivity of organosilicon polymers. Synthetic Metals, 1998. **94**(3): p. 299-306.
61. Fukushima, M., et al., Electrical conductivity of organosilicon polymers II: Synthesis and electrical conductivities of iodine-doped polysilanes containing amino groups. Synthetic Metals, 1998. **96**(3): p. 239-244.

62. Pecora, A., et al. Chemoresistive nanofibrous sensor array and read-out electronics on flexible substrate. in Solid-State Sensors, Actuators and Microsystems Conference, 2009. TRANSDUCERS 2009. International. 2009.
63. K. Desai, C.S., DOE Optimization and Phase Morphology of Electrospun Nanofibers of PANI/PMMA Blends. Nanotechnology, 2004. **3**: p. 429-432.
64. Gilbert2, J.S.a.R.G., Polyaniline. Preparation of a conducting polymer(IUPAC Technical Report)Pure and Applied Chemistry, 2002. **74**(5): p. 857-867.
65. Fryczkowski, R. and T. Kowalczyk, Nanofibres from polyaniline/polyhydroxybutyrate blends. Synthetic Metals, 2009. **159**(21–22): p. 2266-2268.
66. Ramadin, Y., et al., Determination of the type of charge carriers in carbon fiber/polymer composite. Polymer Testing, 1998. **17**(1): p. 35-42.
67. K.Desai*, C.S., PHASE CHARACTERIZATION AND MORPHOLOGY CONTROL OF ELECTROSPUN NANOFIBERS OF PANI/PMMA BLENDS. Mat.Res.Soc.Symp.Proc., 2004. **788**.
68. Sung, K.D.a.C., Electrospinning Nanofibers of PANI/PMMA Blends. Materials Research Society, 2003. **736**.
69. Fukushima, M., et al., Electrical conductivity of organosilicon polymers III: Carrier mobility analysis of iodine-doped polysilane by hall effect measurement. Synthetic Metals, 1998. **96**(3): p. 245-248.
70. Zampetti, E., et al., Biomimetic sensing layer based on electrospun conductive polymer webs. Biosensors and Bioelectronics, 2011. **26**(5): p. 2460-2465.
71. Monkman, A.P., et al., Electronic structure and charge transport mechanisms in polyaniline. Synthetic Metals, 1989. **29**(1): p. 277-284.
72. Luthra, V., et al., Mechanism of dc conduction in polyaniline doped with sulfuric acid. Current Applied Physics, 2003. **3**(2–3): p. 219-222.
73. W. Focke, W. and G. E. Wnek, Conduction mechanisms in polyaniline (emeraldine salt). Journal of Electroanalytical Chemistry and Interfacial Electrochemistry, 1988. **256**(2): p. 343-352.
74. Rivera, R. and N.J. Pinto, Schottky diodes based on electrospun polyaniline nanofibers: Effects of varying fiber diameter and doping level on device performance. Physica E: Low-dimensional Systems and Nanostructures, 2009. **41**(3): p. 423-426.
75. Ian D. Norris a, M.M.S.b., Frank K. Ko b, Alan G. MacDiarmid a, Electrostatic fabrication of ultrafine conducting fibers:polyanilinerpolyethylene oxide blends. Synthetic Metals, 2000. **114**: p. 109-114.
76. Bhadra, S., N.K. Singha, and D. Khastgir, Dual functionality of PTSA as electrolyte and dopant in the electrochemical synthesis of polyaniline, and its effect on electrical properties. Polymer International, 2007. **56**(7): p. 919-927.

77. Sundaray, B., A. Choi, and Y.W. Park, Highly conducting electrospun polyaniline-polyethylene oxide nanofibrous membranes filled with single-walled carbon nanotubes. Synthetic Metals, 2010. **160**(9–10): p. 984-988.
78. Haynes, A.S. and P.I. Gouma, Electrospun Conducting Polymer-Based Sensors for Advanced Pathogen Detection. Sensors Journal, IEEE, 2008. **8**(6): p. 701-705.
79. Lee, W., et al., Charge transport properties of fully-sulfonated polyaniline. Synthetic Metals, 1997. **84**(1–3): p. 807-808.
80. Bhadra, S., et al., Progress in preparation, processing and applications of polyaniline. Progress in Polymer Science, 2009. **34**(8): p. 783-810.
81. Campos, M. and B. Braz, Jr., Mechanism of conduction in doped polyaniline. Journal of Physics D: Applied Physics, 1997. **30**(10): p. 1531.
82. Haynes, A. and P.-I. Gouma, Polyaniline-Based Environmental Gas Sensors, in Sensors for Environment, Health and Security, M.-I. Baraton, Editor 2009, Springer Netherlands. p. 451-459.
83. Morozov, V., T. Morozova, and N. Kallenbach, Atomic force microscopy of structures produced by electrospraying polymer solutions. International Journal of Mass Spectrometry, 1998. **178**(3): p. 143-159.
84. Subbiah, T., et al., Electrospinning of nanofibers. Journal of Applied Polymer Science, 2005. **96**(2): p. 557-569.
85. Huang, Z.-M., et al., A review on polymer nanofibers by electrospinning and their applications in nanocomposites. Composites Science and Technology, 2003. **63**(15): p. 2223-2253.
86. Frenot, A. and I.S. Chronakis, Polymer nanofibers assembled by electrospinning. Current Opinion in Colloid & Interface Science, 2003. **8**(1): p. 64-75.
87. Feng, L., et al., Super-Hydrophobic Surface of Aligned Polyacrylonitrile Nanofibers. Angewandte Chemie, 2002. **114**(7): p. 1269-1271.
88. Ondarçuhu, T. and C. Joachim, Drawing a single nanofibre over hundreds of microns. EPL (Europhysics Letters), 1998. **42**(2): p. 215.
89. Liu, G., et al., Polystyrene-block-poly(2-cinnamoylethyl methacrylate) Nanofibers—Preparation, Characterization, and Liquid Crystalline Properties. Chemistry – A European Journal, 1999. **5**(9): p. 2740-2749.
90. Deitzel, J.M., et al., Controlled deposition of electrospun poly(ethylene oxide) fibers. Polymer, 2001. **42**(19): p. 8163-8170.
91. Doshi, J. and D.H. Reneker, Electrospinning process and applications of electrospun fibers. Journal of Electrostatics, 1995. **35**(2–3): p. 151-160.
92. Ki, C.S., et al., Characterization of gelatin nanofiber prepared from gelatin–formic acid solution. Polymer, 2005. **46**(14): p. 5094-5102.
93. Demir, M.M., et al., Electrospinning of polyurethane fibers. Polymer, 2002. **43**(11): p. 3303-3309.
94. Darrell, H.R. and C. Iksoo, Nanometre diameter fibres of polymer, produced by electrospinning. Nanotechnology, 1996. **7**(3): p. 216.

95. Fong, H., I. Chun, and D.H. Reneker, Beaded nanofibers formed during electrospinning. Polymer, 1999. **40**(16): p. 4585-4592.
96. Deitzel, J.M., et al., The effect of processing variables on the morphology of electrospun nanofibers and textiles. Polymer, 2001. **42**(1): p. 261-272.
97. Son, W.K., et al., The effects of solution properties and polyelectrolyte on electrospinning of ultrafine poly(ethylene oxide) fibers. Polymer, 2004. **45**(9): p. 2959-2966.
98. Zuo, W., et al., Experimental study on relationship between jet instability and formation of beaded fibers during electrospinning. Polymer Engineering & Science, 2005. **45**(5): p. 704-709.
99. Zong, X., et al., Structure and process relationship of electrospun bioabsorbable nanofiber membranes. Polymer, 2002. **43**(16): p. 4403-4412.
100. Gupta, P., et al., Electrospinning of linear homopolymers of poly(methyl methacrylate): exploring relationships between fiber formation, viscosity, molecular weight and concentration in a good solvent. Polymer, 2005. **46**(13): p. 4799-4810.
101. Kim, H.S., et al., Morphological Characterization of Electrospun Nano-Fibrous Membranes of Biodegradable Poly(L-lactide) and Poly(lactide-co-glycolide). Macromolecular Symposia, 2005. **224**(1): p. 145-154.

Chapter 2

The Effects of Electrospinning Parameters On The Morphology of Polyaniline/Poly(ethylene oxide) Nanofibers

2.1 Abstract

Electrospinning is a simple but efficient way to produce continuous polymer fibers with diameters ranging from several nanometers to microns. We investigated the effects of polymer blend composition, degree of dilution and collecting distance on fiber diameter and morphology of porous fiber webs for various diluted PANI/PEO solutions in an electrospinning process. Polyaniline was dissolved in chloroform at 12, 26, 45, 52 and 68wt.% of PANI content ratios, and the solutions were spun and collected at 15 and 30cm separation . The average diameters of PANI/PEO nanofibers ranged from 328 to 544nm. We found that distance was not a major factor on the diameter of nanofibers; rather, it was found to be a sensitive function of solution viscosity where fiber diameter decreased as viscosity decreased. But a threshold was found where below a critical viscosity 10 CPs, the diameter started to increase and junction or droplet defects started to form.

2.2 Introduction

Electrospinning has been regarded as a convenient method for the fabrication of polymer fibers with controlled diameters ranging from tens of nanometers to micrometers[1]. An electrostatically driven jet sprays into fibers and they are collected as random-direction non-woven mat or membrane with high surface to volume ratio[2, 3]. Various polymers or their composites have been successfully electrospun with particular diameter ranges by controlled electrospinning parameters. This technology has attracted a lot of interests in recent years due to the interesting physical, chemical and biological properties of the electrospun fibers[4]. Especially the fibers with small diameters were recognized with diverse and numerous potential applications, including gas sensor based polymer fibers[5], filtration[2], nonwoven fiber webs have been used as catalyst[6]supports and tissue engineering[7, 8].

Conducting polymers have been developed very fast recently in various applications including chemical sensors[9-11], metallic materials in electronic devices[12, 13], electromagnetic radiation shielding[14] or interconnects in circuits. Polyaniline is one of the most investigated electrically conductive polymers. It exists in three oxidation states and they are classified with leucoemeraldine, emeraldine and pernigraniline. Emeraldine base polyaniline is recognized as one of the most useful forms of polyaniline due to high stability at room temperature, and the fact that, the resulting polyaniline salt is electrically conductive upon doped with acid. Its polymer chain mainly consists of half

benzenoid structure-imine site which interacted with oxidation regents and quinoid rings-imine sites which react with reducing or protonating regents. In base form, emeraldine base polyaniline is insulating. Upon exposure to acid medium, the nitrogen of imine is protonated on the polymer chain so that the structure transforms into electrically conducting salts. The rigid backbone due to a high degree of aromaticity makes the elasticity of the solution insufficient for electrospinning[15]. To solve this problem, researchers have explored several non-conductive hosting polymers such as poly(ethylene oxide), polyvinylpyrrolidone and cellulose acetate which have been used to assist polyaniline to form composite fibers[16, 17].

In this work, we report the estimation of PANI content (mg/ml) after filtering by UV-Vis. Using the electrospinning method, we produce electrospun polyaniline/poly(ethylene oxide) composite nanofibers with polyaniline content ranging from 12wt.% to 68wt.%. We also report the colleting distance and dilution effect on the diameter and morphology of the PANI/PEO nanofibers.

2.3 Experimental

2.3.1 UV-Vis of unfiltered and filtered PANI/PEO solutions

A 0.6:1 mole ratio of camphor-sulfonic acid (HCSA) and polyaniline was dissolved in 10ml chloroform to 1.65wt.% concentration. The solution was magnetically stirred for 12 hours at room temperature, followed by 5 minutes of sonication and 5 minutes of

stirring. This process was repeated six times. The precursor was separated into two parts. The first part was diluted by adding chloroform as solvent to the following concentrations: 0.01, 0.02, 0.03, 0.04, 0.05, 0.06 and 0.07mg/ml. After 5 minutes of sonication to make them uniform, the solutions were used for UV-visible spectra. The second part was filtered through a 0.2µm PTFE membrane syringe filter. The uniform solutions were also diluted to the same degree as the first part precursor. After sonication for 5 minutes, they were used for UV-Vis.

2.3.2 Electrospinning PANI/PEO nanofibers

The uniform green PANI solution filtered by syringe filter and 0.5wt.% poly(ethylene oxide) (PEO) were used as electrospinning precursors. Samples for electrospinning were prepared by mixing two solutions at volume ratios of PANI to PEO at 20:80, 40:60, 60:40, 66.7:33.2 and 80:20, respectively.

The five mixture precursors were contained in a glass syringe and were electropun at room temperature at different collecting distances: 15cm and 30cm. The syringe pump was kept at a constant speed of 0.3ml/h to feed the solution for electrospinning. The voltage applied on the tip of the nozzle was 4.5kV, 5kV, 5kV, 5kV and 5.5kV, respectively for the 20:80, 40:60, 60:40, 66.7:33.2 and 80:20 PANI/PEO (v/v) solutions.

The solution with the least amount of carrier hosting PEO had the lowest viscosity. To get nanofibers without beads, the precursors had to be diluted. The collecting distance

was fixed at 15cm and the feed rate was 0.3ml/h for all electrospinning precursors. The 20:80 PANI/PEO (v/v) solution was diluted by 10v%, 30v% and 50v%. The applied voltages were all at 4.5kV. The 40:60 PANI/PEO (v/v) solution was diluted by 10v%, 30v% and 50v%. The electrospinning voltages were 5kV. The 60:40 PANI/PEO (v/v) solution was diluted by 10v%, 20v% and 30v%. 5kV was used for electrospinning. Also, the 80:20 PANI/PEO (v/v) solution was diluted by 10v%. 5.5kV was applied to assist the formation of nanofibers.

2.4 Results and Discussion

2.4.1 Characterization of UV-Vis of HCSA doped PANI solutions before and after filtering

Figure 2.1(a and b) shows the UV-Vis of PANI solution before (a) and after (b) filtering. Three absorption peaks were observed. The 365nm wavelength peak represents π- π* transitions in the benzenoid structure; with the shoulder-like 437nm wavelength, this peak reflects the protonation (doping) on the nitrogen of imine. The peak next to 770nm wavelength reflects the excitation formation in the quinoid rings. This strong peak was attributed to the presence of localized polarons in a coil-like conformation of the polymer chain[18]. With dilution degree increasing, the absorbance decreased. With increasing dilution, the absorbance decreases.

It is known that the UV-Vis spectra of emeraldine base polyaniline without dopants shows the benzenoid and quinoid peaks and their absorbance are almost the same because EB polyaniline consists of equi-molar ratios of amine and imine. The third peak characteristic of EB polyaniline is hpsochromically shifted to near 800nm wavelength due to the protonation with an acid[19]. Thus, the absorbance ratio of benzenoid and quinoid structures was used to estimate the oxidation state of HCSA doped PANI. The oxidation degree of PANI calculated before and after filtering was 1.1 and 1.6, respectively. The changed in oxidation states may be attributed to limited solubility of undoped PANI particles existed in the unfiltered PANI solution which could impact the absorbance of benzenoid and quinoid peaks. In contrast, the filtered solution was uniform.

2.4.2 Estimation of filtered PANI content

Since polyaniline is composed of benzenoid and quinoid structures, so the 365nm and 770nm wavelength peaks were selected to calculate the filtered PANI content. The benzenoid structure peak (365nm wavelength) of unfiltered diluted PANI solutions from figure 2.1.(a) were selected to plot the calibration curve worked as baseline as shown in figure 2.2.(a). The linear fitting rate of this figure is 20.6 (AU)/(mg/ml). The weight lost before and after filtering is assumed to be linear. By using the filtered diluted benzenoid structure peaks from figure 2.1.(b) and the linear relationship A=20.6x(where A represents the 365nm wavelength absorbance of filtered PANI), the filtered PANI

content(x) was calculated and plotted as shown in figure 2.2.(a). By comparing the ratio between $x_{unfiltered}$ and $x_{filtered}$ in this figure, the PANI weight percent change was 67wt.% and the filtered PANI content was estimated to be 3.3 mg/ml. Similarity, the linear relationship of quinoid peaks from figure 2.1.(b) was calculated to be A=32.4x, yielding a 52wt.% change and the filtered PANI content of 4.7 mg/ml was calculated from figure 2.2(b). Consequently, the polyaniline content ranged between 3.3 mg/ml and 4.7 mg/ml. The polyaniline content was assumed to be the average of two estimation. The transformation from volume ratios of PANI/PEO to weight ratios is shown in table 2.1. The actual PANI wt.% in the precursors ranged from 12 to 52wt.%

2.4.3 Viscosities of different composition of PANI/PEO solutions

Shear rate of the nozzle for different compositions of PANI/PEO solutions were calculated by $\upsilon = \frac{4Q}{\pi r^3}$ as shown in table 2.2, where Q represents the flow rate (ml/h) and r is the needle radius (cm). Since the flow rate was kept constant at 0.3ml/hr and the needle radius was fixed at 0.01525cm, the shear rate was 29.9 s^{-} for all compositions.

Since the viscosity of HCSA doped PANI solution is too low to be electrospun into nanofibers, PEO has been found to be a good carrier host for electrospinning by increasing the solution's viscosity. Figure 2.3 shows that the viscosity of PANI/PEO as a function of the PANI content. The viscosity of pure PANI solution was 1.4 CPs and the individual PEO

solution's viscosity was above 200 CPs, indicating that the more PEO content, the more viscous the solution.

2.4.4 The effect of colleting distance on the diameter and morphology of PANI/PEO nanofibers

Figure 2.4 through 2.8 show the diameter distributions and SEM images of PANI/PEO nanofibers electrospun at 12wt.%, 26wt.%, 45wt.%, 52wt.% and 68wt.% PANI content at 15cm and 30cm collecting distances. The counts-fiber diameter distribution plots were fitted by Lorentz model. The kurtosis describes the statistical frequency curve of the mean of the distribution. The skew represents the tail direction of the distribution. The morphology of the fibers changed gradually from individual nanofibers to junction of nanofibers and to an unstable morphology as the PANI content (wt.%) increased.

Figure 2.9 shows that the average fiber diameter became larger with increasing voltage especially between 5 kV and 5.5 kV where fiber diameter increased around 70%. But the percent change in trying to reduce fiber diameter by going to even lower voltages is seen to be rather modest. Figure 2.10 shows that the average diameter of PANI/PEO nanofibers at each composition did not change much (<10%) when the collecting distance increased from 15cm to 30cm which mean that these distances exceeded the critical distance of fiber stretching and solvent evaporation. In all, the viscosity of solution it the most important effect on controlling fiber diameter. Nanofibers with higher PANI content

had larger average diameters. Higher PANI content solutions have too little hosting polymer PEO to assist in the fiber stretching process to form stable fiber morphologies. This is also reflected in the solution viscosity being below the threshold value of 10 CPs.

2.4.5 Dilution (Viscosity) Effect on diameter and morphology of PANI/PEO nanofibers

PANI/PEO nanofibers with PANI content of 12, 26, 45 and 68wt.% were selected to investigate the dilution effect on fiber diameter and morphology. Figure 2.11 to 2.14 show fiber diameter distributions and SEM images of fiber morphology as a function of dilution. The Lorentz distribution, kurtosis and skewness were also described.

The viscosity of PANI/PEO solutions depend on the content of the carrier hosting PEO. The 12wt% PANI/PEO without dilution exhibited the highest viscosity 70.4CPs. The 68wt.% PANI/PEO solution diluted by 10v% had the lowest viscosity 3.93CPs. Figure 2.15 shows rather linear relationships in decreasing viscosity as a function of dilution by volume percent for all the compositions.

Figure 2.16 shows the different voltages used for electrospinning PANI/PEO nanofibers. The applied voltage was a function of PANI/PEO composition not its dilution. Four PANI/PEO compositions were electrospun at 4.5, 5, 5, 5.5kV. Even though it was observed that the average diameter became bigger as the voltage increased, however,

the differences in the applied voltages among each composite were small, which indicates the charge density applied at the tip of nozzle was nearly the same. Thus, voltage was not a very important effect on the fiber diameter and morphology of nanofibers in this study.

In general, as the viscosity of the solution decreased the diameter of the nanofibers also decreased. Figure 2.17 shows how the average diameter of PANI/PEO with 12wt.% PANI gradually decreased with higher dilution. In contrast, for 26wt.%, 45wt.% and 68wt.% PANI/PEO nanofibers, an even lower viscosity resulted in larger diameter nanofibers because the solutions were not viscous enough for the carrier hosting PEO to make the nanofibers stretch further to form thinner fibers.

2.5 Conclusions

The absorbance peaks of UV-visible spectra of HCSA doped PANI solutions before and after filtering were used to estimate the filtered PANI content (4mg/ml). Different composition of PANI/PEO nanofibers were electrospun through controlling electrospinning parameters. The applied voltage and collecting distance played minor effects on the diameter of fibers. Dilution (viscosity) had the largest effect leading the way to the smallest fiber diameters. The average diameter became smaller when dilution degree increased, however, a threshold in minimum viscosity was found where the carrier hosting PEO was not enough to make the nanofibers stretch further to form thinner fibers, leading to increasing fiber diameters and droplet defects.

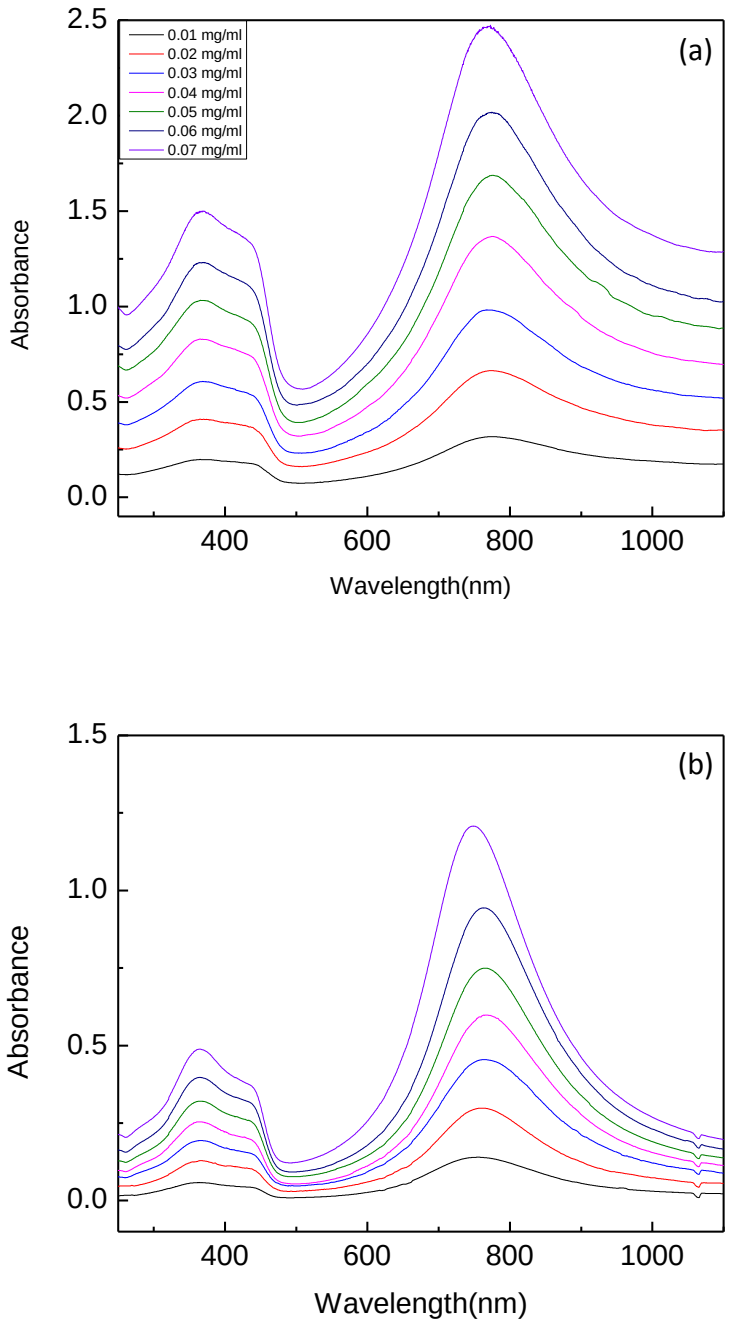

Figure 2.1 UV-visible spectra of (a)unfiltered HCSA doped PANI with different dilution concentrations (b) PTFE syringe filter filtered HCSA doped PANI solution with same dilution degrees as unfiltered HCSA doped PANI solutions

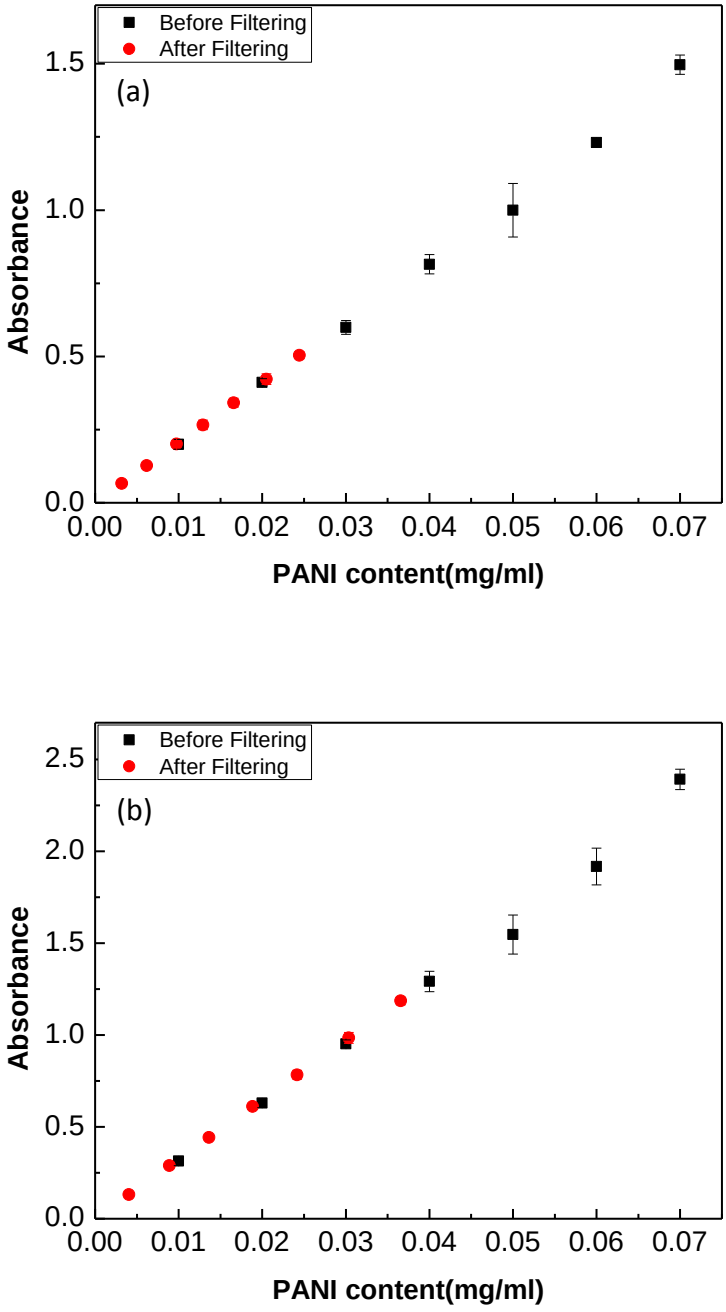

Figure 2.2 Calibration curve comparison of UV-visible absorbance at (a) 365nm and (b)770nm wavelength of HCSA doped PANI before and after filtering

Table 2.1 Calculation of filtered PANI content in PANI/PEO blends

PANI/PEO (v/v)	PANI/PEO (ml)	W_{PANI} in PANI/PEO blends(mg)	W_{PEO} in PANI/PEO blends(mg)	PANI wt.% in PANI/PEO blends	PANI wt.% range in the blends
80:20	4:1	16	7.45	68	64-72
66.7:33.3	3.33:1.67	13.32	12.44	52	47-54
60:40	3:2	12	14.9	45	40-49
40:60	2:3	8	22.35	26	23-30
20:80	1:4	4	29.8	12	10-14

PANI content: 4mg/ml; PEO content:7.45mg/ml , chloroform density: 1.483g/ml

Table 2.2 Shear rates of different composition of PANI/PEO solutions in the needle

PANI content (wt.%)	12	26	45	52	68
Flow rate (Q) (ml/h)	0.3	0.3	0.3	0.3	0.3
Shear rate (v) (s^{-1})	29.9	29.9	29.9	29.9	29.9

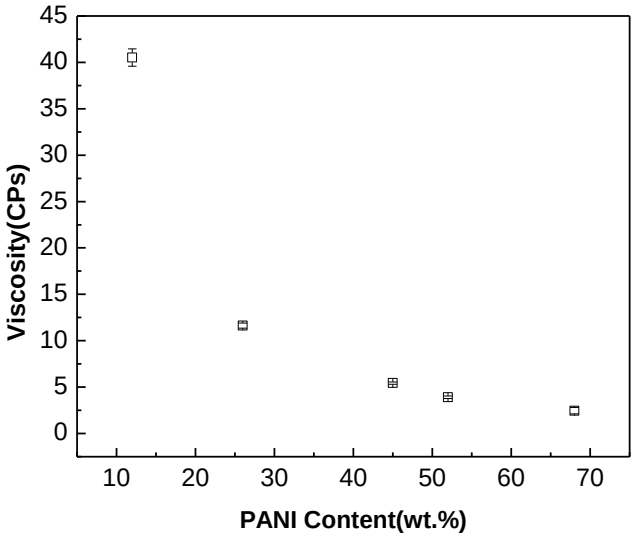

Figure 2.3 Viscosities of different composition of PANI/PEO solutions

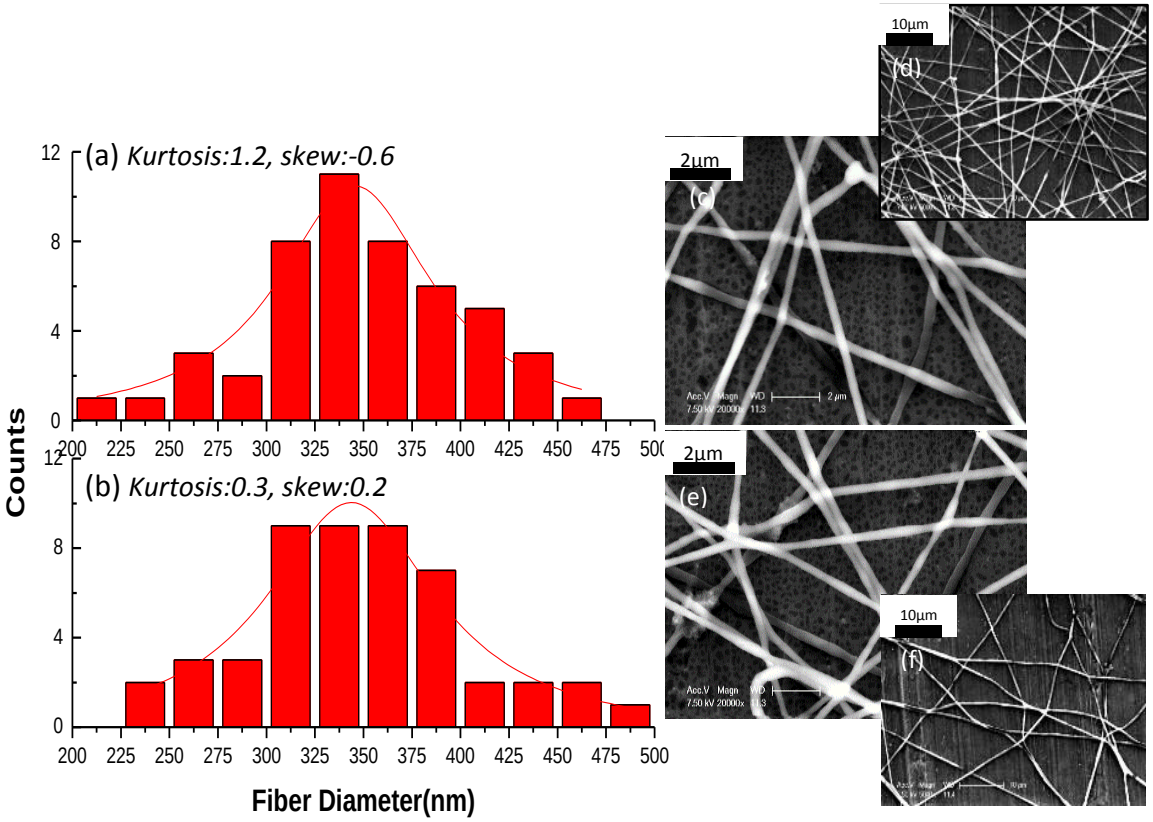

Figure 2.4 Fiber diameter distribution (a, b) and SEM images of (c-f) of the electrospun 12 wt.% PANI PANI/PEO nanofibers with varying the distance between collector and spinneret: 15 cm (a-c) and 30 cm (d-f). The applied voltage and flow rate were fixed at 4.5kV and 0.3 ml/hr, respectively.

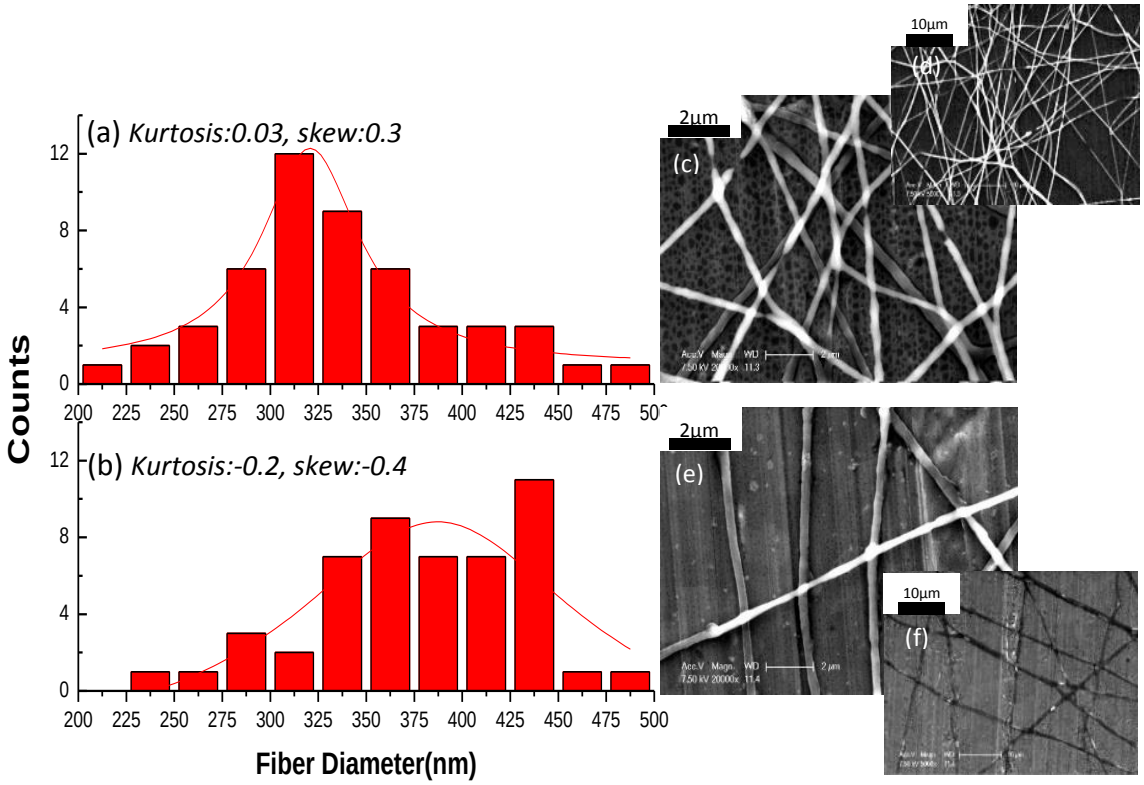

Figure 2.5 Fiber diameter distribution (a, b) and SEM images of (c-f) of the electrospun 26 wt.% PANI PANI/PEO nanofibers with varying the distance between collector and spinneret: 15 cm (a-c) and 30 cm (d-f). The applied voltage and flow rate were fixed at 5 kV and 0.3 ml/hr, respectively.

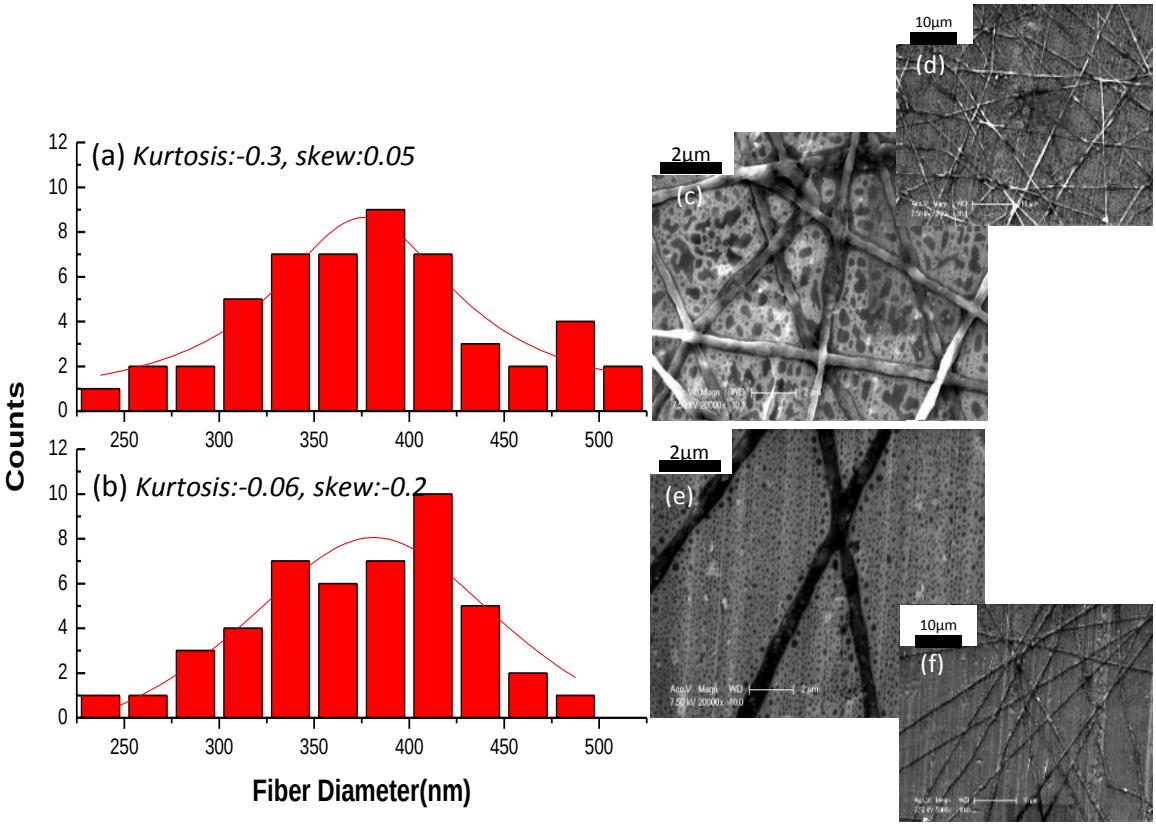

Figure 2.6 Fiber diameter distribution (a, b) and SEM images of (c-f) of the electrospun 45 wt.% PANI PANI/PEO nanofibers with varying the distance between collector and spinneret: 15 cm (a-c) and 30 cm (d-f). The applied voltage and flow rate were fixed at 5 kV and 0.3 ml/hr, respectively.

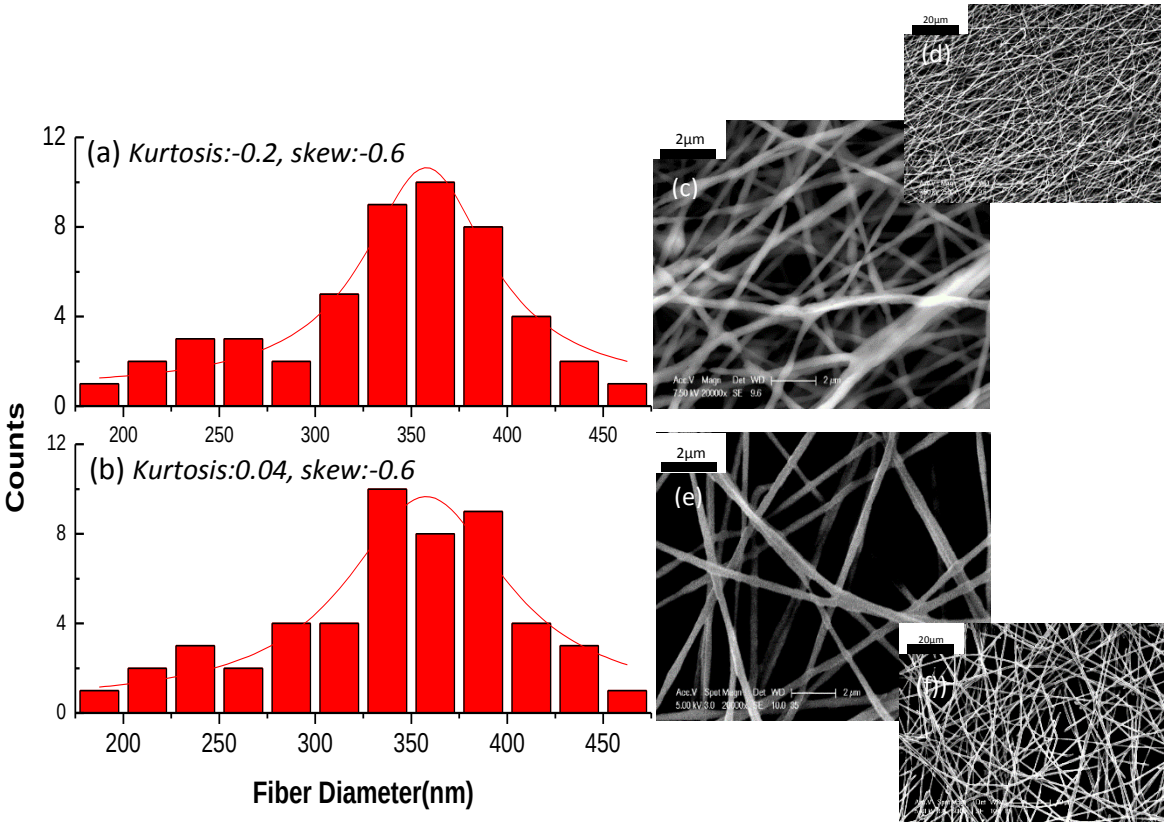

Figure 2.7 Fiber diameter distribution (a, b) and SEM images of (c-f) of the electrospun 52 wt.% PANI PANI/PEO nanofibers with varying the distance between collector and spinneret: 15 cm (a-c) and 30 cm (d-f). The applied voltage and flow rate were fixed at 5 kV and 0.3 ml/hr, respectively.

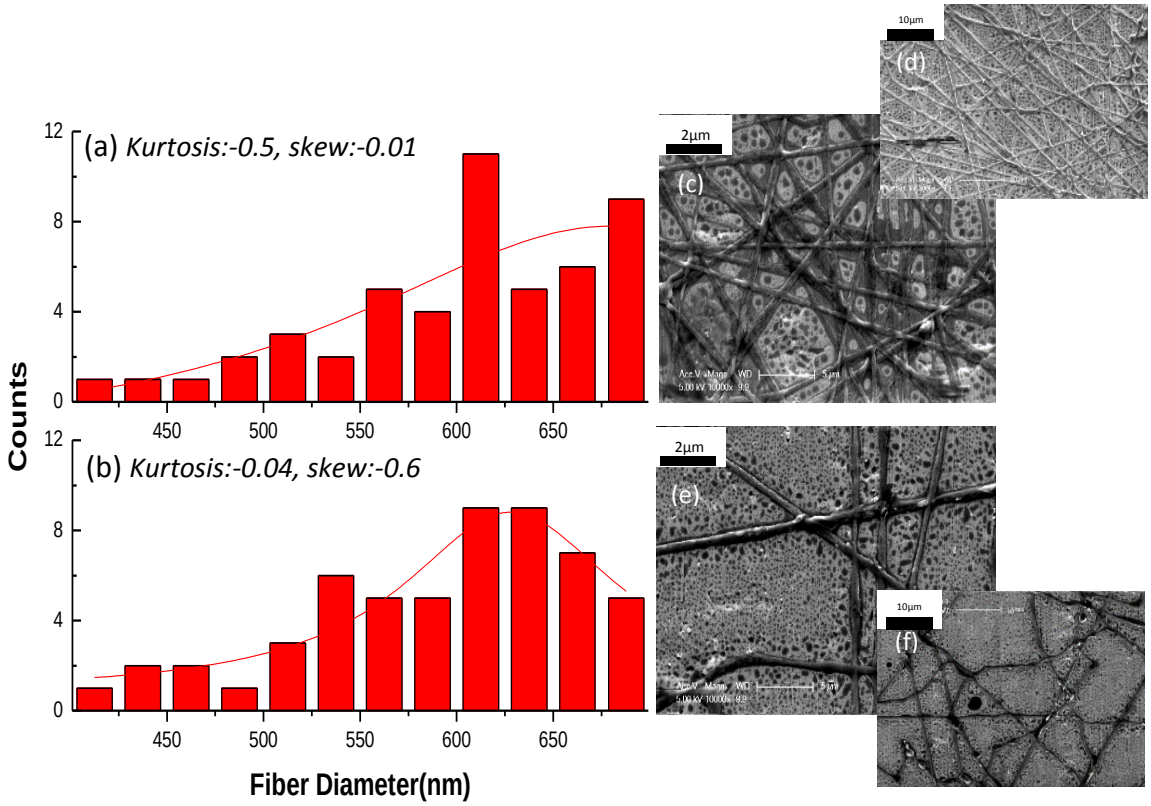

Figure 2.8 Fiber diameter distribution (a, b) and SEM images of (c-f) of the electrospun 68 wt.% PANI PANI/PEO nanofibers with varying the distance between collector and spinneret: 15 cm (a-c) and 30 cm (d-f). The applied voltage and flow rate were fixed at 5.5 kV and 0.3 ml/hr, respectively.

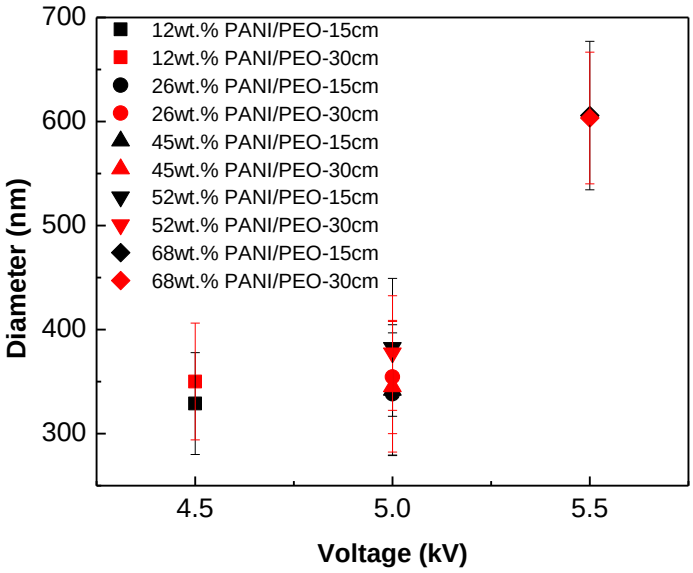

Figure 2.9 The effect of applied voltage on the diameters of different compositions of PANI/PEO nanofibers

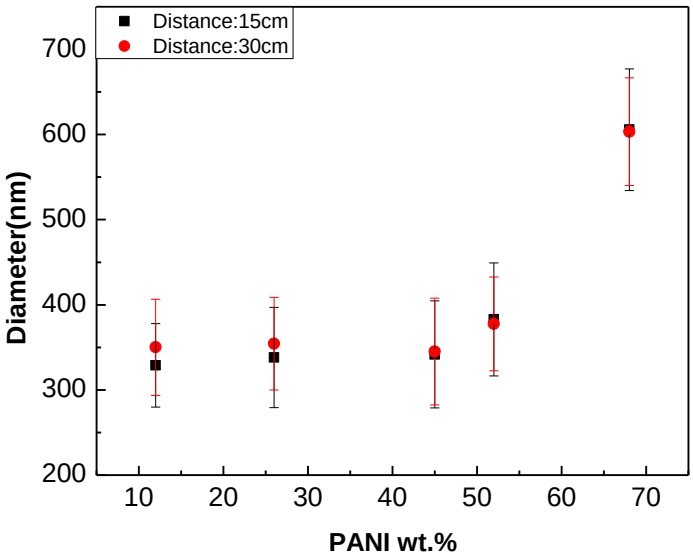

Figure 2.10 The effect of composition and distance between collector and needle on the diameter of electrospun nanofibers

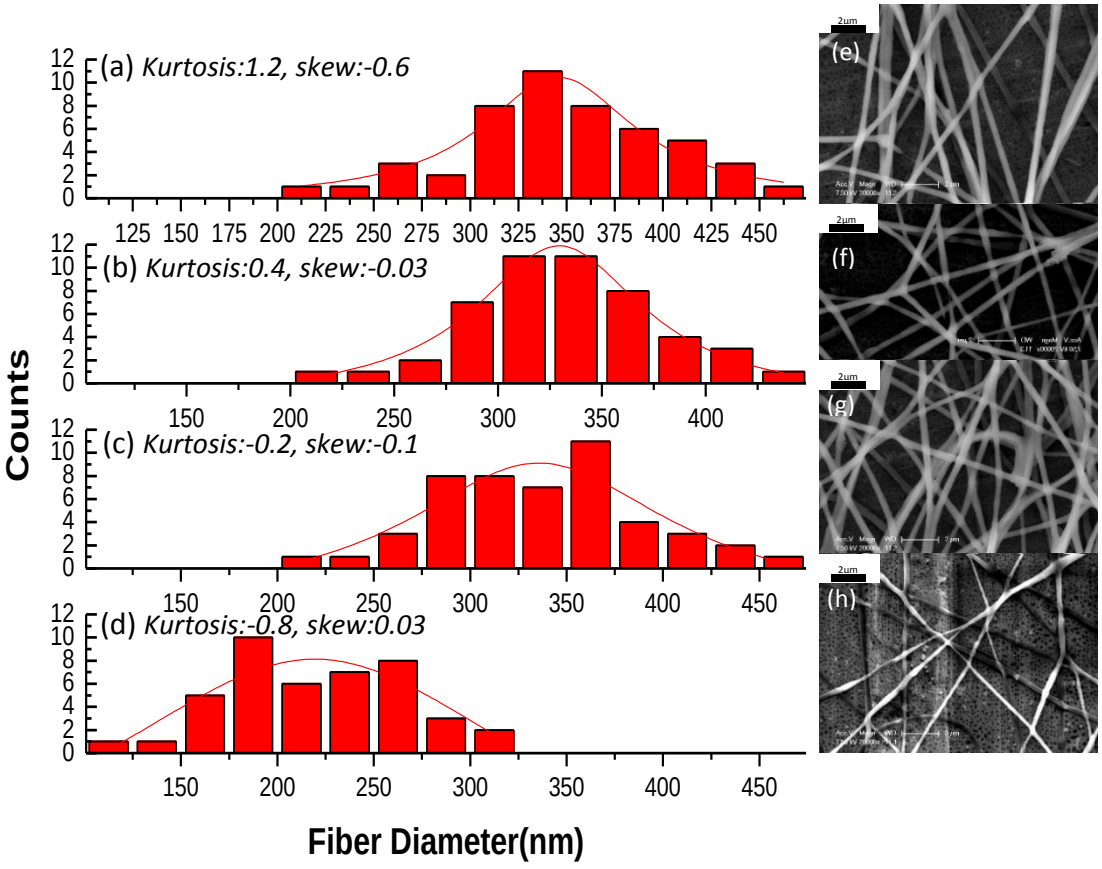

Figure 2.11 Fiber diameter distributions and SEM images of 12 wt% PANI/PEO nanofiber at 4.5 kV as function of different dilution degrees: (a, e) no dilution, (b, f) 10 v%, (c, g) 30 v%, (d, h) 50 v%.

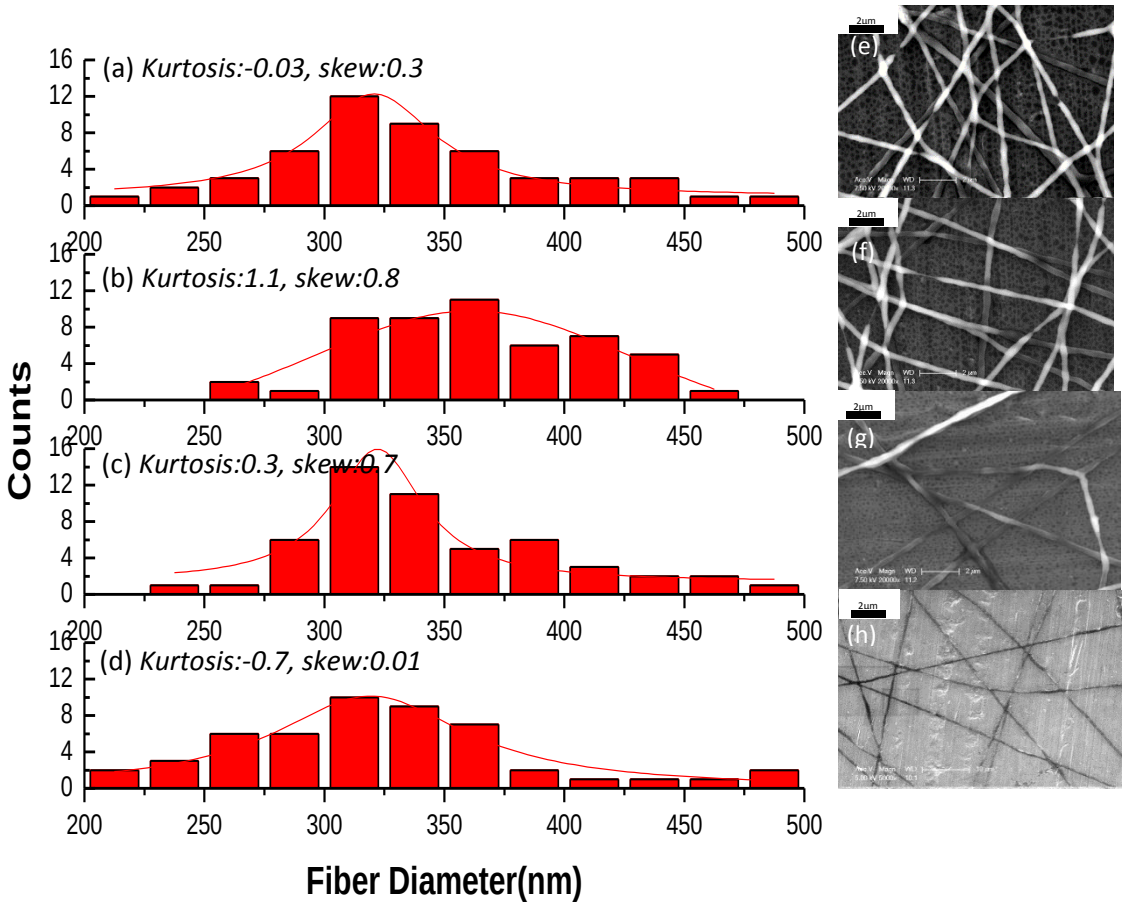

Figure 2.12 Fiber diameter distributions and SEM images of 26 wt% PANI/PEO nanofiber at 5 kV as function of different dilution degrees: (a, e) no dilution, (b, f) 10 v%, (c, g) 30 v%, (d, h) 50 v%.

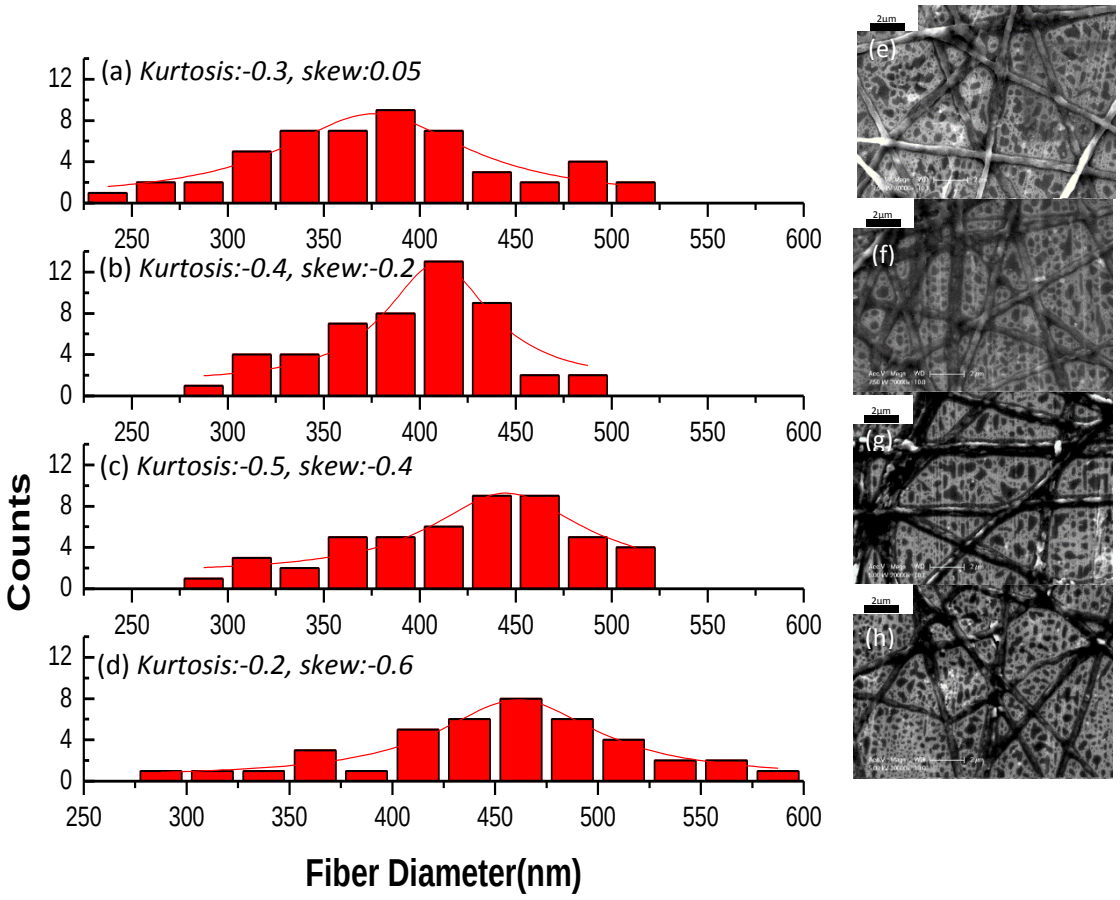

Figure 2.13 Fiber diameter distributions and SEM images of 45 wt% PANI/PEO nanofiber at 5 kV as function of different dilution degrees: (a, e) no dilution, (b, f) 10 v%, (c, g) 20 v%, (d, h) 30 v%.

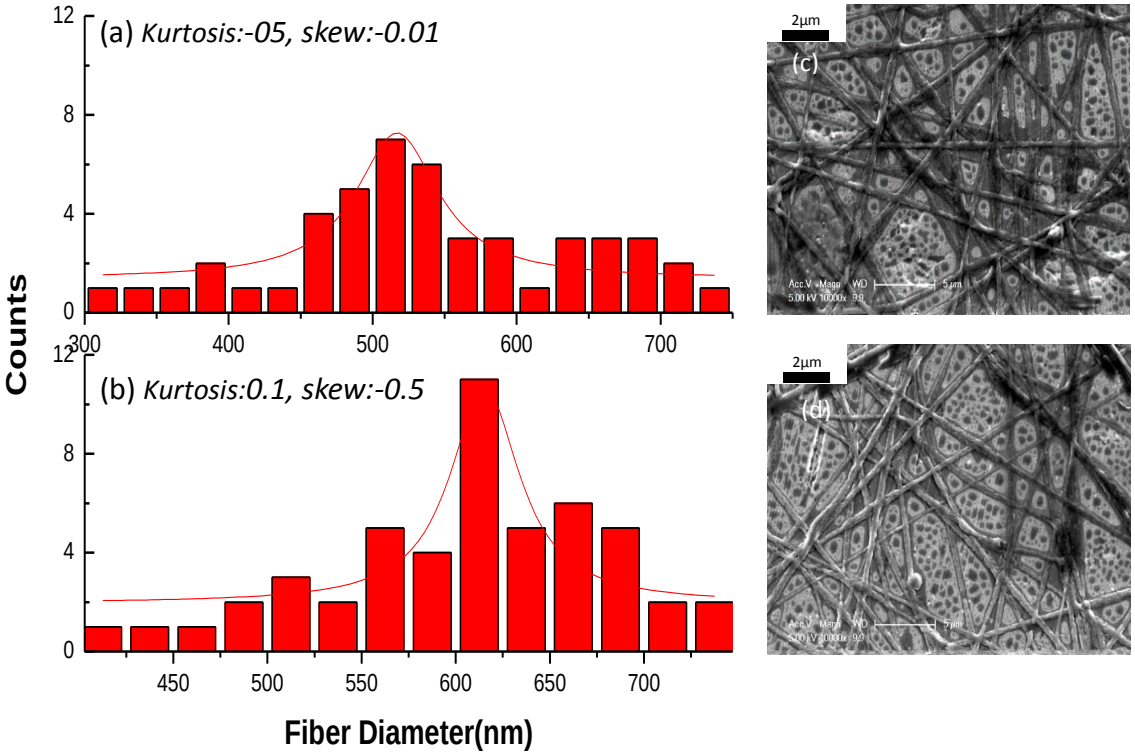

Figure 2.14 Fiber diameter distributions and SEM images of 68 wt% PANI/PEO nanofiber at 5.5 kV as function of different dilution degrees: (a, c) no dilution, (b, d) 10 v%.

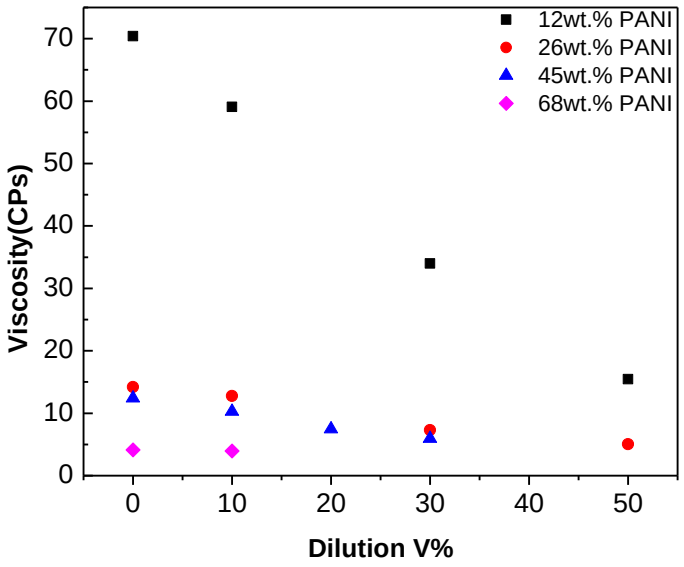

Figure 2.15 Relationship between solution viscosities and dilution degrees of different composition of PANI/PEO solutions

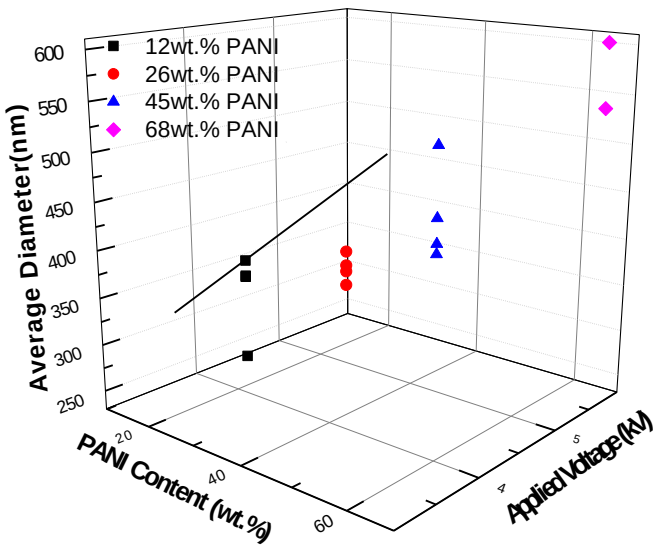

Figure 2.16 The effect of applied voltage on the diameters of electrospun nanofibers

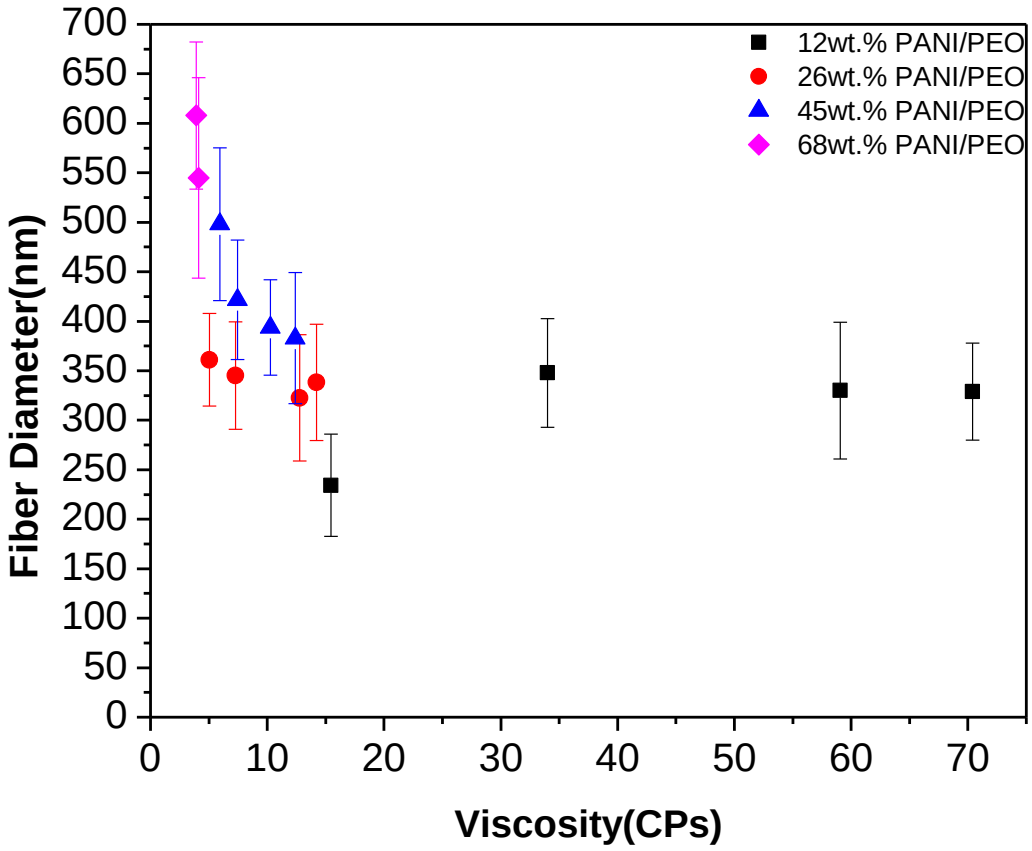

Figure 2.17 Average electrospun nanofibers diameter as function of solution viscosity

References

1. Fridrikh, S.V., et al., Controlling the Fiber Diameter during Electrospinning. Physical Review Letters, 2003. **90**(14): p. 144502.
2. Abdel-Ghani, M.S. and G.A. Davies, Simulation of non-woven fibre mats and the application to coalescers. Chemical Engineering Science, 1985. **40**(1): p. 117-129.
3. Han, T., D.H. Reneker, and A.L. Yarin, Buckling of jets in electrospinning. Polymer, 2007. **48**(20): p. 6064-6076.
4. Huang, Z.-M., et al., A review on polymer nanofibers by electrospinning and their applications in nanocomposites. Composites Science and Technology, 2003. **63**(15): p. 2223-2253.
5. Krupenkin, T.N., et al., Reversible Wetting−Dewetting Transitions on Electrically Tunable Superhydrophobic Nanostructured Surfaces. Langmuir, 2007. **23**(18): p. 9128-9133.
6. Stasiak, M., et al., Polymer Fibers as Carriers for Homogeneous Catalysts. Chemistry – A European Journal, 2007. **13**(21): p. 6150-6156.
7. Yoshimoto, H., et al., A biodegradable nanofiber scaffold by electrospinning and its potential for bone tissue engineering. Biomaterials, 2003. **24**(12): p. 2077-2082.
8. Yang, F., et al., Electrospinning of nano/micro scale poly(l-lactic acid) aligned fibers and their potential in neural tissue engineering. Biomaterials, 2005. **26**(15): p. 2603-2610.
9. Stutzmann, N., R.H. Friend, and H. Sirringhaus, Self-Aligned, Vertical-Channel, Polymer Field-Effect Transistors. Science, 2003. **299**(5614): p. 1881-1884.
10. Gelinck, G.H., T.C.T. Geuns, and D.M. de Leeuw, High-performance all-polymer integrated circuits. Applied Physics Letters, 2000. **77**(10): p. 1487-1489.
11. Koezuka, H., A. Tsumura, and T. Ando, Field-effect transistor with polythiophene thin film. Synthetic Metals, 1987. **18**(1–3): p. 699-704.
12. Bao, Z., A. Dodabalapur, and A.J. Lovinger, Soluble and processable regioregular poly(3‐hexylthiophene) for thin film field‐effect transistor applications with high mobility. Applied Physics Letters, 1996. **69**(26): p. 4108-4110.
13. Pinto, N.J., et al., Dual input AND gate fabricated from a single channel poly(3-hexylthiophene) thin film field effect transistor. Journal of Applied Physics, 2006. **99**(8): p. 084504-084504-5.
14. Yu, J.H., S.V. Fridrikh, and G.C. Rutledge, The role of elasticity in the formation of electrospun fibers. Polymer, 2006. **47**(13): p. 4789-4797.
15. Zhou, Y., et al., Fabrication and electrical characterization of polyaniline-based nanofibers with diameter below 30 nm. Applied Physics Letters, 2003. **83**(18): p. 3800-3802.

16. Bai, H., et al., Composite nanofibers of conducting polymers and hydrophobic insulating polymers: Preparation and sensing applications. Polymer, 2009. **50**(14): p. 3292-3301.
17. Kessick, R. and G. Tepper, Electrospun polymer composite fiber arrays for the detection and identification of volatile organic compounds. Sensors and Actuators B: Chemical, 2006. **117**(1): p. 205-210.
18. Grummt, U.-W., et al., Polyaniline based optical pH sensor. Analytica Chimica Acta, 1997. **357**(3): p. 253-259.
19. Wang, Y. and X. Jing, Effect of solution concentration on the UV–vis spectroscopy measured oxidation state of polyaniline base. Polymer Testing, 2005. **24**(2): p. 153-156.

Chapter 3

Electric Properties Characterization and Sensing Performance of PANI/PEO Nanofibers

3.1 Abstract

Camphor-10-sulfonic acid (HCSA) doped PANI/PEO with different composition (12 to 52wt.% of PANI) were synthesized and their properties including optical, electrical and sensing properties were systematically investigated. FT-IR shows that an increase of IR absorbance ratios of aromatic C-C stretching vibration of benzenoid rings to C=N stretching vibration of quinoid rings which confirmed that PANI content in nanofiber mats increased proportionally with increase in PANI content in electrospinning solution. The band gap of PANI was determined to be 2.5 eV using UV-vis spectroscopy technique. The electrical conductivities of the nanofibers increased with an increase in the PANI content in the nanofibers. Additionally, the sensitivity ($\Delta R/R\%$ [%/ppm]) toward NH_3 increased as the PANI content increased, but branched nanofibers reduced sensing performance. The humidity sensitivity changed from positive to negative as the PANI content increased. The electron transport mechanism was studied by measuring temperature dependent electrical conductivity. The negative temperature coefficient of resistance revealed a semiconducting behavior of PANI/PEO nanofiber. The activation energy was calculated by

Arrhenius plot and shows and increasing as the PANI content decreased. The Power Law indicated that holes were being transported in a three dimensional matrix, and the longer hopping distance required more hopping energy for hole transport.

3.2 Introduction

The ability to detect gaseous species in the atmosphere, especially those gases which are harmful to humans has attracted a great deal of concern in the medical field and near industrial manufacturing sites. Thus, the investigation into new materials to improve gas sensor technology has been under rapid developed in recent years. Typically, a gas sensor is characterized by several performance features including sensitivity, selectivity, response time, recovery time, low and upper detection limit, stability, reproducibility and durability [1, 2]. The sensitivity of a gas sensor is strongly dependent on the surface to volume ratio of the material, where in general higher surface to volume ratios materials yield a higher sensitivity response [3, 4].

Although the electrospinning has been known for over 70 years, it has been receiving a greater attention in the past decade because its ability to form micron and nanofibers with controlled morphology and dimension[5-7]. The resulting electrospun fibers are collected as random- distribution fibrous webs with high specific surface areas. The electrospun fibers can be aligned to construct parallel one-direction nanostructures. Furthermore, the properties such as strength, weight, surface variation and porosity can be investigated based on the specific polymer [8].

Conducting polymers have been recognized as novel materials because their chemical and mechanical properties can be easily altered so that they perform like semiconductors and metals. Polyaniline is one of the most studied conducting polymers

due to its ease of synthesis, high stability at room temperature, and can be made electrically conductive by doping with acids. The conductivity mainly depends on the oxidation states and doping degree [9, 10].

In this work, we present the morphology change of different compositions of PANI/PEO nanofibers and their electrical response to NH_3 and water vapor. We also report the thickness effect on the sensing performance by selecting 52wt.% PANI/PEO fiber mats. Fourier transform infrared spectroscopy is used to determine the PANI content within composite nanofibers. Moreover, their resistance as a function of temperature was used to characterize the electron transport mechanism for each of the PANI/PEO nanofibers.

3.3 Experimental Details

3.3.1 Electrospun PANI/PEO nanofibers with different composition

The preparations of electrospinning solution were described in sections 1.2.1 and 1.2.2. Precursors for electrospinning were prepared by mixing two solutions according to the PANI weight percentage (wt.%): 12, 26, 45 and 52, respectively. The solutions were fed through a glass syringe which resists the corrosive nature of chloroform. The applied voltages were varied between 4.5, 5, 5 and 5 kV. The distance between collector and needle was fixed at 15cm with a feed rate of 0.3ml/hr.

3.3.2 Gas sensing measurements

For gas sensing studies, the PANI/PEO fiber mats coated with gold electrodes were integrated onto a pin chip holder by wire bonding (West Bond Inc. Model 7443A), and subsequently loaded on the printed circuit board designed to interface with the chip holder and sensing system. Each sensor was subjected to a 0.5 V, and the current was continuously monitored by a LabView program. The resistance was determined by applying Ohm's law. A baseline resistance was established by flowing dry air as a carrier gas. Once stabilized, different analyte concentrations were introduced into the system by subsequent dilutions of the carrier gas. Exposure times were set up to be 15 minutes and recovery times were limited to 20 minutes. Analyte and carrier gas flow rates were adjusted by a mass flow controller (Alicat Scientific Incorporated).

3.4 Results and Discussion

3.4.1 Material synthesis and characterization

Fiber diameter and morphology are important factors controlling the electrical properties and sensing performance of nanofibers. As already pointed out, achieving a high surface area to volume ratio is critical when optimizing sensing performance[11]. Thus, to determine the PANI content and fiber thickness effects on conductivity and sensing properties, electrospinning parameters were controlled to yield nanofibers with comparable diameters for each composition. Figure 3.1 shows the diameter distribution

of PANI/PEO nanofibers from solutions with 12, 26, 45 and 52 wt.% PANI contents. The average diameter of each blend was 366, 345, 339 and 324 nm, respectively. Figure 3.2 shows that the morphology of the 12 and 26wt% PANI/PEO nanofibers were individual. However, the fused nanofibers were observed when the PANI content increased to 45 and 52wt.%. This may be attributed to lower solution's viscosity which may lead to incomplete solvent evaporation and not enough fiber hosting for stretching during the in-flight electrospinning process.

The chemical structure of the electrospun PANI/PEO nanofibers was determined using FT-IR analysis. The FT-IR spectra PANI/PEO composite nanofibers is shown in figure 3.3. The presence of characteristic IR absorption peaks due to quinoid and benzenoid rings at 1466 cm^{-1} and 1612 cm^{-1} indicate the aromatic C=N stretching vibration of quinoid and aromatic C-C stretching vibration of benzenoid rings. 1307 cm^{-1} and 1167 cm^{-1} are due to aromatic amine stretching. The peak at 832 cm^{-1} attributed to the out-of-plane hydrogen deformation of aromatic rings in the PANI unit sequences. Except for the characteristic peaks, the absorption band at 1043 cm^{-1} was assigned to an S=O stretching vibration. Furthermore, for PEO structure, 1099 cm^{-1} and 2950 cm^{-1} (corresponding to C-O-C vibrational modes and CH_2 stretching modes), and 850-970 cm^{-1} (corresponding to CH_2 rocking) were observed. The 1612 cm^{-1} peaks representing a PANI structure was chosen to compare with the 1099 cm^{-1} peaks which represent a PEO structure[12-14]. The transmittance ratios of T_{1612}/T_{1099} were 0.066, 0.071, 0.112 and 0.165, respectively for

PANI/PEO nanofibers with PANI contents of 12, 26, 45, 52 wt.%. The increase in the ratios indicates that the PANI content in the composite increased.

The transparency of the green PANI/PEO fiber mats was determined by measuring optical transmittance, which was carried out with a UV-visible spectrophotometer in the range 300-1100nm. Figure 3.4 shows optical transmittance (T) spectra of as-prepared different compositions of PANI/PEO nanofibers based on the Kulbeka-Munt Function. It is known that intrinsically PANI is insulating. The sulfonic group from HCSA protonates the nitrogen on the imine and induces charge carriers, meaning that the band gap responsible for electron excitation changes by doping. The second peak which represents the protonation level was chosen to make linear fitting and the intercept with x axis is the band gap for the PANI oxidation state. The calculated band gaps of PANI/PEO nanofibers were 2.5 eV independent of the composition as shown in figure 3.5, which correspond to the normal range of band gap for polyaniline oxidation states[15, 16].

Figure 3.6 to figure 3.9 show dektak images of thickness at specific electrospinning times for each composition of PANI/PEO nanofibers, and the measurement was selected on the same spot on the collecting substrate. The effect of electrospinning time on fiber mat thickness is plotted in figure 3.10. Longer electrospinning time resulted in thicker fiber mats. However, the deposition rate (figure 3.11) is different. Fiber mats with higher PANI contents had lower deposition rates. That is because when the electrospinning solution was charged by the applied voltage, the higher PANI content solutions, which are

more conductive, had higher charge densities. The nanofibers would repulse each other over larger distances, leading to a larger deposition area yielding thinner fiber mats.

3.4.2 Composition effect on electrical characterization

A thickness around 800nm was selected from the four composites fiber mats to study the PANI content effect on their electrical properties and sensing performance. As shown in figure 3.12, the PANI/PEO nanofibers were collected on a 1cm by 1cm SiO_2/Si substrate. 300nm thick gold electrodes were sputtered on top of the fiber mats using shadow mask. The width of the fiber mat was approximately 4 mm and the gap between electrodes was approximately 1 mm.

The resulting linear current-voltage (I-V) curves reveal that the contact between the fiber mat and gold electrode were ohmic at room temperature (figure 3.13). Since PEO is a non-conductive polymer, acting only as a carrier host to assist the formation of nanofibers, the HCSA doped PANI is responsible for electrical conduction. Figure 3.14 shows that the PANI/PEO nanofibers with the higher PANI content were more conductive. Note the conductivity with PANI content is not a linear relationship probably due to the porosity and surface variation effects.

3.4.3 Composition effect on sensing performance

The sensing performance of individual sensors was investigated as a function of composition of the conductive polymer PANI and host carrier PEO towards NH_3 and water. The dynamic response processes were operated at room temperature. Figure 3.15 shows the real-time response of different compositions of PANI/PEO nanofibers exposed to different concentrations of NH_3. The sensing response ($\Delta R/R$) increases as the NH_3 concentration increases because the fiber mat absorbs more NH_3 molecules over the same area. The real-time NH_3 response to different compositions of PANI/PEO nanofibers are compared in figure 3.16. These results clearly show that high mat conductivity did not correlate with high sensitivity by noting that the fiber mat with 26wt.% PANI shows the optimal sensitivity even though it was not the most conductive. In this experiment, sensing performance of fiber mats was more a function of fiber morphology. For example, we attribute the poor sensing performance of fiber mat samples with 45 and 52wt.% PANI to the presence of fusion of nanofibers which reduces the surface area to volume ratio. Also, undulating and "wet" surface of the fibers were caused by the delayed drying and the stress relaxation behavior of fibers at lower viscosities, which absorbed a lot of NH_3 molecules on the surface and less gases reacted with PANI. The sensing mechanism of PANI/PEO nanofiber is shown in figure 3.17. After NH_3 molecules adsorb into the nanofibers, which destroys the conduction path, the nitrogen atoms on the imine are deprotonated, which decreases the charge carrier density on the polymer chain[11].

The calibration curves clearly show that fiber mats with 26wt.% PANI content displayed the best sensing performance among the four compositions (figure 3.18 and 3.19). The response time was calculated by 90% resistance change within the 15 minutes analyte exposure time. It was observed that fiber mat with 26wt.% took the longest time to response to NH_3, even though it had the highest sensitivity (figure 3.20). The recovery time was calculated at 75% resistance change compared the saturation resistance (figure 3.21). For each composite, lower NH_3 concentrations took longer time to react with the fiber mats. The low analyte density decreased the absorption rate onto the fiber mats, which means their response was reduced.

The humidity sensing data for different composition of PANI/PEO nanofibers is shown in figure 3.22, 3.23. In each composition, as the humidity increased the sensitivity increased. However, the sensing curves were shifting - the response went out of normal range when the humidity was at greater than RH 50%. Because PEO is a hydrophilic polymer, the water molecules went into the nanofibers- the PEO bulk change was not a physical swelling process. PEO reacted with water and this process disturbed the stability of the conduction mechanism and ΔR. The humidity response transformed from positive to negative in a continuous way as the PANI content increased. That is because the swelling process, which increases resistance, was reduced in contrast as the interaction between PANI and water molecules increased, which induced more charge carriers. The reaction mechanisms between HCSA doped PANI and water molecules are shown in figure 3.24. The water molecules forms hydrogen bond with nitrogens on amine and

protonation with imine, which enhances the conductivity[6]. The calibration curve is shown in figure 3.25.

3.4.4 Temperature dependent of resistance

HCSA doped polyaniline is conductive and the PEO is non-conductive polymer, so the ratio of PANI to PEO effect on the electron hopping mechanism is an attractive property to be investigated. Figure 3.26 shows the I-V response of PANI/PEO nanofibers with same thickness around 800nm as a function of temperature. The current-voltage plot showed an ohmic contact between the nanofibers and gold electrodes for a voltage range of -0.5 to 0.5. The contact changed from ohmic to Schottky or even went open at a critical temperature with temperature decreasing.

The resistivity of PANI/PEO nanofibers at different temperatures were calculated as shown in figure 3.27. The resistivity increases as the temperature decreases. However, the resistivity alone is not sufficient to characterize these materials. Electron transport properties of conducting polymer are unique because they are composed of 1-dimensional chains that have both polydispersity and packing arrangement of degree of disorder in addition to doping level. Thus, the charge carriers are transported intra-chain or inter-chain by a hopping mechanism. The appropriate model for conducting polymers can be described by temperature-dependent charge transport. The negative temperature coefficient of resistance (TCR) shown in figure 3.28, describes as $R^{-1}(dR/dT)=\alpha$, indicates

the semiconducting behavior of the electrospun composites[17]. The less conductive nanofibers had more negative semiconducting behavior. Semiconducting behavior was further substantiated by a resistance-sensitive region at high temperature and the resistance tending to saturation at low temperature as shown in figure 3.29. The resistance-sensitive region fits an Arrhenius relationship at high temperature, with an increasing activation energy as the PANI content (wt.%) decreases as shown in figure 3.30. The more non-conductive PEO existing in the matrix, the less charge carriers, which requires more energy for electron transport. For disordered materials with localized carriers, such as conducting polymers, a more insightful parameter for the metal insulator transition is the reduced energy, $W = d[\ln(\sigma)]/d[\ln(T)]$ as shown in figure 3.31, producing a positive slope for metallic transport, a negative slope for insulating behavior, and a zero slope in the critical regime[18]. The PANI/PEO nanofibers with 12 wt.% PANI exhibited a negative slope, indicating that the insulating behavior resulted in the least ordered composite. The relatively weak temperature-dependent changes in the W value for the 52 wt.% PANI/PEO nanofibers suggest the mat is approaching the critical regime. On the other hand, PANI/PEO nanofibers with 26 wt.% and 45 wt.% PANI exhibited positive slopes of 0.0185 and 0.0137, respectively, demonstrating less disorder than the nanofibers with 12 wt.% and 52 wt.% PANI. This phenomenon may be attributed to the fusion of nanofibers with 45 wt.% and 52 wt.% PANI, having a higher disorder degree than that of 26 wt.% PANI/PEO nanofibers. Since PANI/PEO nanofibers with 26 wt.% exhibited

the highest metallic behavior, the sensitivity towards NH_3 showed optimal performance as shown in figure 3.16.

In the VRH model, the temperature T dependence of conductivity σ follows the relation

$$\sigma = \sigma_o \exp[-(\frac{T_o}{T})]^{1/r}$$

where T_0 is the Mott characteristic temperature and σ_o the conductivity at $T = \infty$. T_0 and are determined by the localization length, the density of states and the hopping distance in the material. The r is determined by the dimension of researching system. For 1D, 2D and 3D dimensional systems, r is equal to 2, 3 and 4, respectively. Figure 3.32 showed the power law plots, where the 3D VHR model gave the highest correlation coefficient, meaning that the electron transportation was three-dimensional. According to the 3D VHR model, the dc conductivity is given by

$$\sigma = \sigma_o \exp[-(\frac{T_o}{T})]^{1/4} \qquad \text{Eq. (a)}$$

$$\sigma_o = e^2 v R^2 N(E) \qquad \text{Eq. (b)}$$

$$T_o = \lambda\alpha/kN(E \qquad \text{Eq. (c)}$$

$$T_o = \lambda\alpha/kN(E) \qquad \text{Eq. (d)}$$

$$W = 3/4\pi R^3 N(E) \qquad \text{Eq. (e)}$$

where *e* is the electronic charge, v is a hopping frequency, λ≈18.1 is a dimensionless constant, α is the inverse rate of fall of the wave function, *k* is Boltzmann's constant, N(E) is the density of states at the Fermi level[19, 20].

The values of the parameters T_o and σ_o can be obtained from the slope and from the intersection with the conductivity axis from figure 3.32, respectively. Then the hopping distance and hopping energy were also calculated as shown in figure 3.33 and figure 3.34. The more conductive PANI/PEO matrix shorten the hopping distance, thus, requiring less hopping energy for electron transport, while the less conductive PANI/PEO nanofibers (high PEO content) increase the hopping distance for electron movement, thus, requiring more energy to excite electron transport.

3.4.5 Thickness effect on sensing performance

Thicknesses of 0.82µm, 1.15µm, 3.57µm and 5.24µm fiber mats with 52wt.% PANI content were selected to study the thickness effect on the gas sensing performance. The dektak (sic) images are shown in figure 3.35. The current-voltage (I-V) curves in figure 3.36 proved that the sputtered gold made ohmic contact with the fiber mats. The resistance obtained from linear rate of I-V curves showed that the thicker fiber mats had lower resistance as shown in figure 3.37. The conductivity of the four samples shown in figure 3.38 were at similar order range.

Figure 3.39 shows the real-time response of different thicknesses of 52wt.% PANI/PEO when exposed to different concentrations of NH_3. For high NH_3 concentrations ranging from 25ppm, 50ppm and 100ppm, the thicker fiber mats showed higher resistivity. This is because thicker fiber mats have more reaction area for the same amount of NH_3 molecules. In contrast, the thinner fiber mats were more sensitive to low NH_3 concentration because thinner fiber mats have excellent surface area to volume ratios and NH_3 diffusion takes place over shorted times. Figure 3.40 clearly shows the thickness effect on sensitivity to different concentrations of NH_3. As mentioned before, thicker fiber mats have a higher density reaction area to the same concentration of analyte, so thinner fiber mats responded with longer time as shown in figure 3.41. Since thicker fiber mats absorbed more analyte, they take a longer time to release the gas molecules to recover toward the baseline shown in figure 3.42.

3.5 Conclusions

We have synthesized electrospun fibers of molar ratio 1:0.6 PANI doped with HCSA blended with PEO ranging from 12wt.% to 52wt.% PANI contents in the composite. The conductivities of the PANI-blend fibers mats were found to increase with the weight percent of polyaniline in the fibers. Ohmic contact sensors were made by sputtering gold as the electrodes. The sensing of NH_3 showed that increasing the PANI content enhances the sensitivity, but branched nanofibers significantly reduced sensing performance.

Moreover, the humidity sensitivity could be tuned from positive to negative by varying the PANI/PEO ratio, meaning that swelling process was reduced with enhancing water protonation. The electron transport mechanism was investigated by measuring the sensors' TCR. The negative temperature coefficient of resistance indicates a semiconducting behavior of PANI/PEO nanofibers. The activation energy increased with the decreasing of PANI content (wt.%). The Power Law revealed that the charge carriers are being transported in a three-dimensional matrix, and the longer hopping distance requires more hopping energy for electron transport.

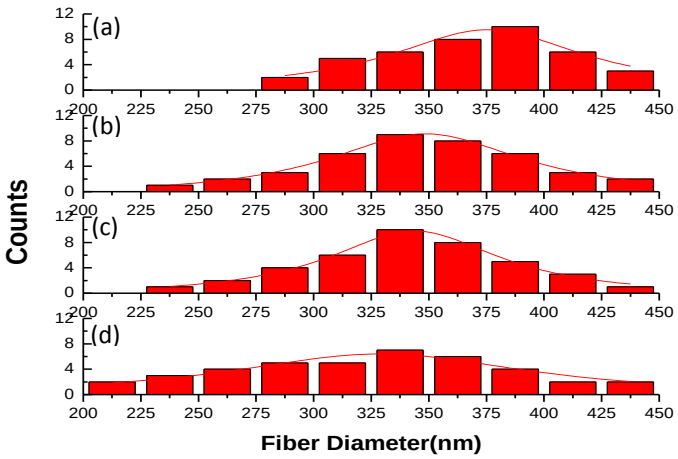

Figure 3.1 Diameter distributions of different composition of PANI/PEO nanofibers with PANI content (wt.%) (a)12 (b)26 (c)45 (d)52

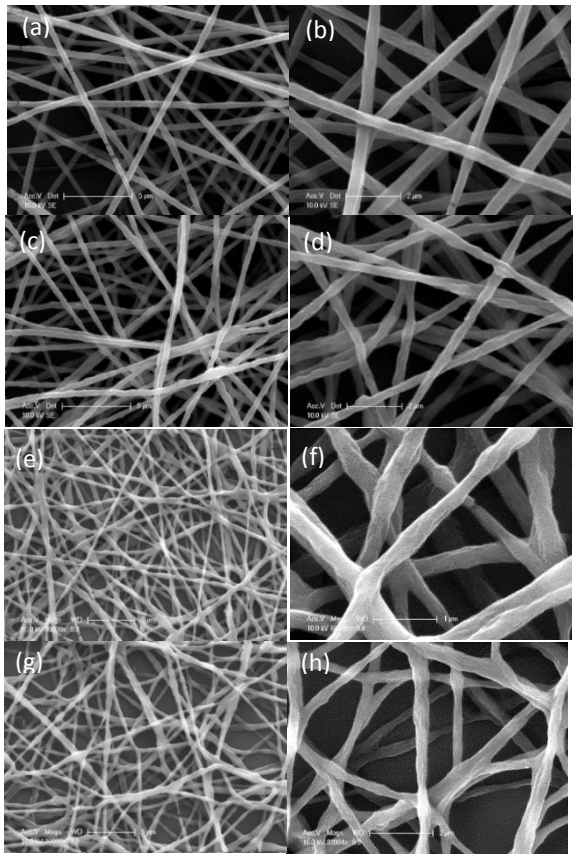

Figure 3.2 Scanning electron microscopy images of the electrospun PANI/PEO nanofibers with PANI content(wt.%): (a)(b)12, (c)(d)26, (e)(f)45, (g)(h)52.

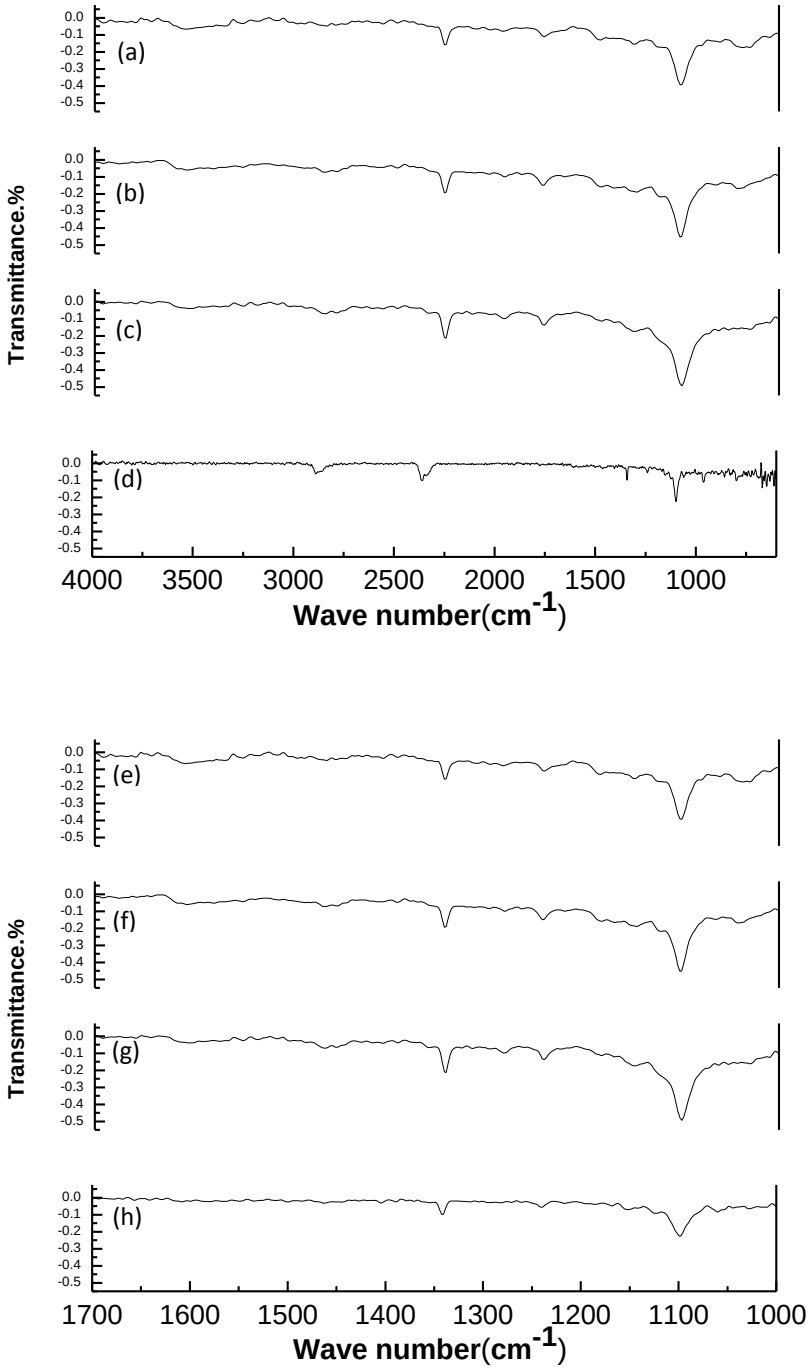

Figure 3.3 FT-IR of different compositions of PANI/PEO nanofibers (a)(e)12wt.% PANI (b)(f)26wt.% PANI (c)(g)45wt.% (d)(h)52wt.% with various wave number (cm^{-1}) range

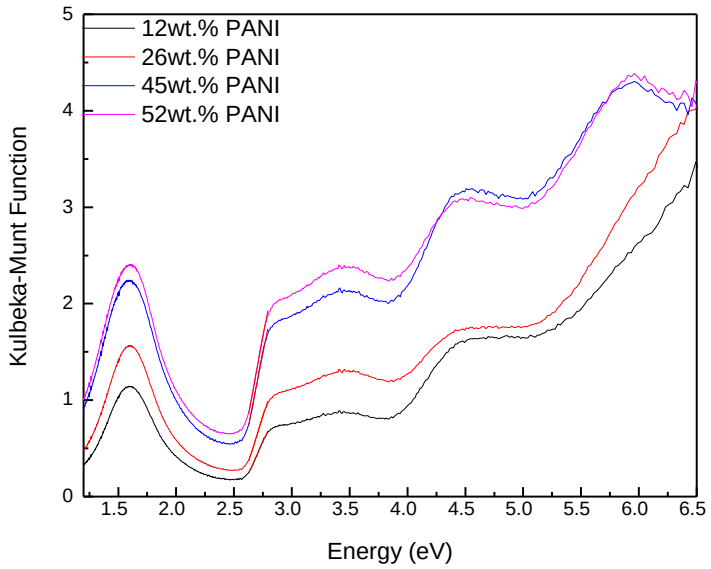

Figure 3.4 Direct energy band gap of PANI/PEO fiber mats

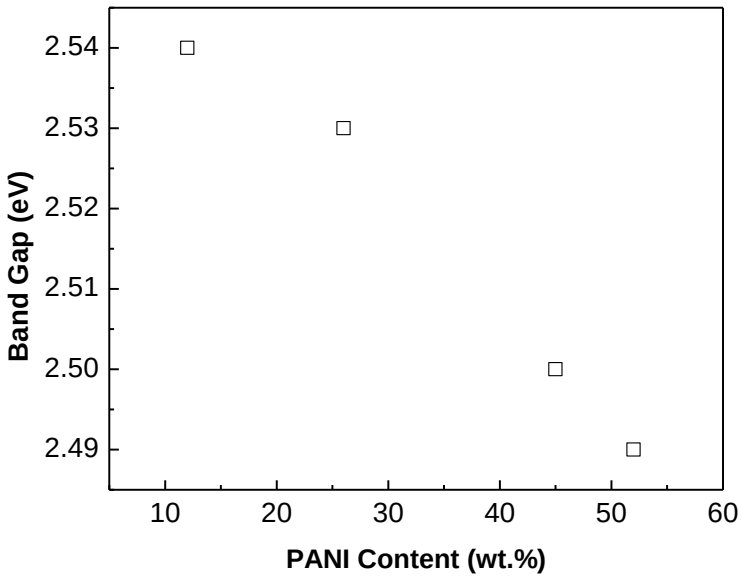

Figure 3.5 Band gap for HCSA doped PANI

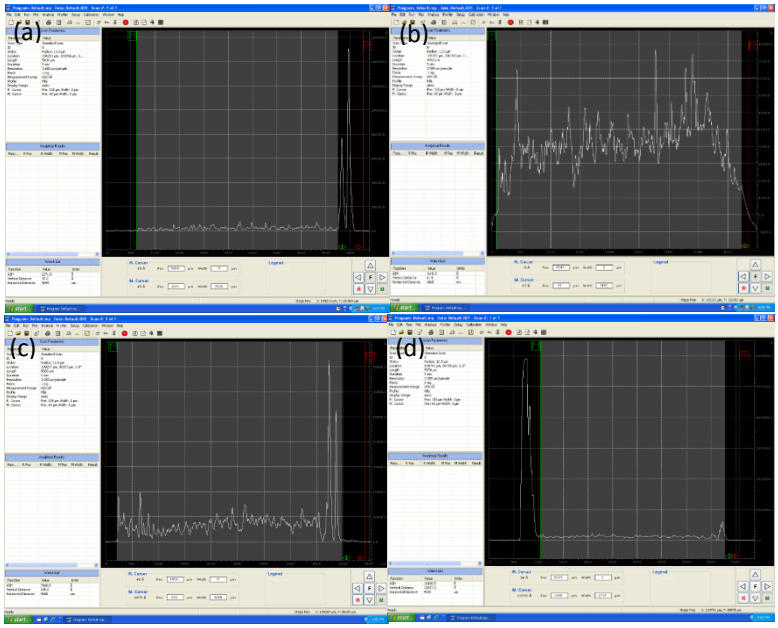

Figure 3.6 Dectak images of electrospun 12wt.% PANI/PEO nanofibers with different electrospinning time: (a)2.5min (b)5min (c)7.5min (d)10min

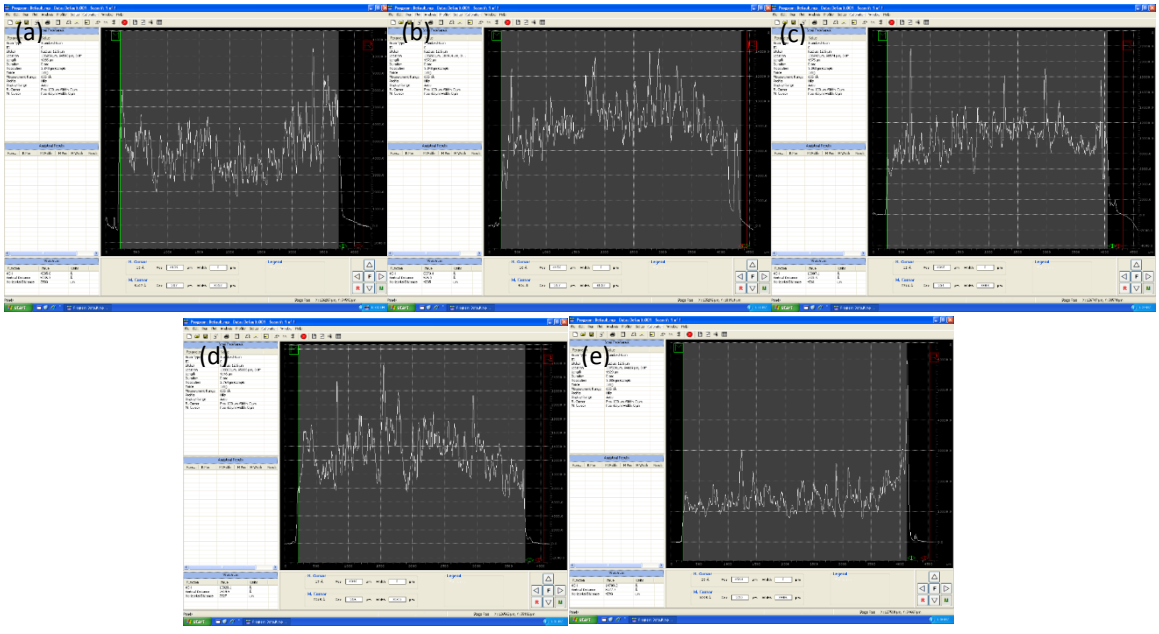

Figure 3.7 Dectak images of electrospun 26wt.% PANI/PEO nanofibers with different electrospinning time: (a)10min (b)15min (c)20min (d)25min (e)30min

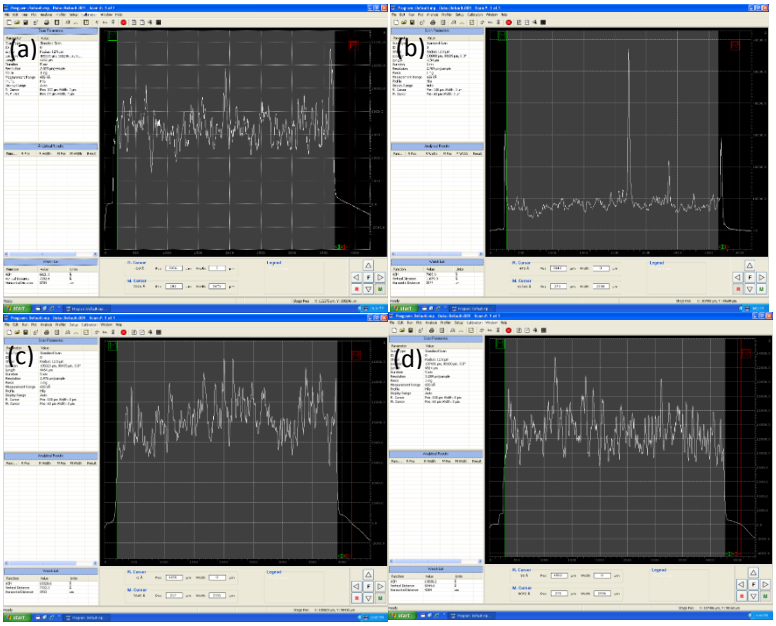

Figure 3.8 Dectak images of electrospun 45wt.% PANI/PEO nanofibers with different electrospinning time: (a)15min (b)20min (c)25min (d)30min

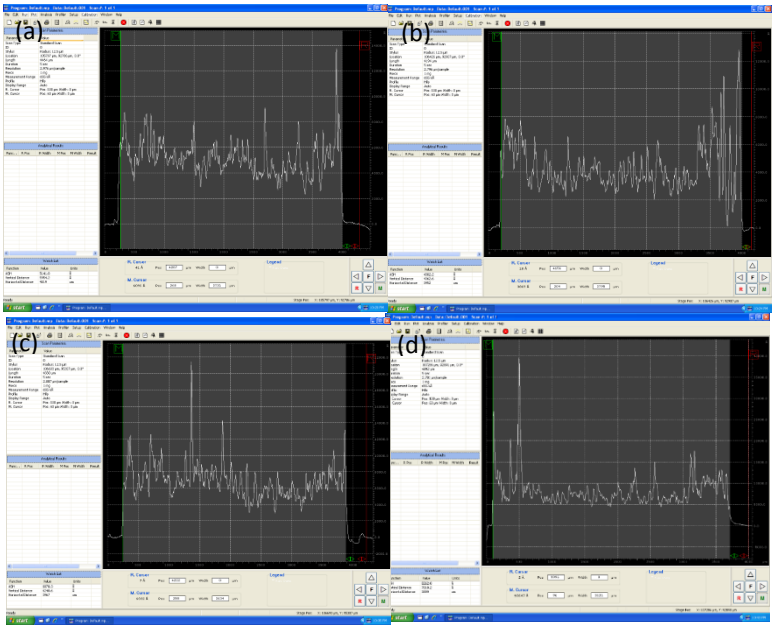

Figure 3.9 Dectak images of electrospun 52wt.% PANI/PEO nanofibers with different electrospinning time: (a)15min (b)20min (c)25min (d)30min

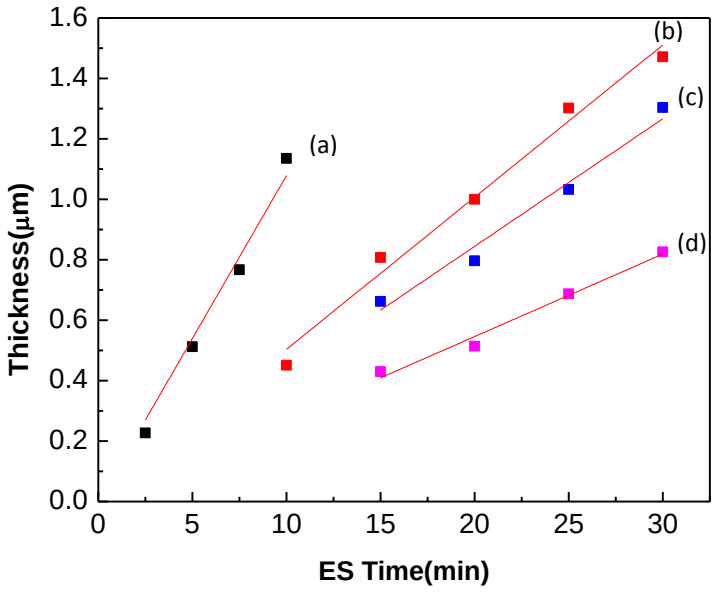

Figure 3.10 Electrospinning time effect on the thickness of different composition of PANI/PEO fiber mats. PANI content (wt.%): (a)12 (b)26 (c)45 (d)52

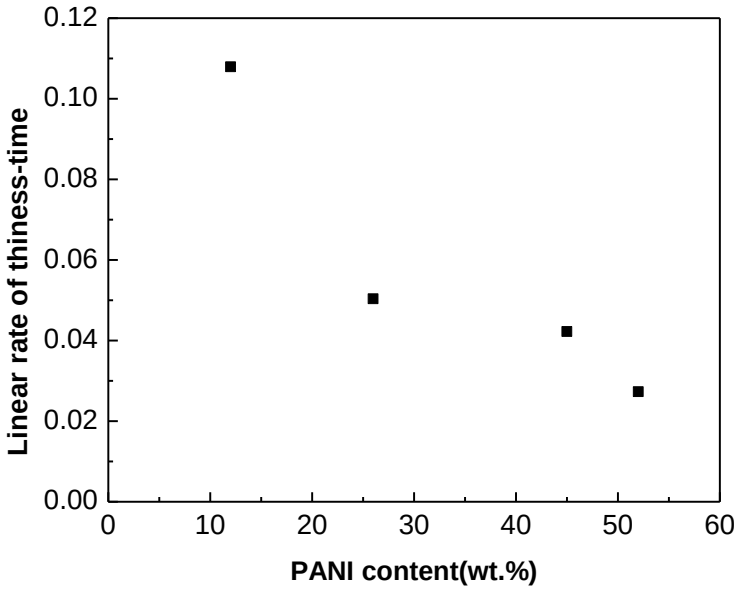

Figure 3.11 Linear rate of different composition of PANI/PEO fiber mats

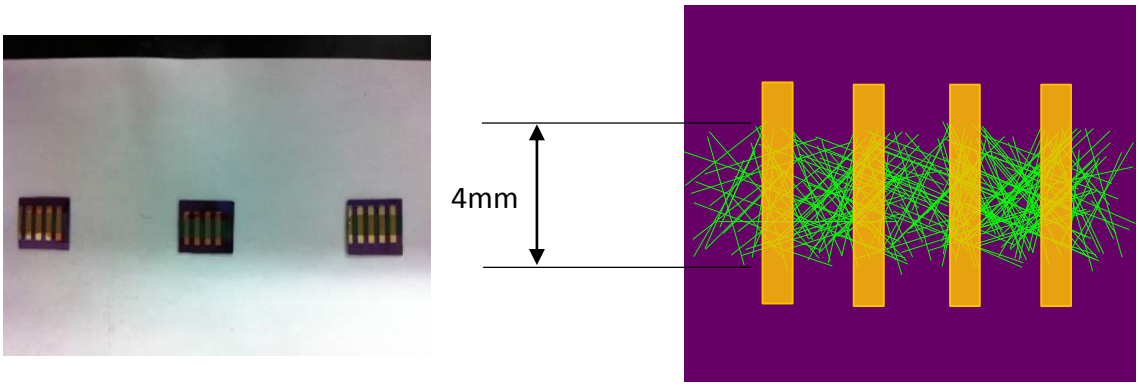

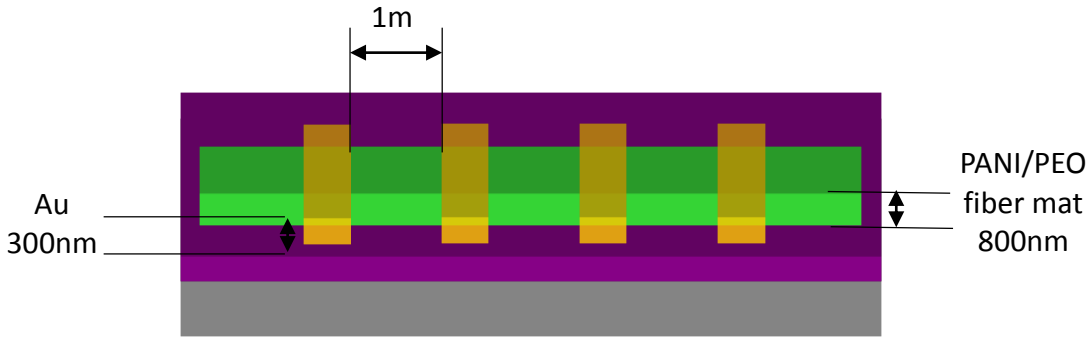

Figure 3.12 Fabrication of PANI/PEO fiber mats contact

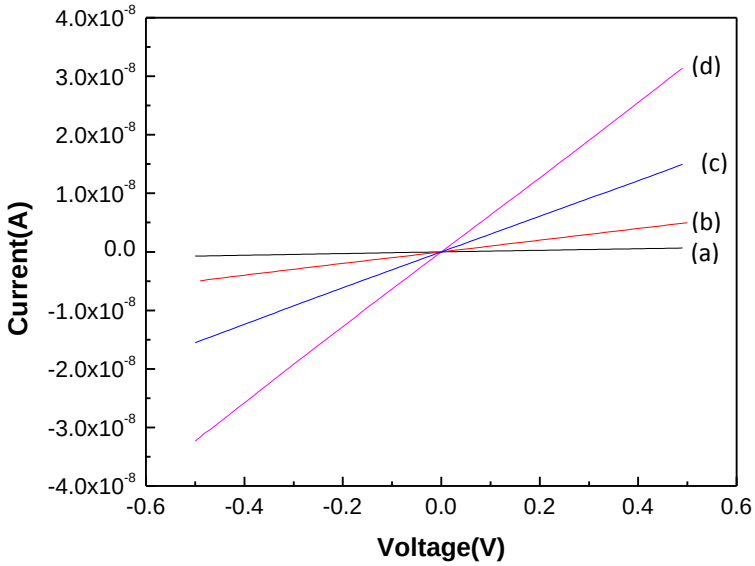

Figure 3.13 I-V curves of PANI/PEO fiber mats with 800nm thickness. PANI content (wt.%): (a)12 (b)26 (c)45 (d)52

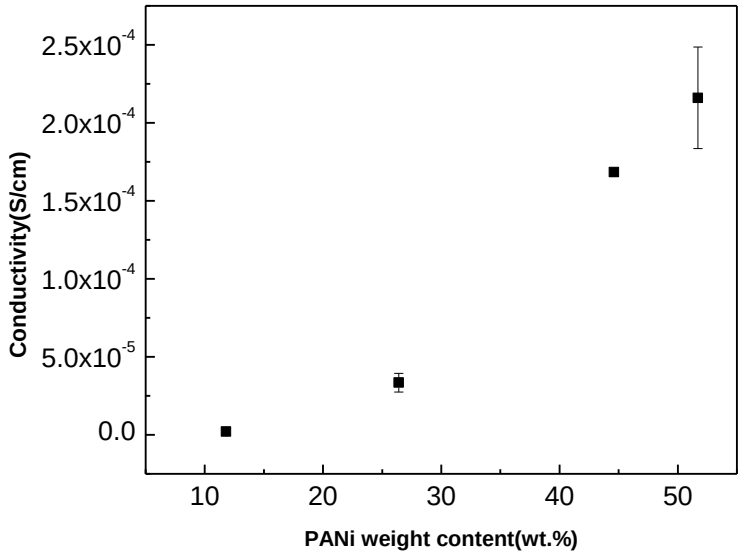

Figure 3.14 Electrical conductivity of the HCSA doped PANI and PEO blend electrospun nanofibers

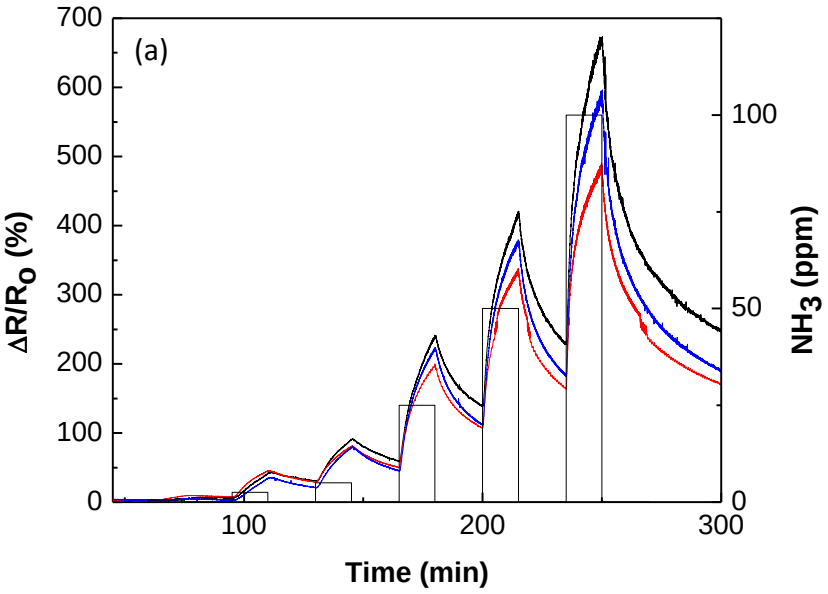
(a)
700
600
500
400
300
200
100
0
100
200
300
Time (min)
ΔR/R0 (%)
100
50
0
NH3 (ppm)

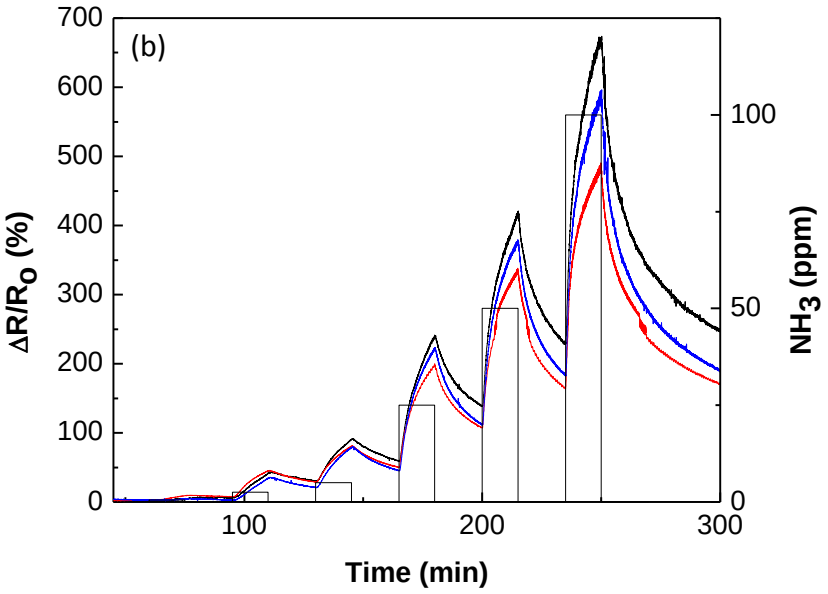
(b)
700
600
500
400
300
200
100
0
100
200
300
Time (min)
ΔR/R0 (%)
100
50
0
NH3 (ppm)

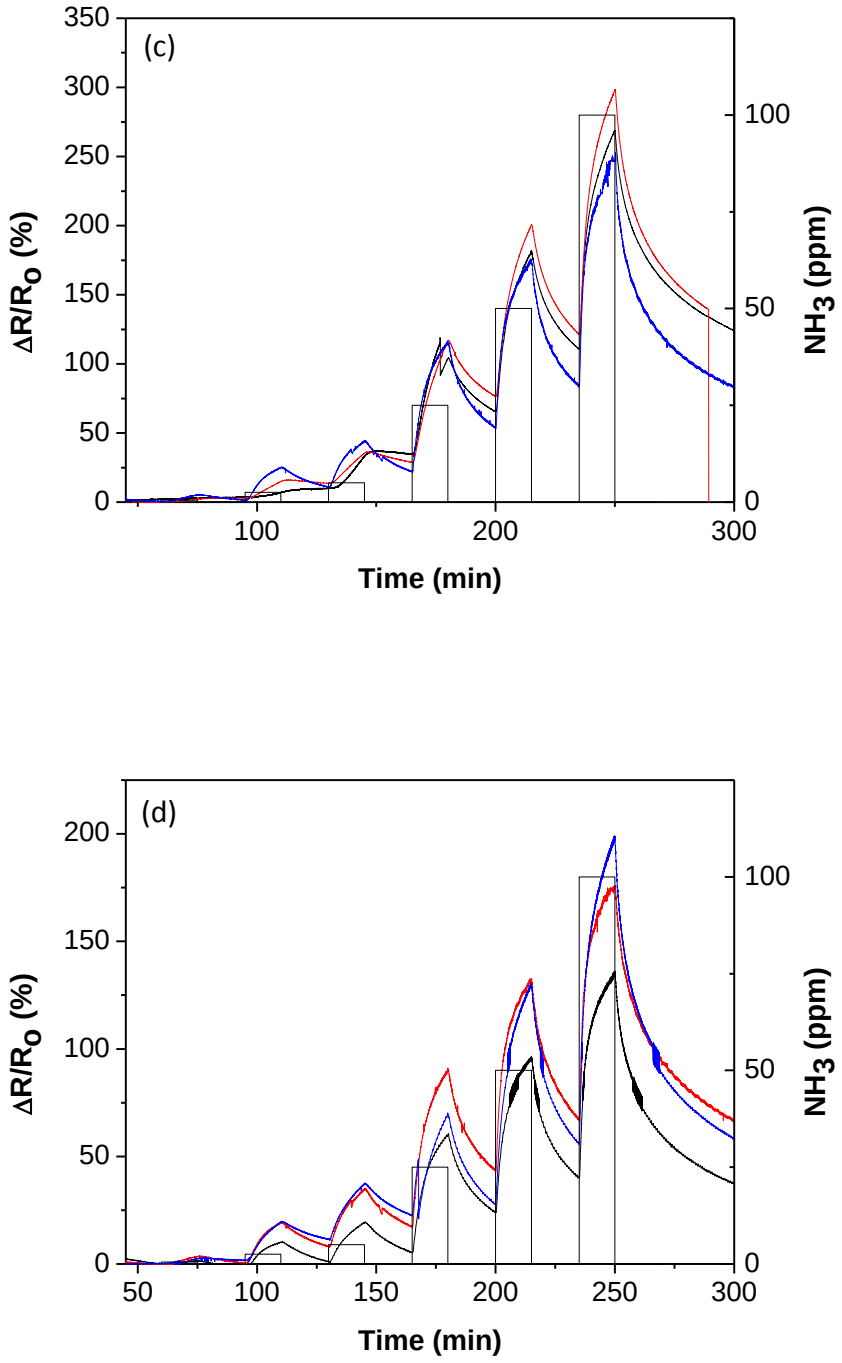

Figure 3.15 Real-time response of different composition of PANI/PEO nanofibers to different concentrations of NH_3. PANI content (wt.%): (a)12 (b)26 (c)45 (d)52

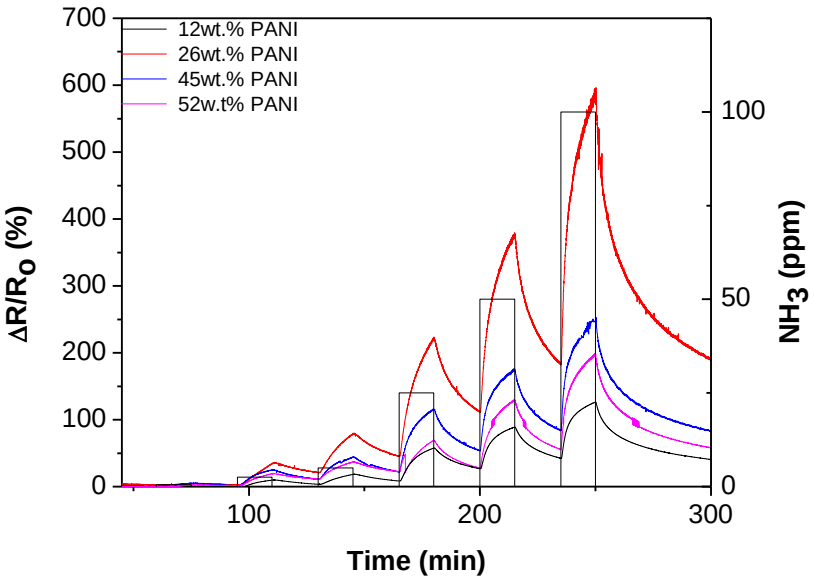

Figure 3.16 Real-time response of different composition of PANI/PEO nanofibers to different concentrations of NH_3

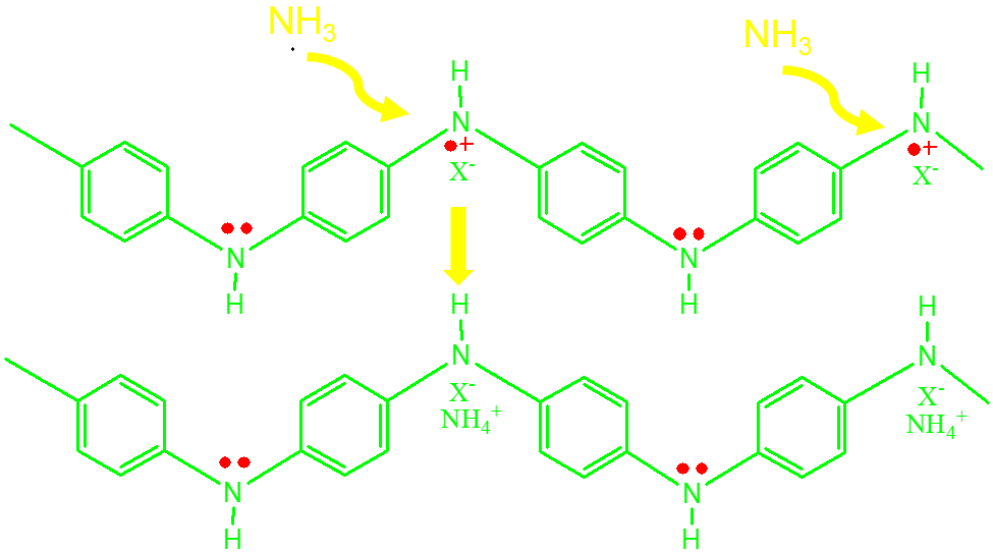

Figure 3.17 Sensing Mechanism of HCSA doped Polyaniline to NH_3

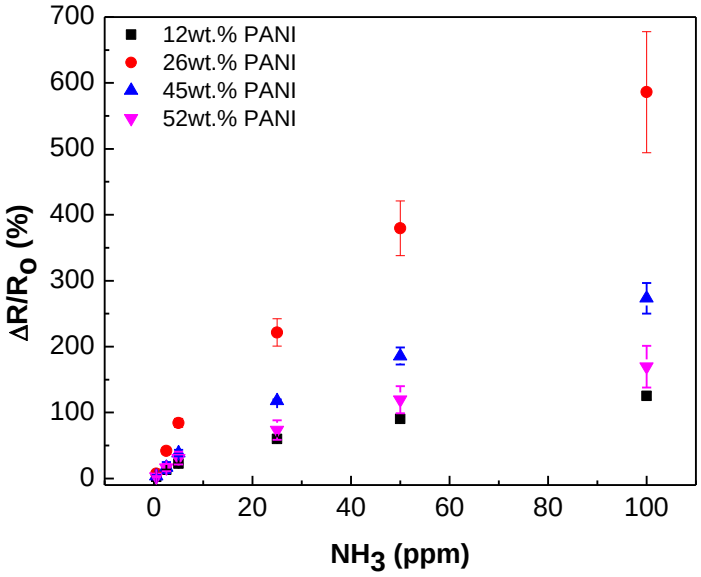

Figure 3.18 Calibration Curve of sensitivity of different composition of PANI/PEO nanofibers exposed to NH_3

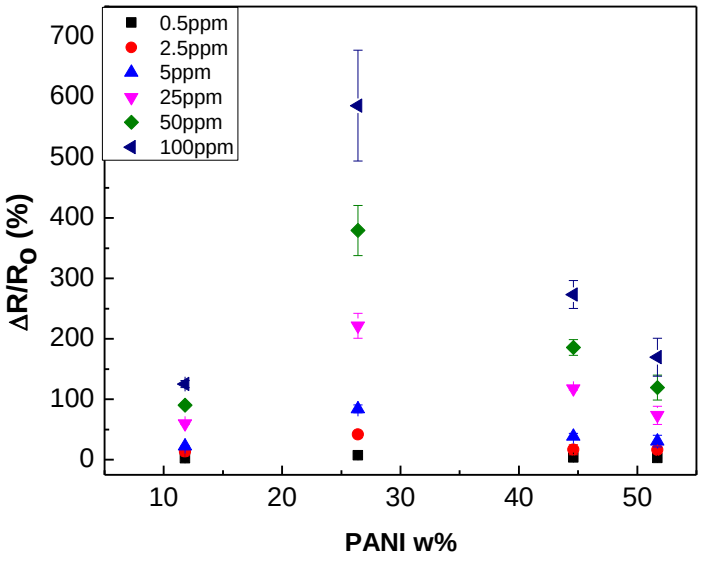

Figure 3.19 PANI Content effect on NH3 sensing sensitivity

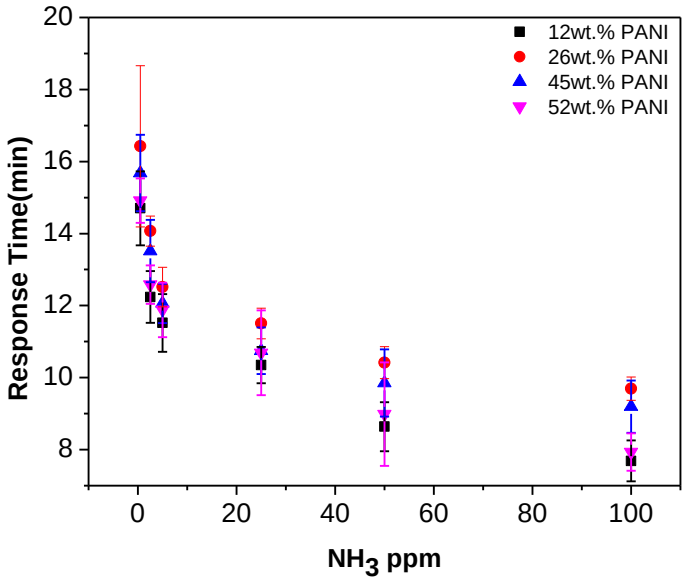

Figure 3.20 Calibration curve of response time to different concentrations of NH_3

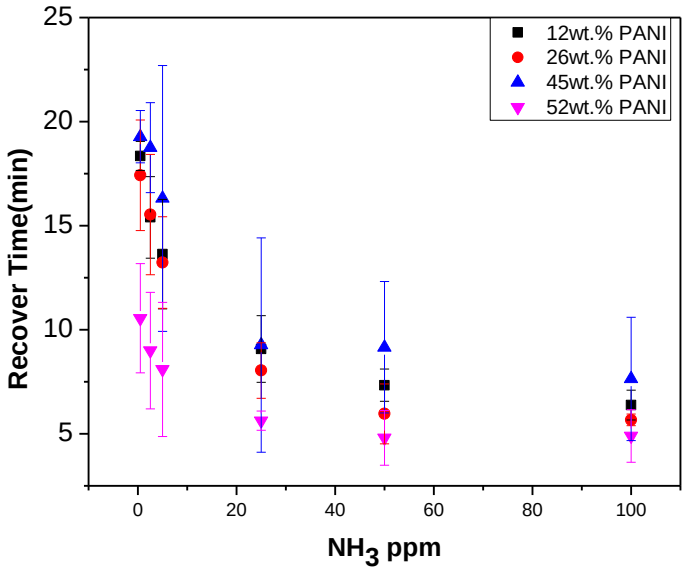

Figure 3.21 Calibration curve of recovery time to different concentrations of NH_3

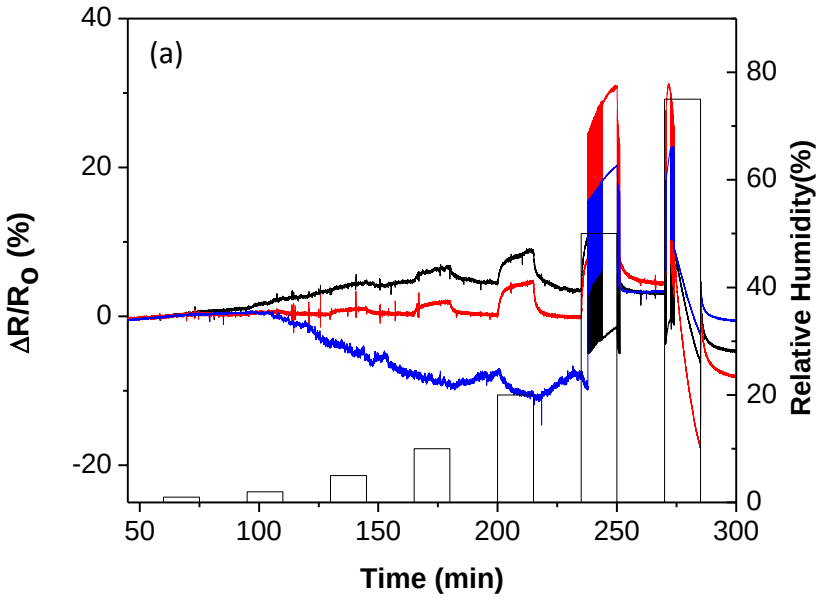
(a)
40
20
0
-20
80
60
40
20
0
50
100
150
200
250
300
ΔR/R_O (%)
Relative Humidity(%)
Time (min)

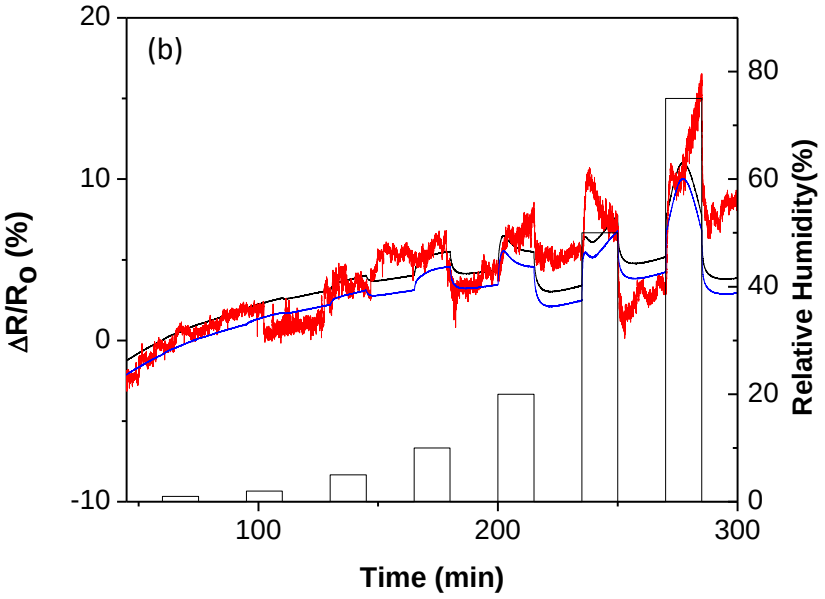
(b)
20
10
0
-10
80
60
40
20
0
100
200
300
ΔR/R_O (%)
Relative Humidity(%)
Time (min)

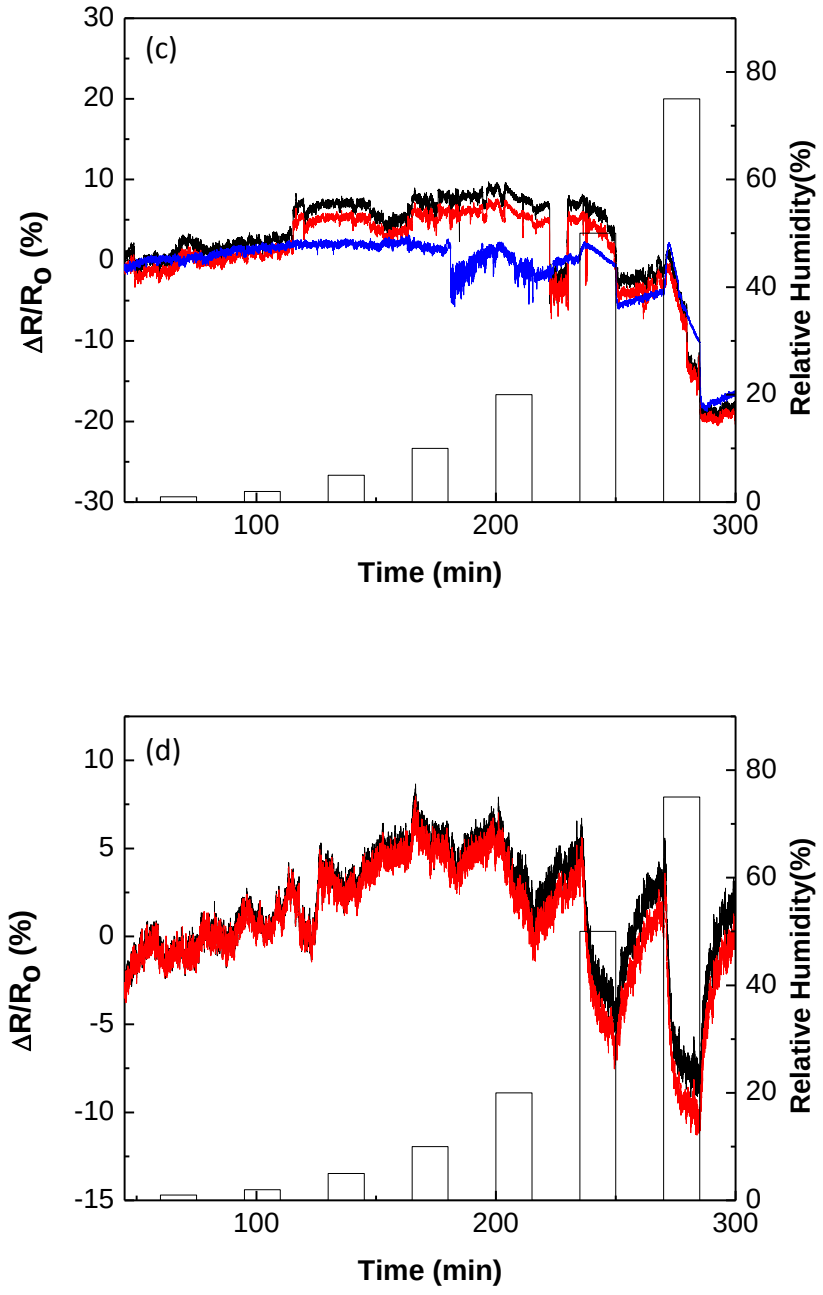

Figure 3.22 Real-time response of different composition of PANI/PEO nanofibers to different concentrations of NH_3. PANI content (wt.%): (a)12 (b)26 (c)45 (d)52

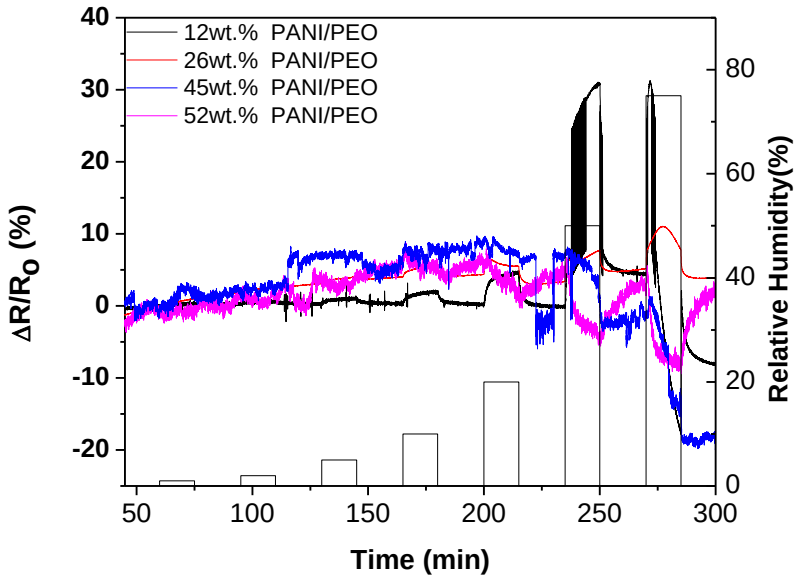

Figure 3.23 Real-time response of different composition of PANI/PEO nanofibers to different concentrations of NH_3

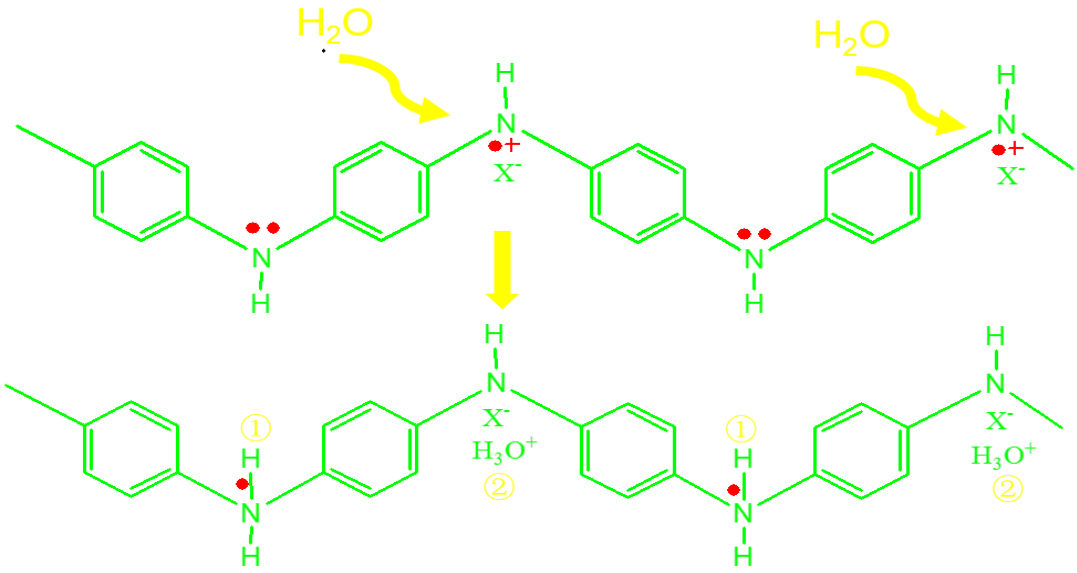

Figure 3.24 Sensing mechanism of HCSA doped polyaniline to water

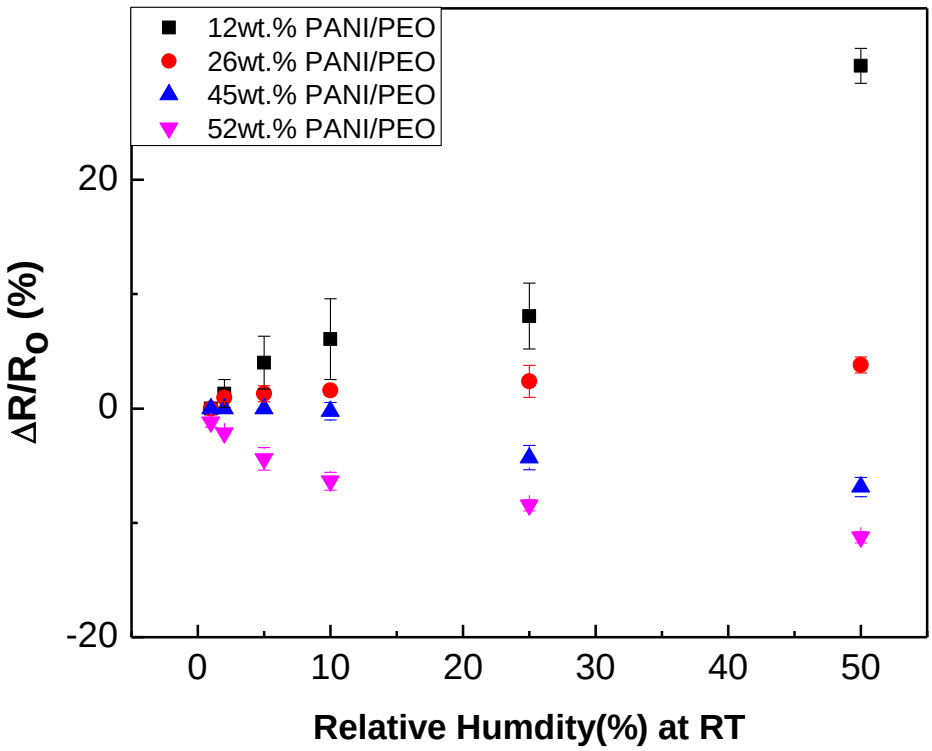

Figure 3.25 Calibration Curve of sensitivity of different humidity degrees

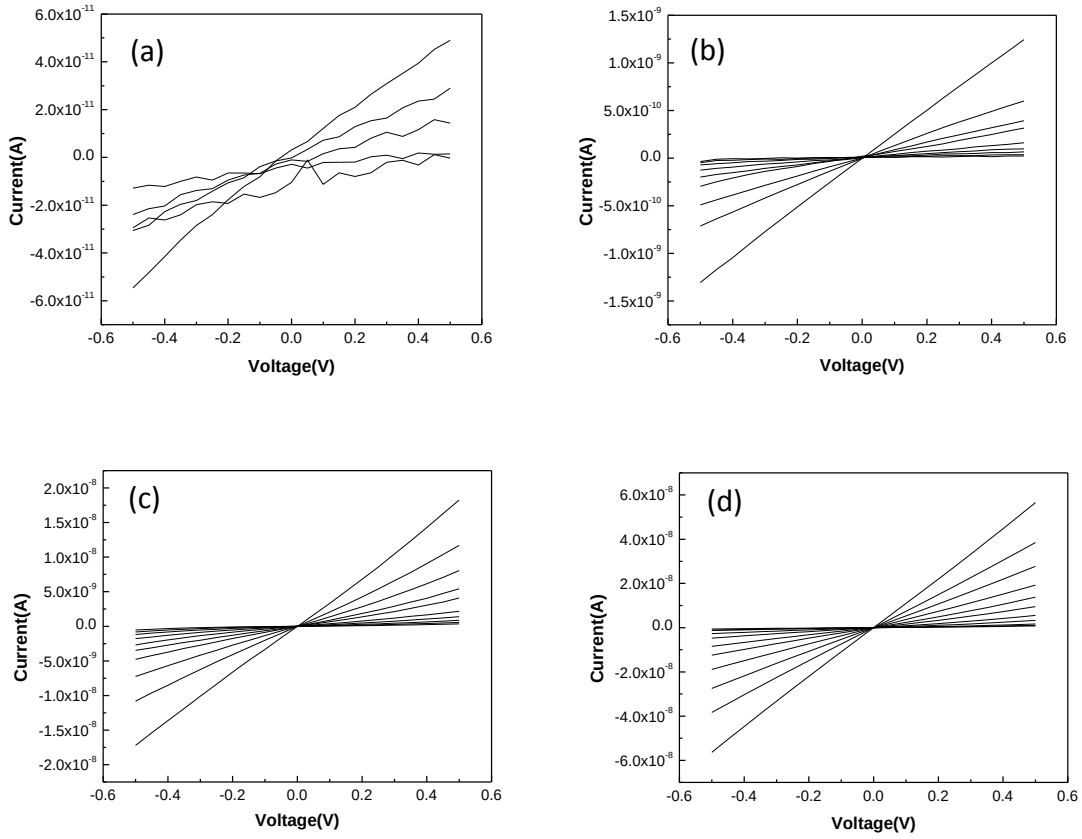

Figure 3.26 I-V characteristics of PANI/PEO nanofiber with various temperatures. PANI content (wt.%): (a)12 (b)26 (c)45 (d)52

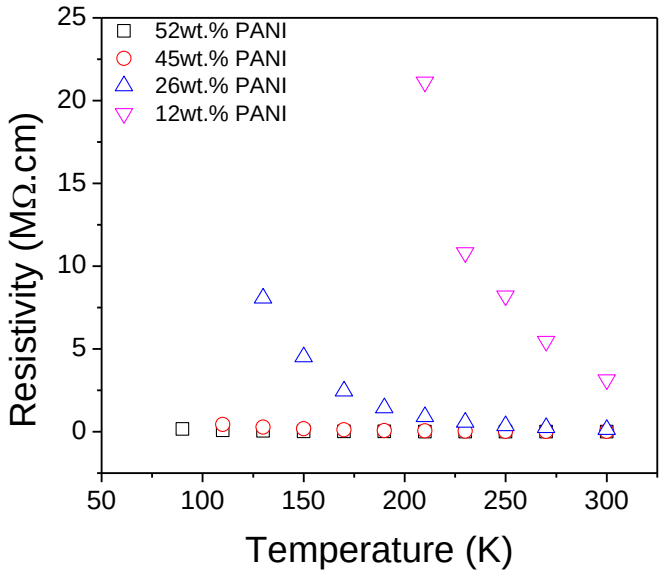

Figure 3.27 Resistivity at various temperature

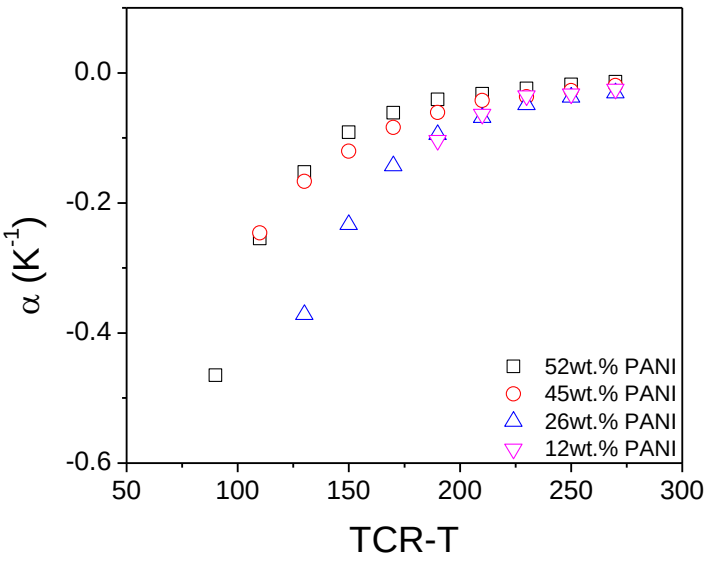

Figure 3.28 Temperature coefficient of resistance for different compositions of PANI/PEO nanofibers

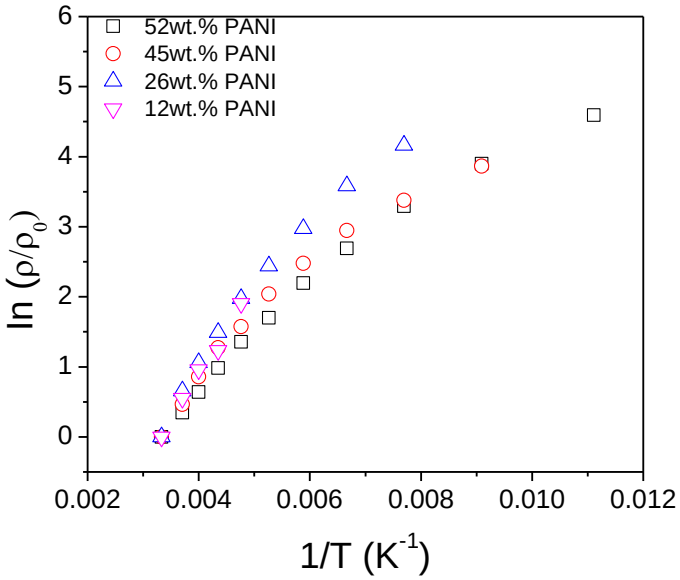

Figure 3.29 Arrhenius plot for different compositions of PANI/PEO nanofibers

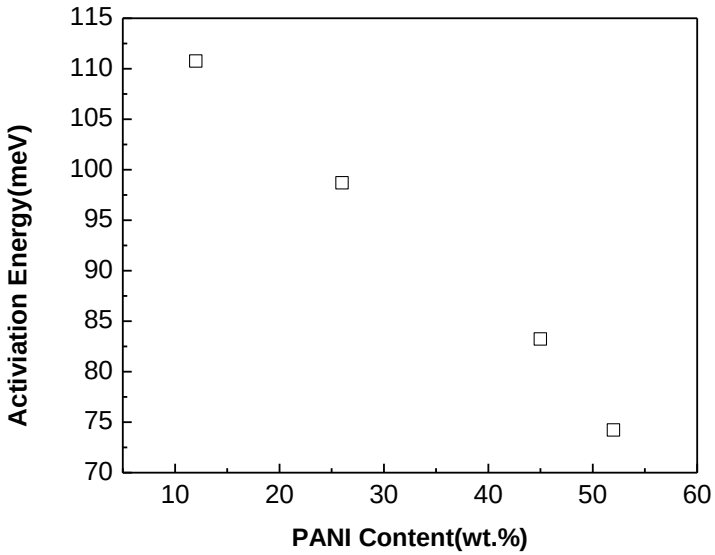

Figure 3.30 Activation energy for different compositions of PANI/PEO nanofibers

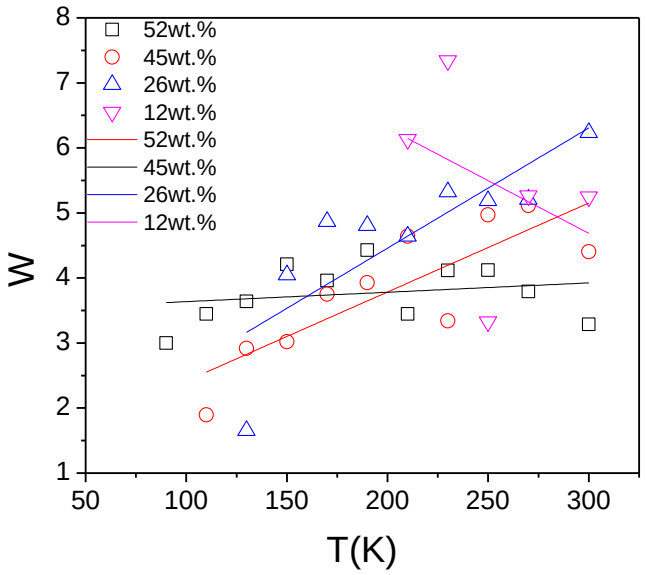

Figure 3.31 Reduced activation energy for different compositions of PANI/PEO nanofibers

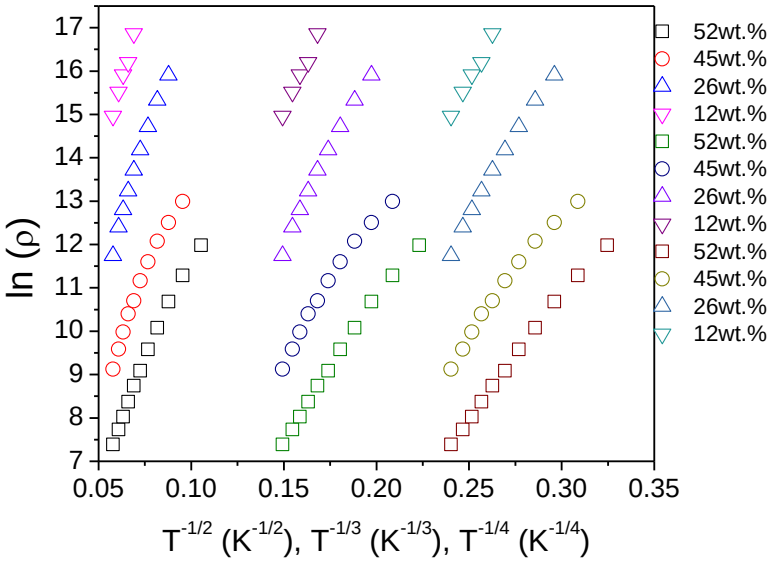

Figure 3.32 Plot of ln(ρ) as function of $T^{1/2}$, $T^{1/3}$, $T^{1/4}$

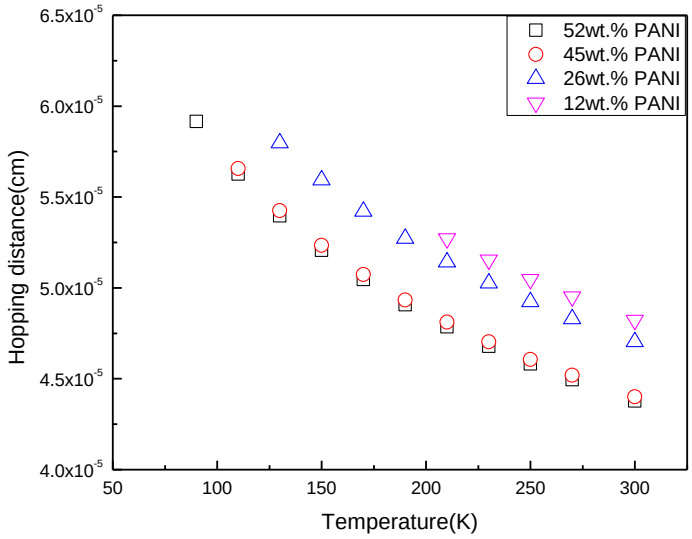

Figure 3.33 Average hopping distance for different compositions of PANI/PEO nanofibers

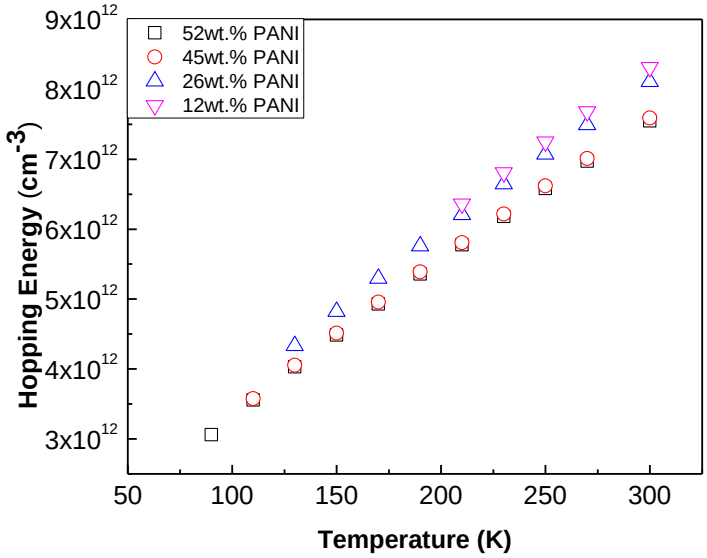

Figure 3.34 Average hopping energy for different compositions of PANI/PEO nanofibers

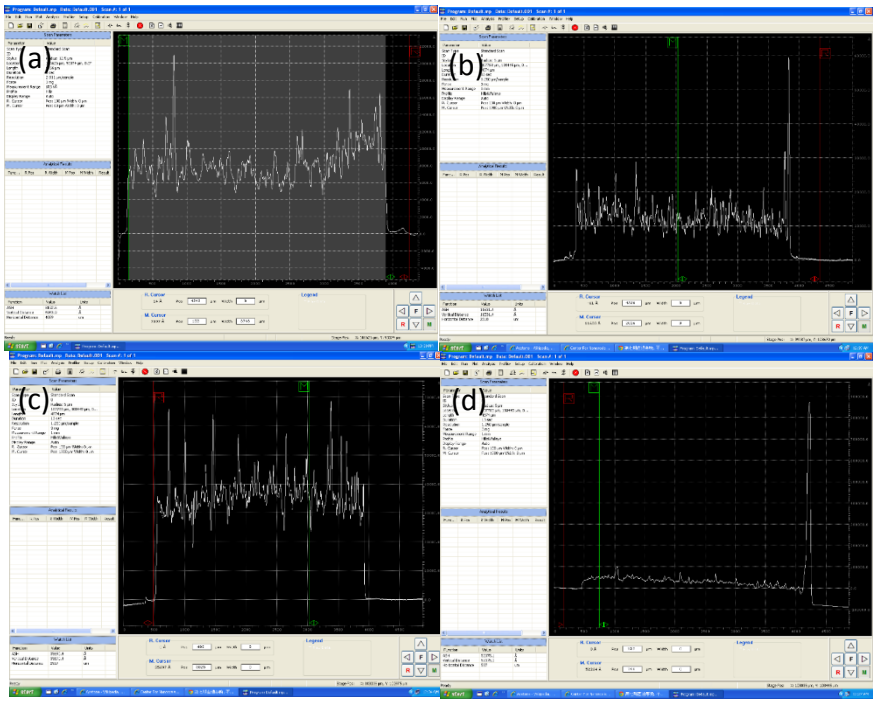

Figure 3.35 Dectak images of 52wt.% PANI/PEO nanofibers with different thickness (a)0.82μm (b)1.15μm (c)3.57μm (d)5.24μm

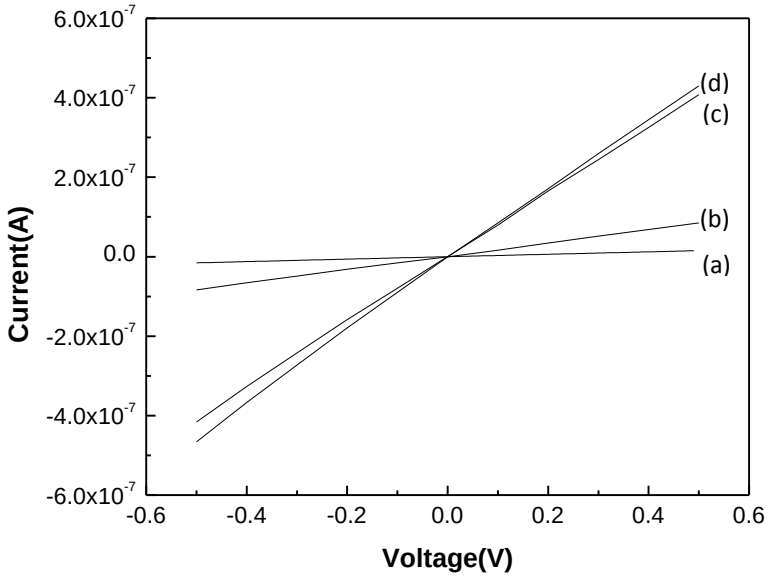

Figure 3.36 I-V curve of 52wt.% PANI/PEO nanofibers with different thickness(a)0.82μm (b)1.15μm (c)3.57μm (d)5.24μm

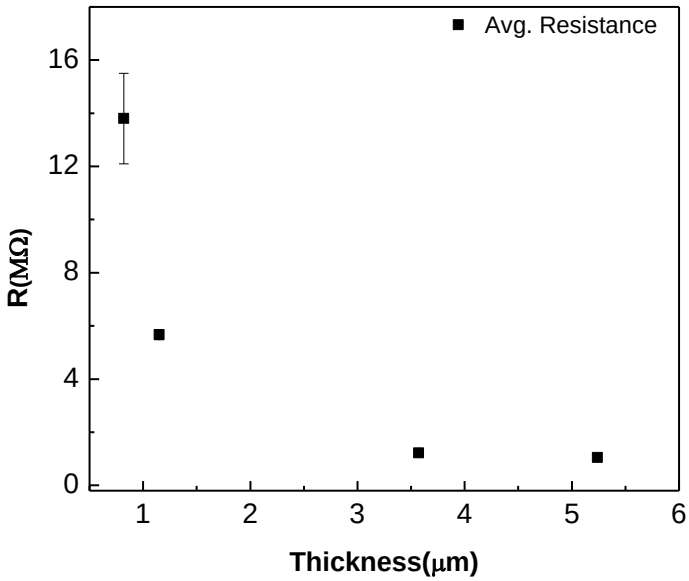

Figure 3.37 Resistance of 52wt.% PANI/PEO fiber mats with different thickness

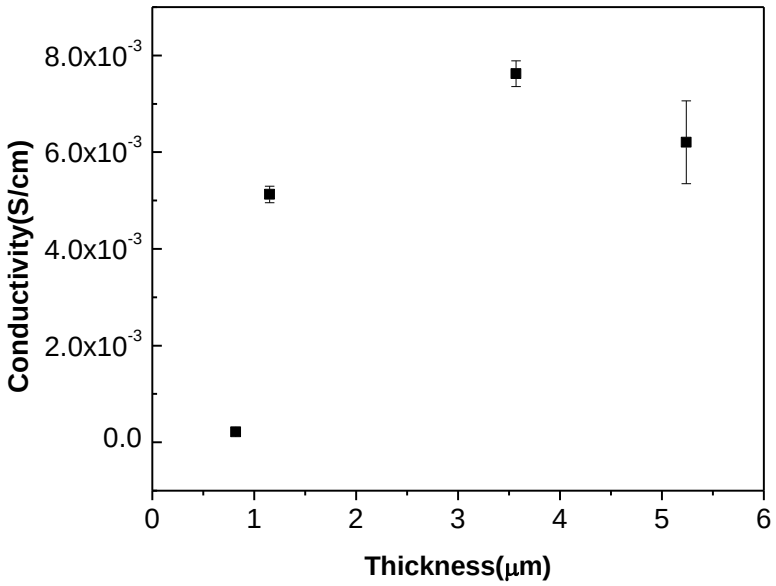

Figure 3.38 Electric conductivity of 52wt.% PANI/PEO fiber mats with different thickness

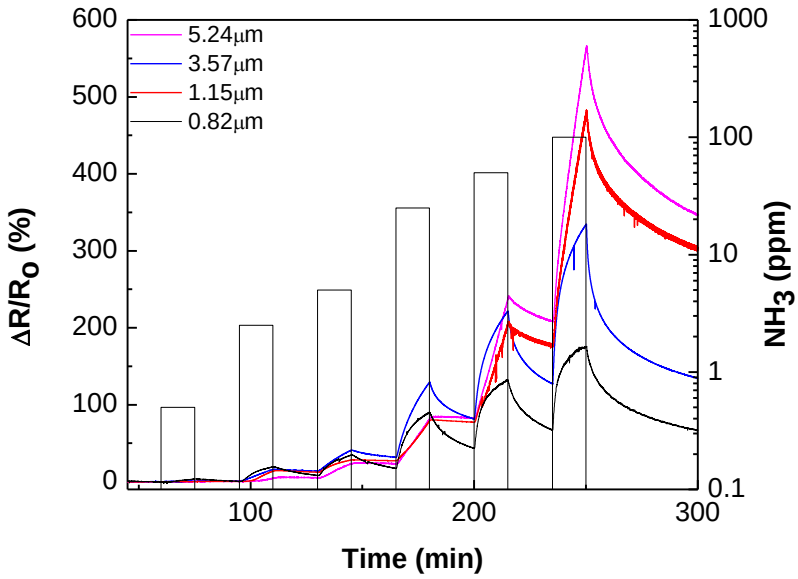

Figure 3.39 Real-time response of different thickness of 52wt.% PANI/PEO nanofibers to different concentrations of NH_3

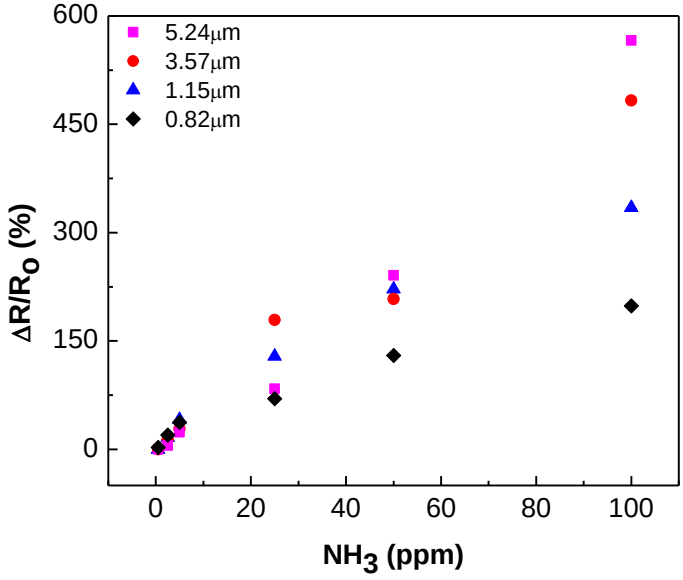

Figure 3.40 Calibration curve of different NH_3 concentrations of 52wt.% PANI/PEO nanofibers with different thickness

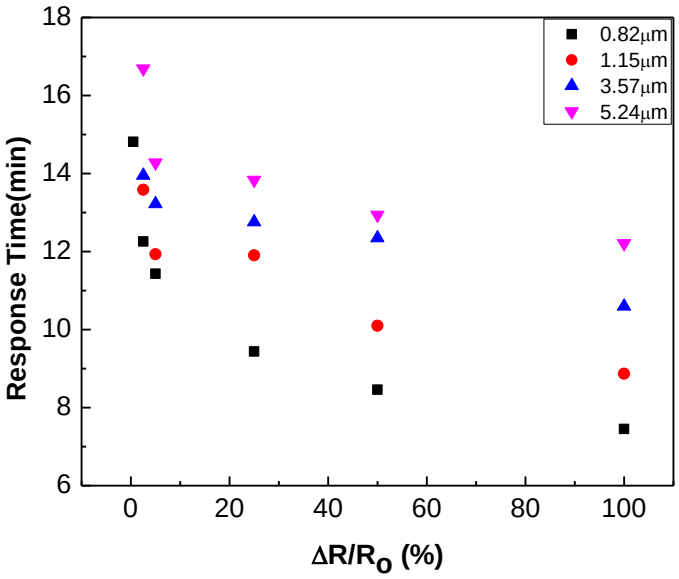

Figure 3.41 Calibration curve of response time of different composition of PANI/PEO nanofibers exposed to NH_3

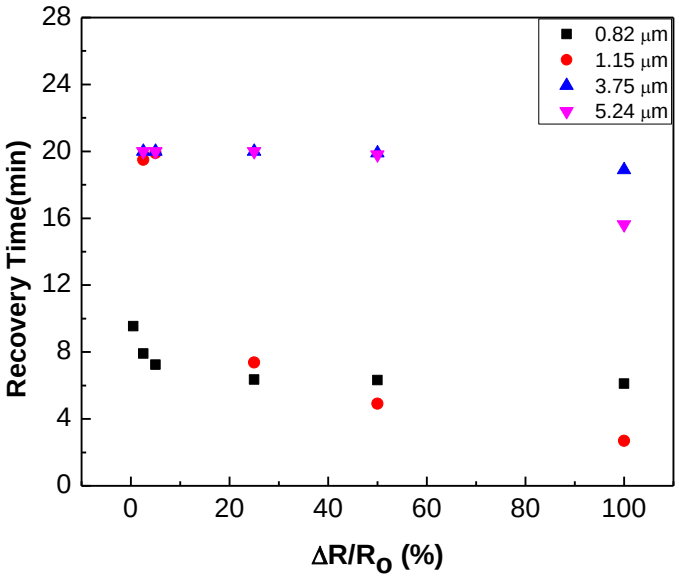

Figure 3.42 Calibration curve of recovery time of different composition of PANI/PEO nanofibers exposed to NH_3

References

1. Kong, J., et al., Nanotube Molecular Wires as Chemical Sensors. Science, 2000. **287**(5453): p. 622-625.
2. Göpel, W. and K.D. Schierbaum, SnO2 sensors: current status and future prospects. Sensors and Actuators B: Chemical, 1995. **26**(1–3): p. 1-12.
3. Göpel, W., Supramolecular and polymeric structures for gas sensors. Sensors and Actuators B: Chemical, 1995. **24**(1–3): p. 17-32.
4. Lee, D.-S., et al., Nitrogen oxides-sensing characteristics of WO3-based nanocrystalline thick film gas sensor. Sensors and Actuators B: Chemical, 1999. **60**(1): p. 57-63.
5. Darrell, H.R. and C. Iksoo, Nanometre diameter fibres of polymer, produced by electrospinning. Nanotechnology, 1996. **7**(3): p. 216.
6. Doshi, J. and D.H. Reneker, Electrospinning process and applications of electrospun fibers. Journal of Electrostatics, 1995. **35**(2–3): p. 151-160.
7. Fong, H., I. Chun, and D.H. Reneker, Beaded nanofibers formed during electrospinning. Polymer, 1999. **40**(16): p. 4585-4592.
8. Frenot, A. and I.S. Chronakis, Polymer nanofibers assembled by electrospinning. Current Opinion in Colloid & Interface Science, 2003. **8**(1): p. 64-75.
9. Sundaray, B., A. Choi, and Y.W. Park, Highly conducting electrospun polyaniline-polyethylene oxide nanofibrous membranes filled with single-walled carbon nanotubes. Synthetic Metals, 2010. **160**(9–10): p. 984-988.
10. Ji, S., Y. Li, and M. Yang, Gas sensing properties of a composite composed of electrospun poly(methyl methacrylate) nanofibers and in situ polymerized polyaniline. Sensors and Actuators B: Chemical, 2008. **133**(2): p. 644-649.
11. Ding, B., et al., Gas Sensors Based on Electrospun Nanofibers. Sensors, 2009. **9**(3): p. 1609-1624.
12. Lijuan, Z. and W. Meixiang, Synthesis and characterization of self-assembled polyaniline nanotubes doped with D-10-camphorsulfonic acid. Nanotechnology, 2002. **13**(6): p. 750.
13. Jang, W.H., et al., Synthesis and electrorheology of camphorsulfonic acid doped polyaniline suspensions. Colloid and Polymer Science, 2001. **279**(8): p. 823-827.
14. Raut, B.T., et al., CSA doped polyaniline/CdS organic–inorganic nanohybrid: Physical and gas sensing properties. Ceramics International, 2012. **38**(7): p. 5501-5506.
15. Arenas, C. and G. Sánchez, Optical, electrical and morphological properties of transparent binary doped polyaniline thin films synthesized by in situ chemical bath deposition. Polymer International, 2011. **60**(7): p. 1123-1128.
16. Safenaz M. Reda, S.M.A.-G., Synthesis and Electrical Properties of Polyaniline Composite with Silver Nanoparticles. Advances in Materials Physics and Chemistry, 2012. **2**(3): p. 75-81.

17. Chartuprayoon, N., et al., Wafer-Scale Fabrication of Single Polypyrrole Nanoribbon-Based Ammonia Sensor. The Journal of Physical Chemistry C, 2010. **114**(25): p. 11103-11108.
18. Li, J., et al., Micromorphology and electrical property of the HCl-doped and DBSA-doped polyanilines. Synthetic Metals, 2004. **142**(1–3): p. 107-111.
19. Campos, M. and B. Braz, Jr., Mechanism of conduction in doped polyaniline. Journal of Physics D: Applied Physics, 1997. **30**(10): p. 1531.
20. Lee, W., et al., Charge transport properties of fully-sulfonated polyaniline. Synthetic Metals, 1997. **84**(1–3): p. 807-808.

Chapter 4(Appendix)

Inkjet Printing PEDOT:PSS using Desktop Inkjet Printer

4.1 Abstract

The fabrication of PEDOT-PSS as functional thin films in electronic devices has been recently investigated. PEDOT-PSS is a conductive polymer with interesting thermal and electrical properties that exhibits good stability under ambient conditions. The advantage of using conductive polymer films as a sensing element is that they are easy to manufacture with low fabrication costs. In this work, we investigated inkjet printing as a method to optimize the fabrication of PEDOT-PSS films. We present our results where we inkjet printed various dilutions of PEDOT-PSS solutions onto a patterned substrate as the sensor element and determined their performance for NH_3 sensing.

4.2 Introduction

Recently, the development of organic elements in electronic devices has been widely studied due to their efficient performance, relatively low material costs and ease of manufacture [1]. Poly(-ethylenedioxythiophene) : poly(styrenesulfonate) (PEDOT:PSS) is one of the most interesting conductive polymers that has been applied as a sensing material. It possesses high electrical conductivity, excellent stability at ambient environment, and it is easily deposited as a film on substrates PEDOT itself is insoluble in water and hard to process. Polymerization with PSS in water as the electrolyte however can enhance its processability [4]. The electrical conductivity of PEDOT-PSS can be tuned from 1-10 S/cm.

PEDOT-PSS can be printed as a patterned film by various methods, such as gravure, screen printing, inkjet printing, and imprinting. Among these methods, inkjet printing is recognized as one of the more efficient methods to deposit PEDOT-PSS thin films. Inkjet film deposition is essentially a data-driven, mask-less, and non-contacting process with low material costs. The resolution of inkjet printing depends on the smallest dot size that can be printed [5, 6].

4.3 Experimental Details

Our PEDOT-PSS based gas sensors were ink-jet printed onto a 24-individually addressable microelectrode array fabricated photo lithographically on a Si wafer with 3 micron gaps as shown in figure 3.1. The Si wafer was p-type with a 300nm SiO_2 oxidation layer done by e-beaming. The gold electrodes were deposited onto this oxide layer at 20nm and 180nm. Before inkjet printing, however, the wafer was cleaned with oxygen plasma.

Two water dispersions of PEDOT-PSS at 0.13wt% and 1.3w.% concentrations were fed into 1mL cartridges and loaded into a Fujifilm Dimatix DMP 2831 piezoelectric inkjet printer. The Si wafer was put on the working plate, and the spray nozzle was set at 15V at a frequency of 10 kHz. The printer was programmed to evenly deposit samples composed of 1 drop, 5 drops, 10 drops, and 20 drops, respectively onto the microelectrode array.

4.4 Results and Discussion

4.4.1 Material characterization

Optical images of the 0.13wt.% and 1.3wt.% PEDOT-PSS solutions ink printed onto the microelectrodes at different drop numbers (1 drop to 20 drops) are shown in figure 4.2 and figure 4.3. The diameters of the samples became bigger and the color got darker as the drop number increased. The thickness of each sample was measured by dectak as

shown in figure 4.4 and figure 4.5. Since the gap distance was kept constant at 3µm, the sample film thickness increased with increasing drop number. We also want to note that during the printing process solvent evaporation may have caused thicker films. Figure 4.6 shows that film thickness is not a linear function of drop number, and figure 4.7 shows the calculated resistivity of the films ranging between 1 Ω.cm to 16 Ω.cm.

4.4.2 NH_3 Sensing

The microelectrodes printed with PEDOT-PSS sensing material were integrated onto the chip holder by wire bonding and loaded with the sensing system as described in section 2.2.2. Figure 4.8 and figure 4.9 show the sensitivity response of all the above samples when exposed to different concentrations of NH_3 gas. The resistivity increased with NH_3 concentration. When pumping dry air through the chamber to let the sensors recover, we note that their resistance did not return to the baseline (i.e. a hysteresis). Thus, the PEDOT-PSS sensing material has been altered or even destroyed by the NH_3 gas. The sensitivity calibration curves of 1.3wt.% and 0.13wt.% PEDOT-PSS NH_3 sensing are shown in figure 4.10. The 1.3wt% PEDOT-PSS films showed optimal sensing performance at the 5-drop level, while the sensing performance for the 0.13wt.% PEDOT-PSS films showed very little dependence on drop number. Furthermore, the sensitivities of the 1.3wt.% and 0.13wt.% PEDOT-PSS films are compared in figure 4.11. Again, the 5 drop, 1.3wt.% PEDOT film shows the optimal sensing performance.

4.4 Conclusions

We successfully inkjet-printed PEDOT:PSS conductive ink solutions with a resolution gap of 3 microns and film thicknesses ranging from 200 nm to 3 microns on an oxidized Si wafer terminated with gold microelectrodes. We have compared dilution degree of PEDOT-PSS inks and thickness of the jetted films effect on NH_3 sensing performance. It showed that printing 5 drops of a 1.3wt.% PEDOT-PSS solution had the optimal sensitivity to NH_3.

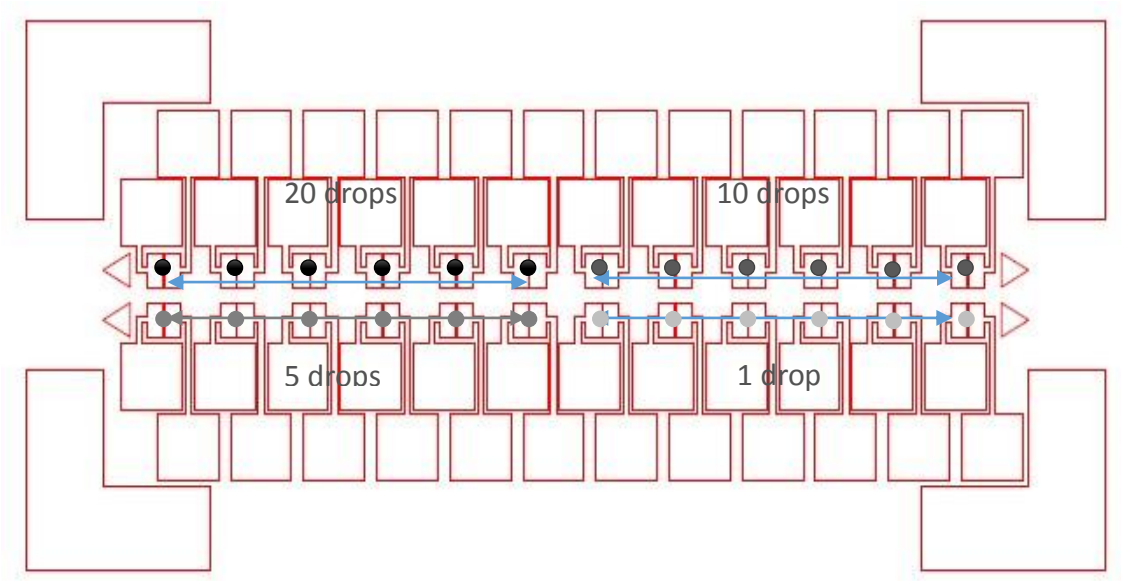

Figure 4.1 Distribution areas of inkjet printing different drops of 1.3wt.% and 0.13wt.% PEDOT-PSS

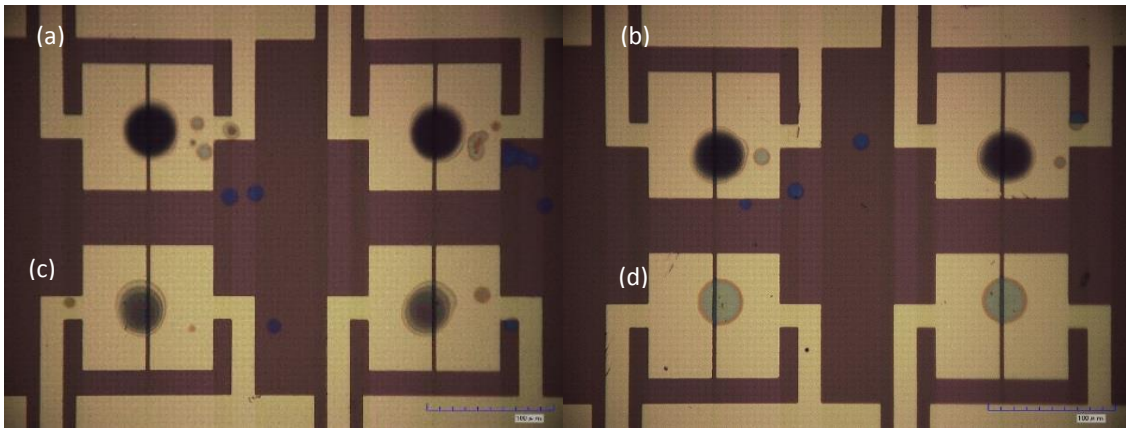

Figure 4.2 Optical images of Ink-jet printing different drops of 1.3wt.% PEODT-PSS (a)20 drops (b)10 drops (c)5 drops (d)1 drop

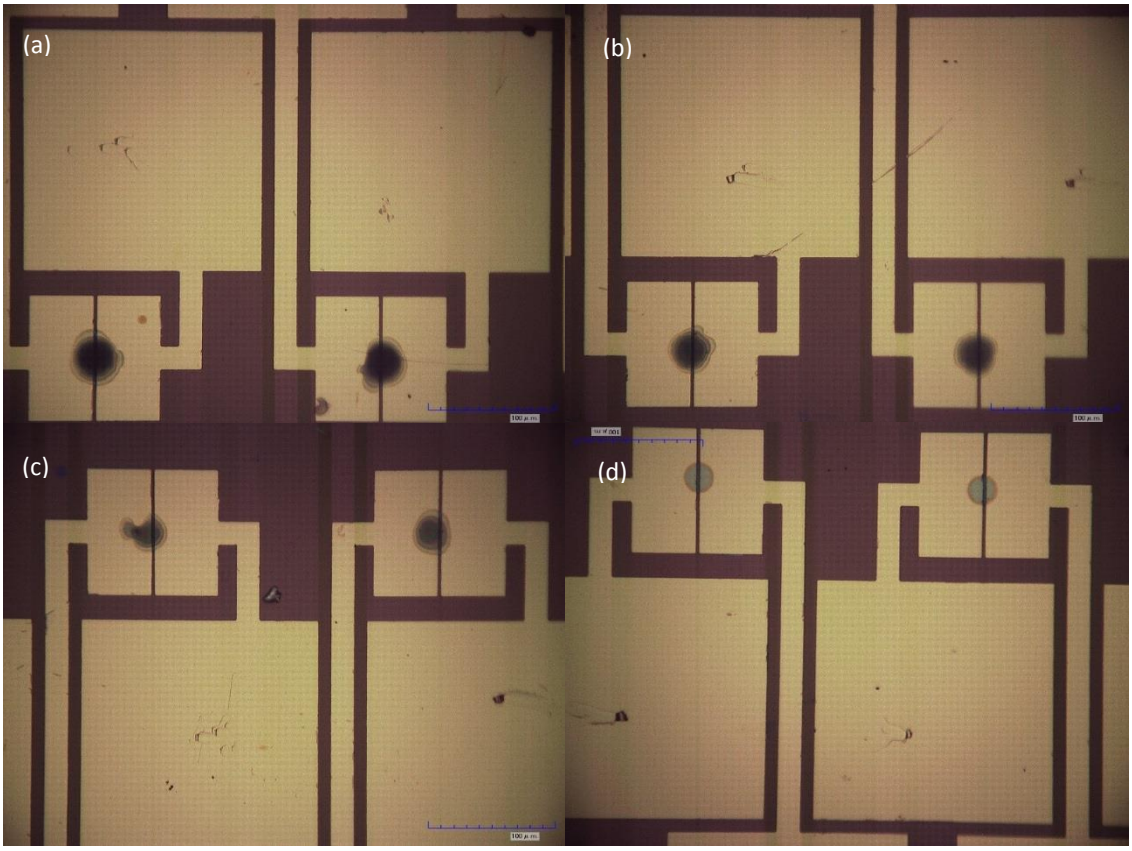

Figure 4.3 Optical images of Ink-jet printing different drops of 1.3wt.% PEODT-PSS (a)20 drops (b)10 drops (c)5 drops (d)1 drop

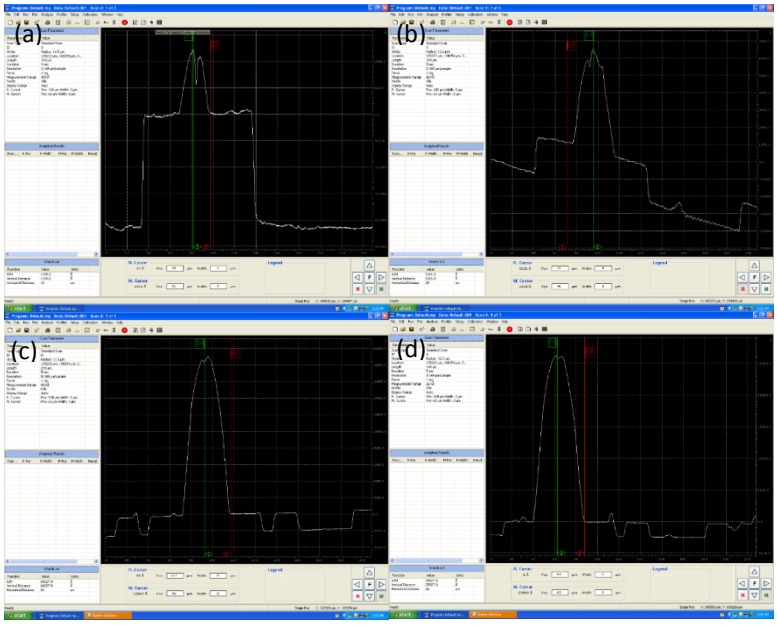

Figure 4.4 Dectak images of ink-jet printing different drops of 1.3wt.% PEDOT-PSS (a)20 drops (b)10 drops (c)5 drops (d)1 drop

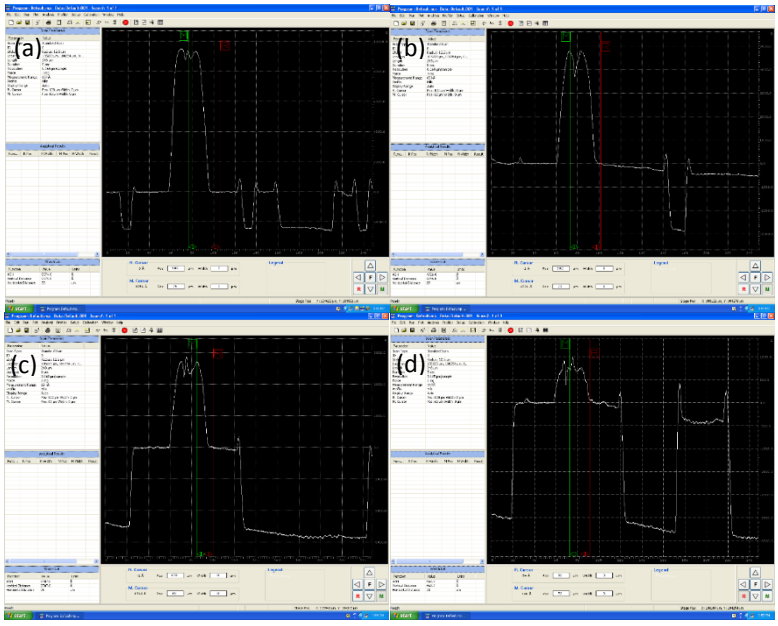

Figure 4.5 Dectak images of ink-jet printing different drops of 0.13wt.% PEDOT-PSS (a)20 drops (b)10 drops (c)5 drops (d)1 drop

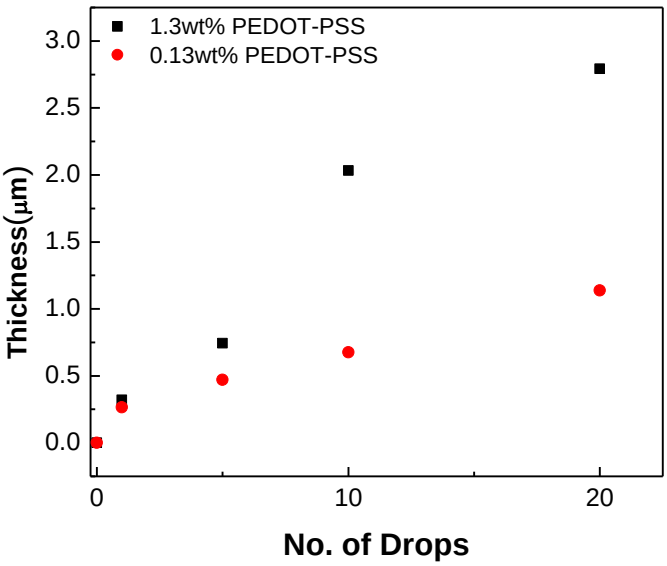

Figure 4.6 Films thickness of ink-jet printing different drops of 1.3wt.% and 0.13wt.% PEDOT-PSS

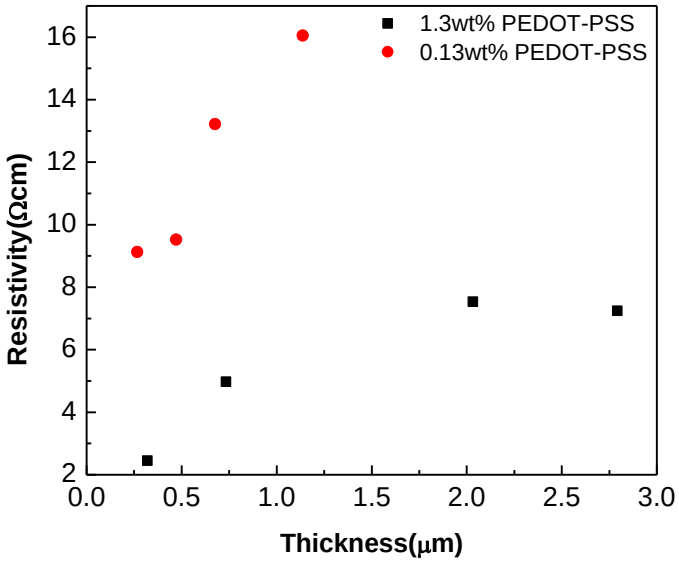

Figure 4.7 Resistivity of ink-jet printing different drops of 1.3wt.% and 0.13wt.% PEDOT-PSS

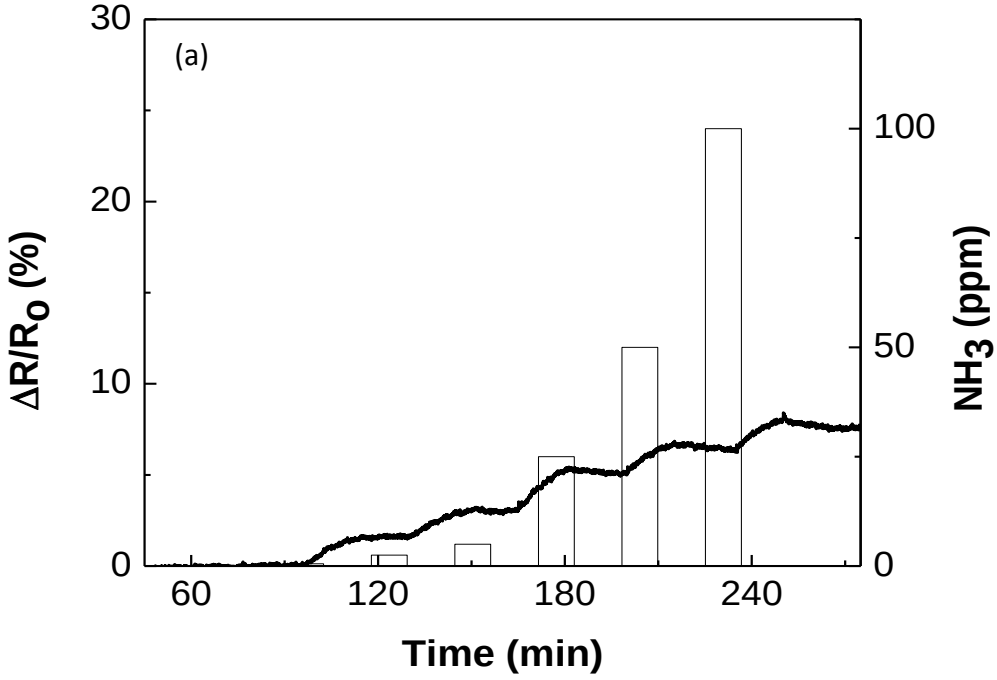
(a)
30
20
10
0
100
50
0
60
120
180
240
Time (min)
ΔR/R0 (%)
NH3 (ppm)

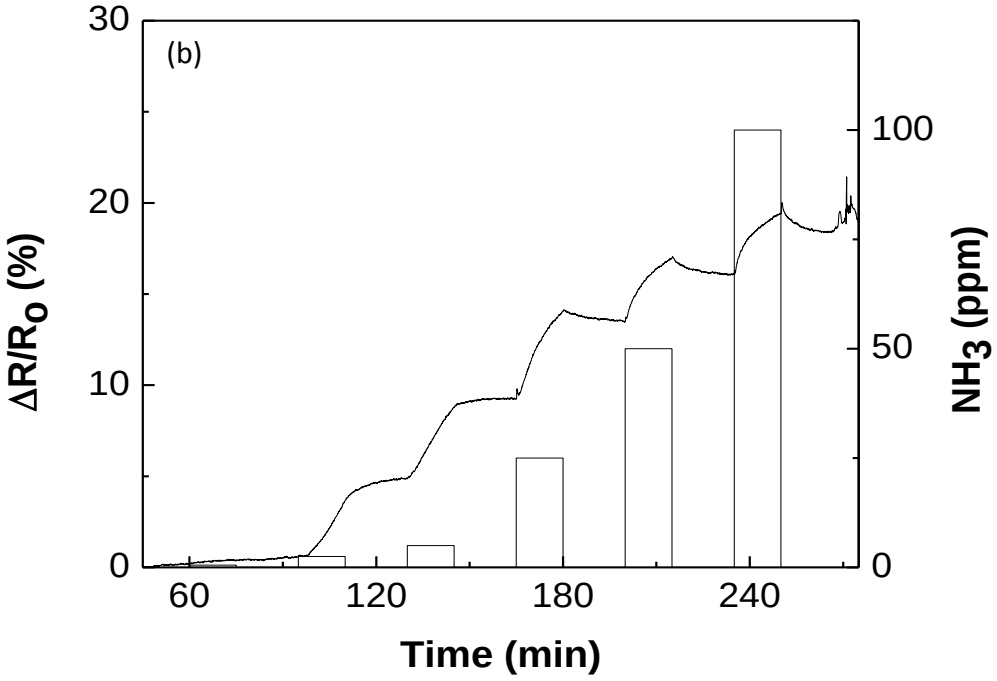
(b)
30
20
10
0
100
50
0
60
120
180
240
Time (min)
ΔR/R0 (%)
NH3 (ppm)

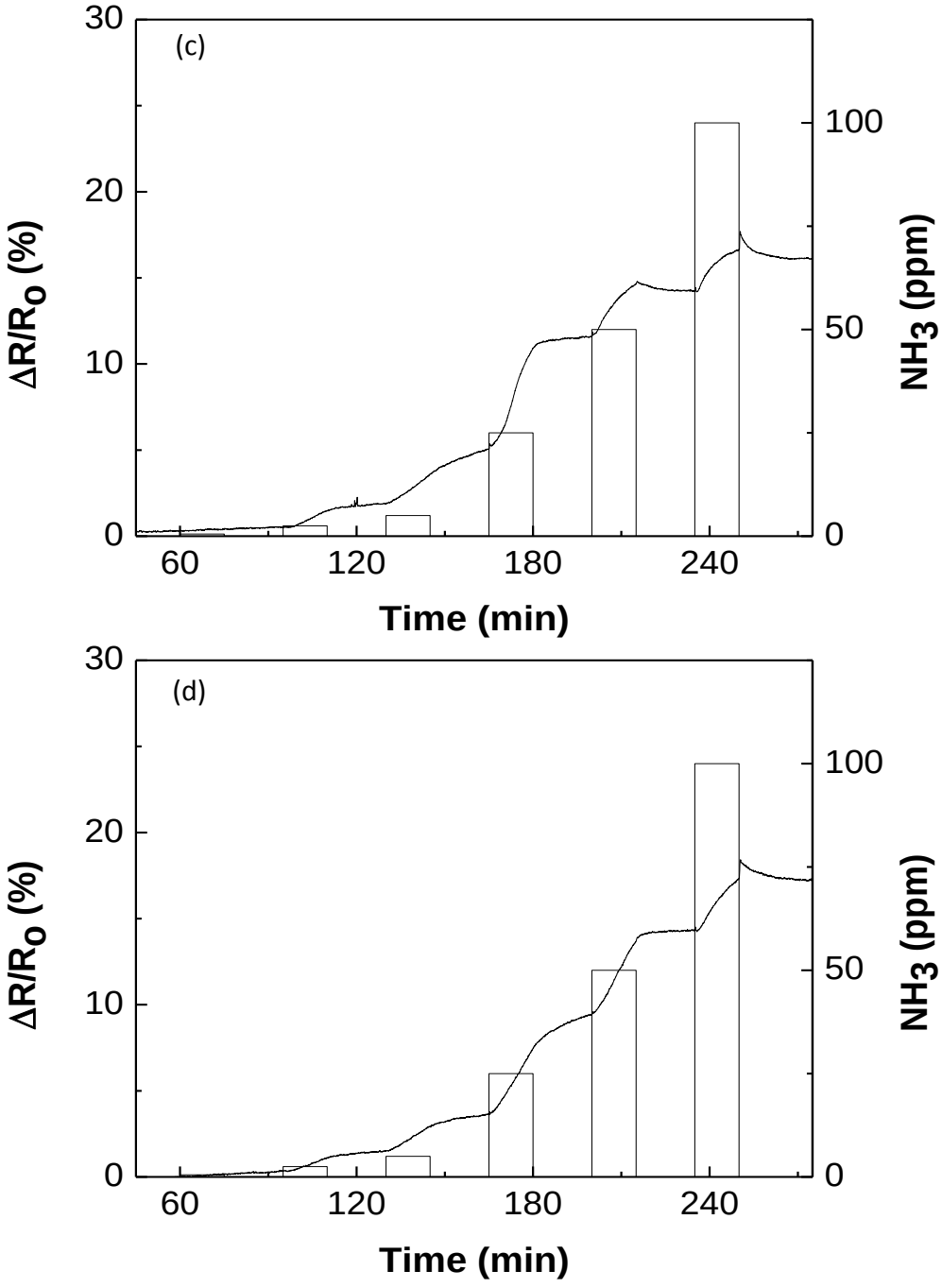

Figure 4.8 Real-time response of ink-jet printing different drops of 1.3wt.% PEDOT-PSS exposed to NH_3 (a)20 drops (b)10 drops (c)5 drops (d)1 drop

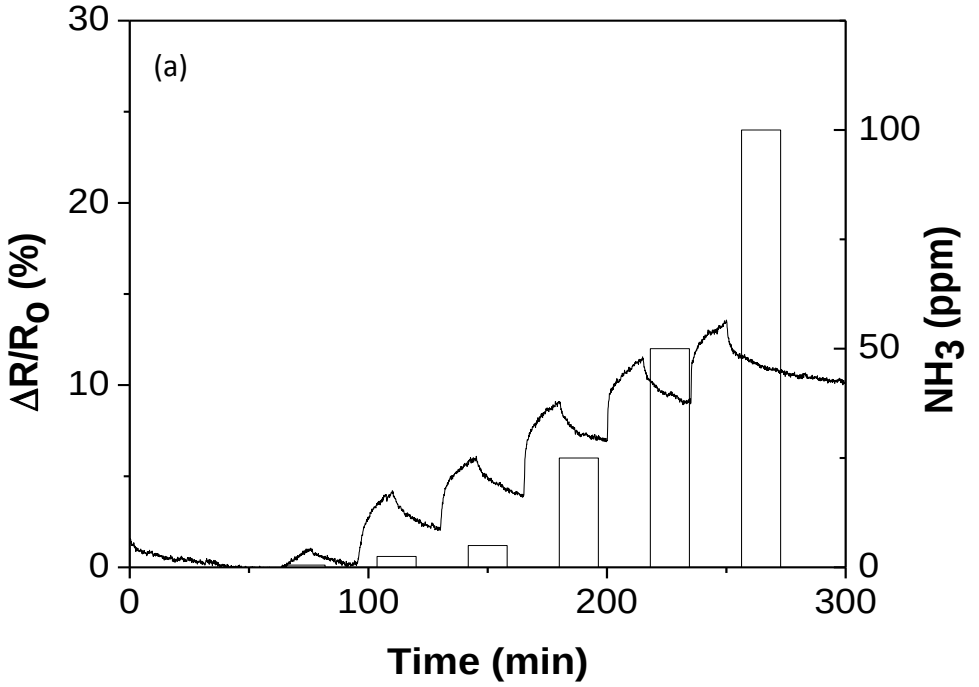
(a)
30
20
10
0
0
100
200
300
100
50
0
ΔR/R$_O$ (%)
NH$_3$ (ppm)
Time (min)

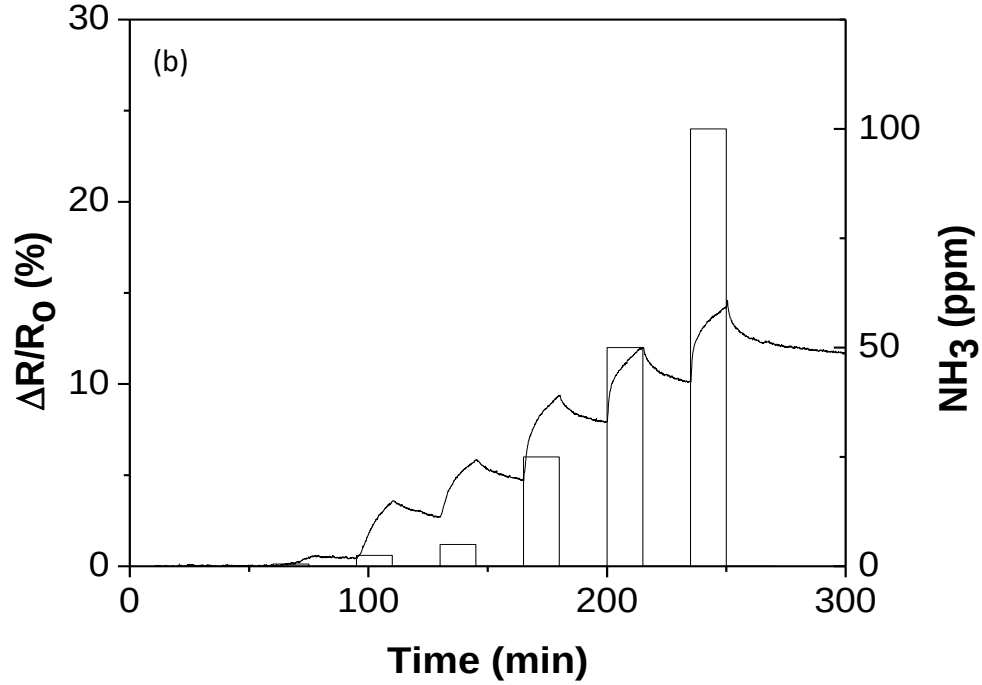
(b)
30
20
10
0
0
100
200
300
100
50
0
ΔR/R$_O$ (%)
NH$_3$ (ppm)
Time (min)

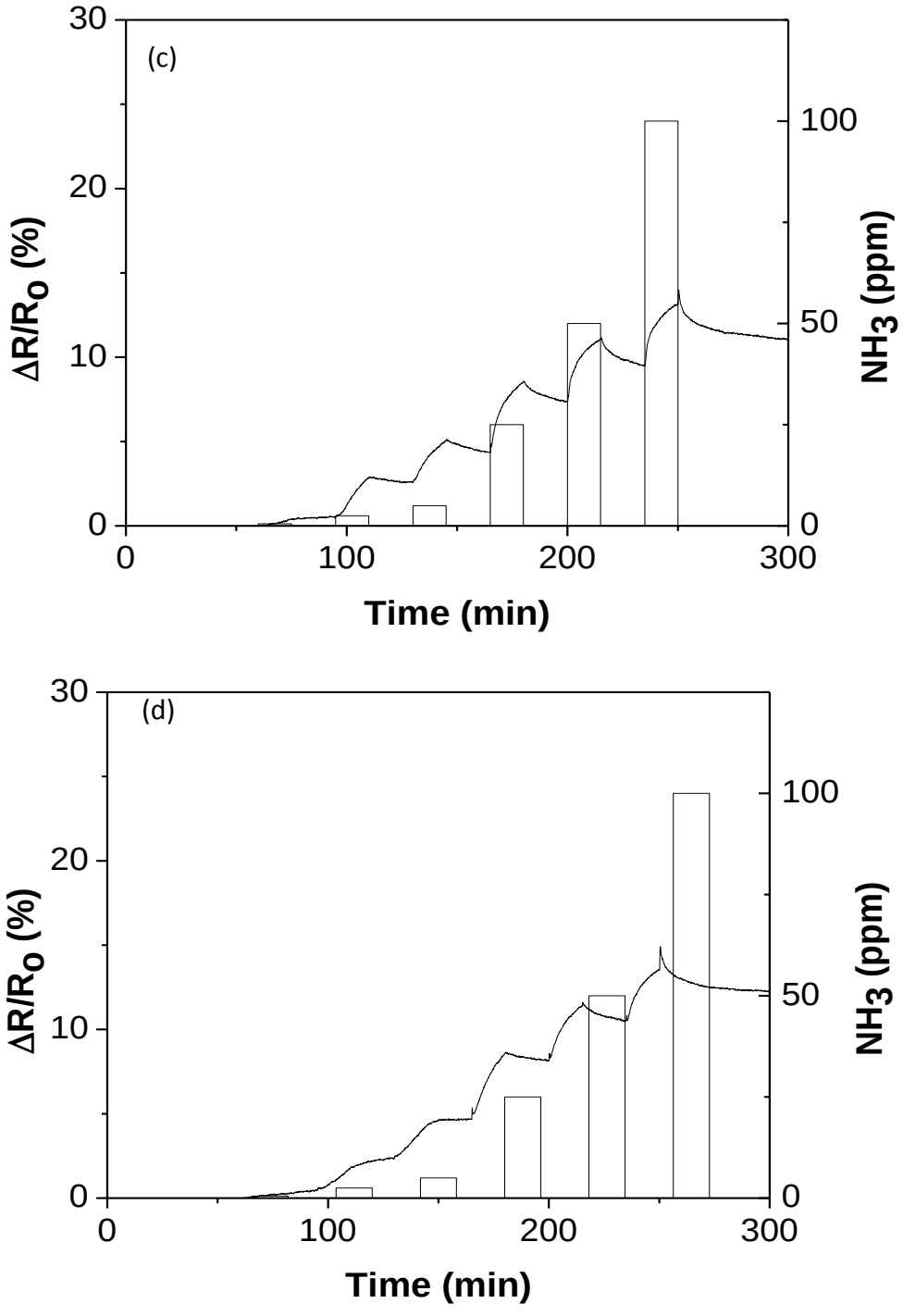

Figure 4.9 Real-time response of ink-jet printing different drops of 0.13wt.% PEDOT-PSS exposed to NH_3 (a)20 drops (b)10 drops (c)5 drops (d)1 drop

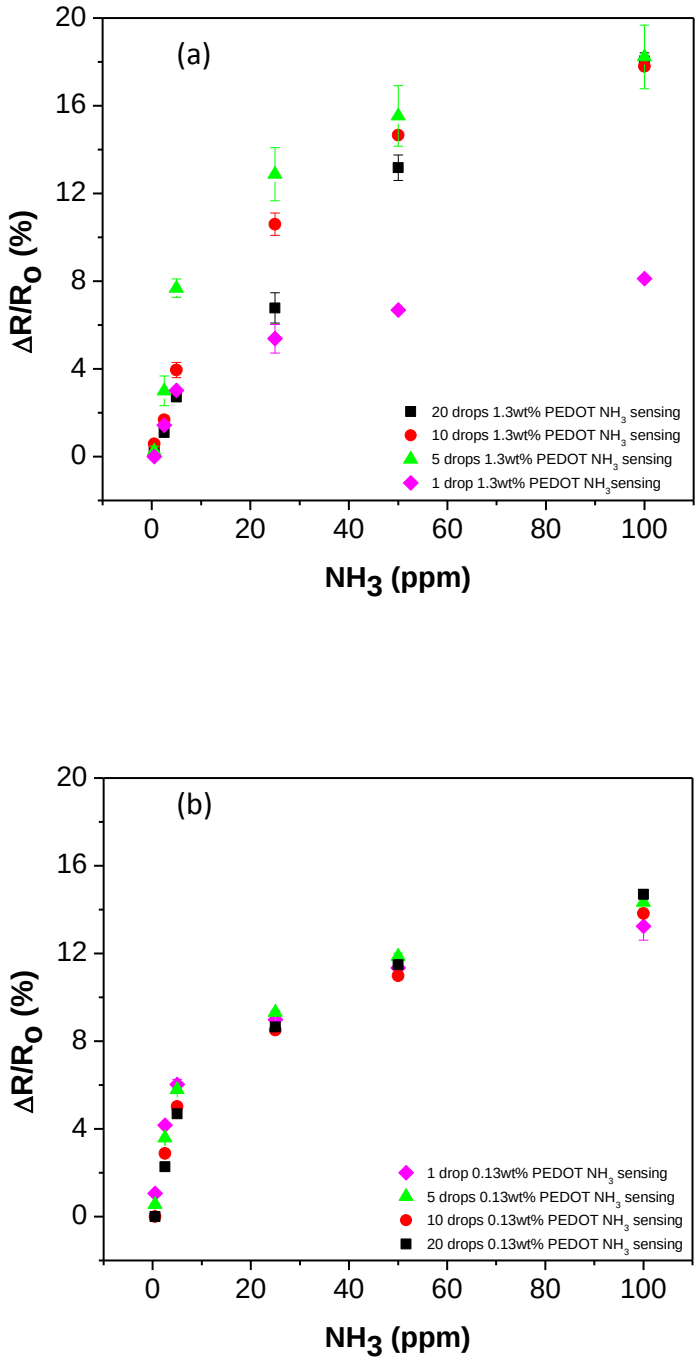

Figure 4.10 Calibration curves of ink-jet printing different drops of (a) 1.3wt.% and (b) 0.13wt.% PEODT-PSS exposed to NH_3 sensing

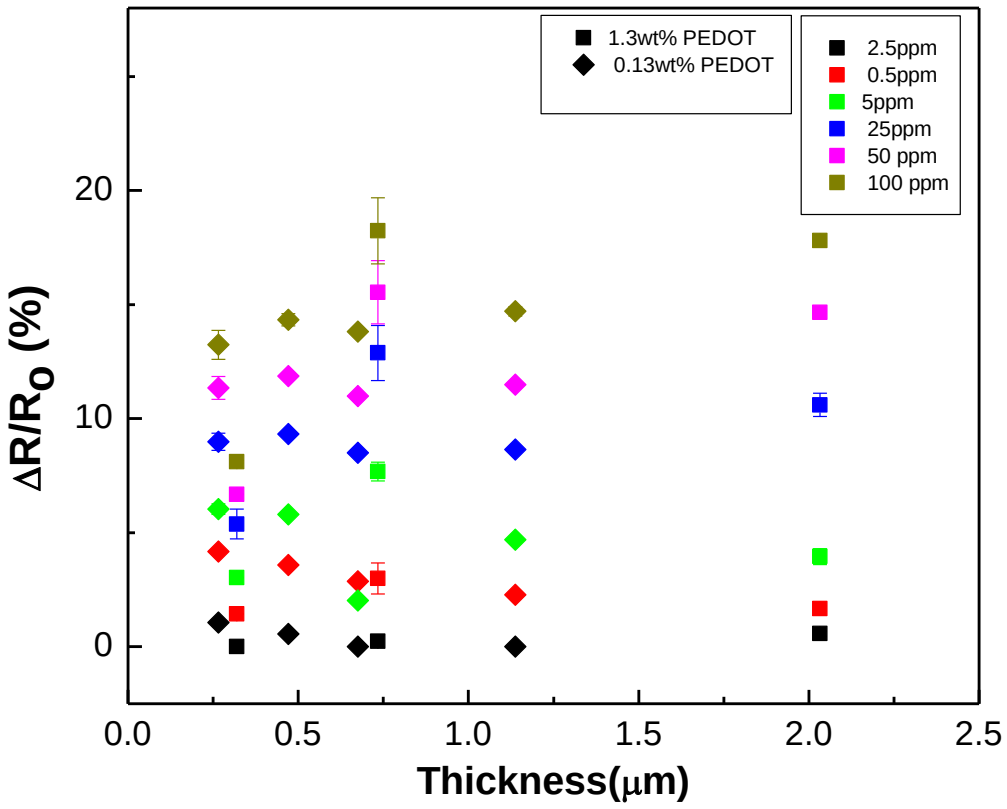

Figure 4.11 Calibration curve of different thickness of PEODT-PSS to NH_3 sensing

References:

1. Singh, M., et al., Inkjet Printing—Process and Its Applications. Advanced Materials, 2010. **22**(6): p. 673-685.
2. Srichan, C., et al. Inkjet printing PEDOT:PSS using desktop inkjet printer. in Electrical Engineering/Electronics, Computer, Telecommunications and Information Technology, 2009. ECTI-CON 2009. 6th International Conference on. 2009.
3. Sappat, A., et al. Humidity sensor based on piezoresistive microcantilever with inkjet printed PEDOT/PSS sensing layers. in Electrical Engineering/Electronics, Computer, Telecommunications and Information Technology (ECTI-CON), 2011 8th International Conference on. 2011.
4. Sriprachuabwong, C., et al. Enhancing electrochemical sensitivity of screen printed carbon electrode by inkjet printed graphene-PEDOT/PSS Layers. in Electrical Engineering/Electronics, Computer, Telecommunications and Information Technology (ECTI-CON), 2011 8th International Conference on. 2011.
5. Hon, K.K.B., L. Li, and I.M. Hutchings, Direct writing technology—Advances and developments. CIRP Annals - Manufacturing Technology, 2008. **57**(2): p. 601-620.
6. Calvert, P., Inkjet Printing for Materials and Devices. Chemistry of Materials, 2001. **13**(10): p. 3299-3305.